1993

Magnetic properties of metallic glasses

Adil Khizar Shaikh
University of Wollongong

MAGNETIC PROPERTIES OF METALLIC GLASSES

A thesis submitted in fulfilment of the requirements for the award of the degree

MASTER OF ENGINEERING (HONOURS)

from

THE UNIVERSITY OF WOLLONGONG

by

ADIL KHIZAR SHAIKH M.Sc.

DEPARTMENT OF MATERIALS ENGINEERING

1993

CANDIDATE'S CERTIFICATE

This is to certify that the work presented in this thesis was carried out by the candidate in the Department of Materials Engineering, the University of Wollongong and has not been submitted to any other university or institution for a higher degree.

.....

ACKNOWLEDGEMENTS

The author would like to thank the entire staff of the Department of Materials Engineering of the University of Wollongong for their kind support and assistance throughout the duration of the research programme. In particular to Dr.J. Khachan and Dr.D. Wexler for their assistance in understanding the instruments, meaningful discussions, helpful suggestions.and assistance on electron metallography.

The author would like to thank his parents, brother and sister for the support to complete this work. The author would also like to thank his friends for their co-operation.

Lastly, the author is indebted to Dr.G.W. Delamore whose guidance and support were paramount in the success of the current research programme.

SYNOPSIS

The response of a series of iron and cobalt-based metallic glasses to heat treatment has been examined in terms of the subsequent changes in magnetic properties. Annealing at temperatures below the crystallisation temperature improves the soft magnetic properties for low frequency applications by relief of stresses generated during rapid solidification. Annealing at higher temperatures improves the magnetic properties for higher frequency applications by introducing a small amount of crystals into the structure which refine the domain size and pin the domain walls, reducing excess eddy current loss.

In the $Co_{75}Si_{10}B_{15}$ glassy alloy, annealing at higher temperatures also produces a shift in the hysteresis loop about the origin. The shift in this alloy is shown to be due principally to crystallisation within the bulk rather than at the surface as previously suggested for some other metallic glasses. The shift in Co-based alloys is due to its high magnetocrystalline anisotropy compared to iron.

Optimum annealing temperatures for magnetic applications at different frequencies have been determined for $Fe_{60}Ni_{20}Si_{10}B_{10}$ and $Fe_{72}Si_{10}B_{18}$. Annealing of $Fe_{72}Si_{10}B_{18}$ close to the Curie temperature ribbon also results in a severely skewed hysteresis loop which is shown to be due to a change in surface condition well before crystallisation can be detected by optical metallography. Removal of the surface layer after annealing produces a dramatic improvement in magnetic properties in this alloy.

TABLE OF CONTENTS

Chapter 1

1.0 INTRODUCTION

In 1960, Pol Duwez and his co-workers [1] reported that certain molten alloys, if rapidly cooled, freeze into amorphous, or glassy, solids.

Depending on composition, the glassy material produced may possess attractive properties such as a high corrosion resistance, high resistivity, and good soft magnetic properties. The soft magnetic properties have attracted major research efforts for many years. The random atomic arrangement of atoms, which lacks regular crystalline anisotropy and grain boundaries, makes the alloys easy to magnetise along any direction. Another unique feature of these materials is the one-step production technique which makes their manufacturing costs far less than those of the conventional steels used in transformer cores. Table 1.1 shows a comparison of some of the magnetic properties of the metallic glasses with the comparable crystalline materials [2]. Some applications of soft magnetic metallic glasses are given in Table 1.2 [3].

The major application of these materials is in distribution transformers. However, there are several disadvantages of these materials, such as their inherent thinness which gives a lower space factor, (ratio of the space filled to the amount of space available), which translates into a larger core. They are also four to five times harder than conventional iron silicon alloys used in transformers, and cutting tools wear out approximately one thousand times faster in cutting amorphous materials than in cutting grain-oriented iron silicon alloys. The amorphous alloys also usually require stress-relief annealing to optimise their magnetic properties which sometimes makes them brittle. In spite of these disadvantages, their 60-70% lower core loss compared with conventional crystalline iron silicon cores have made them attractive for commercial applications.

The work reported in this thesis was undertaken to investigate the effects of heat treatment on the magnetic properties of some iron and cobalt-based metallic glasses, both low temperature annealing for stress relief and also for higher temperature annealing with the aim of improving soft magnetic properties at higher frequencies by introducing a small percentage of crystals into the structure.

Co-based amorphous alloys have a near-zero magnetostriction which makes them attractive for switch mode power supplies and for many types of magnetic sensors. On annealing some of these alloys, an asymmetrically displaced hysteresis loop is obtained. In this work the reason for this asymmetrically displaced hysteresis loop was also investigated.

Curie temperature (T_C), saturation induction (B_S), saturation magnetostriction (λ_S), core loss (L), impedance permeability (μ_S) and dc coercivity (H_C). L, μ_S and H_C are quoted for optimally annealed material; L and μ_S are specified for a typical frequency and maximum level of induction.

Alloy	T_C (°C)	B_S (T)	λ_S (10^{-6})	L (W/kg)	μ_S	H_C (A/m)
(a) Fe-based glasses						
$Fe_{78}B_{13}Si_9$*	415	1.56	27	0.2 (60 Hz/1.4 T)	-	2.5
$Fe_{81}B_{13.5}Si_{3.5}C_2$	370	1.61	30	0.3 (60 Hz/1.4 T)	-	3.2
$Fe_{75}Ni_4Mo_3B_{16}Si_2$	300	1.23	19	7 (50 kHz/0.1 T)	14,000	2.5
(b) FeNi-based glasses						
$Fe_{40}Ni_{38}Mo_4B_{18}$	353	0.88	9	-	(μ_{max} ~500,000)	~1
(c) Co-based glasses						
$Co_{76}Fe_2Mn_4B_{12}Si_6$	405	1.2	0.2	-	18000 (1 kHz/1.01T)	2.5
(d)Conventional crystalline materials						
Oriented Fe-3.5†Si	730	1.97	9	0.9 (60 Hz/1.4 T)	-	10-20
Non-oriented Fe-3.5Si	730	1.97		2.6 (60 Hz/1.4 T)	-	40
Fe-50Ni	480	1.6	25	0.7 (60 Hz/1.4 T)	-	8
Supermalloy (Fe-79Ni-4Mo)	400	0.78	~1	7 (50 kHz/0.1 T)	-	2
Ni-Zn ferrite	210	0.5		15 (50 kHz/0.1 T)	4500	16

* subscripts in atomic %
† composition in weight %

Table 1.1 Principal metallic glass systems and comparable crystalline materials with representative magnetic properties [2].

No.	FIELD OF APPLICATION	SPECIFIC APPLICATION
1	Power Electric Applications	(a) 50/60 Hz Distribution Transformers (b) Electric Motors (c) High-Gradient Magnetic Separators (d) Step-up Transformers and Saturable Reactors for High Repetition Rate Pulse Compressors (e) 400 Hz Airborne Transformers
2	Switching Mode Power Supplies	(a) Saturable Reactors (b) Non-saturable Inverter Transformers
3	Electric Circuits	(a) Pulse Transformers (b) RFI Current compensated Chokes (C) Ground Fault Interrupters
4	Communication Components	(a) Record/Playback Heads for Audio Systems (b) Video Tape Heads (c) Stereophonograph Cartridges
5	Magnetic Shielding	(a) Flexible Shielding Wrap (b) Flexible Cable Shielding (c) Cassette Shielding Spring
6	Sensors & Transducers	(a) Magneto-Elastic Force, Displacement and Torque Transducers (b) Magnetic Field Sensors (c) Temperature Transducers and Sensors (d) Personal Identification Badges (e) Anti-Pilferage Devices (f) Pulse Generator Devices

Table 1.2 Applications of soft magnetic metallic glasses [3].

Chapter 2

2.0 LITERATURE REVIEW

2.1 Metallic Glasses

In some metallic alloy systems, the liquid can be cooled to the solid state without crystallisation occurring. The frozen, thermodynamically unstable structure thus obtained is called 'metallic glass'. The process can be understood by considering a time-temperature-crystallisation diagram, as shown in Fig.2.1.1 [4].

In Fig.2.1.1, the C-shaped curves indicate the starting time and finishing time of crystallisation when liquid is cooled below its melting point to a particular temperature level. The 'nose' of the curve indicates the minimum time required to start crystallisation. If the liquid is supercooled to a temperature above the nose of the curve then the time taken to start crystallisation is long. If the alloy is in the liquid state at a temperature below the nose then the time taken to start crystallisation is also long because diffusion in the liquid becomes progressively more difficult and it takes longer to arrange the atoms to form stable nuclei. In order to avoid crystallisation and obtain the solid state, the liquid must be cooled to the glass transition temperature, well below the nose of the C-curve, in a time which is less than the time at which the nose is positioned. Since silicates and many organic polymers have complicated structures, the position of the nose of the C-curve for crystallisation lies at hours or days on the time scale, hence it is easy to cool them to the glassy state at low cooling rates. For metals, the atomic structure is comparatively very simple and the nose lies at few milliseconds on the time scale: as a result when molten metal is cooled slowly, it crystallises. In order to avoid crystallisation, the molten metal must be cooled very quickly, typically at rates of 10^5°C to 10^6°C per second or greater.

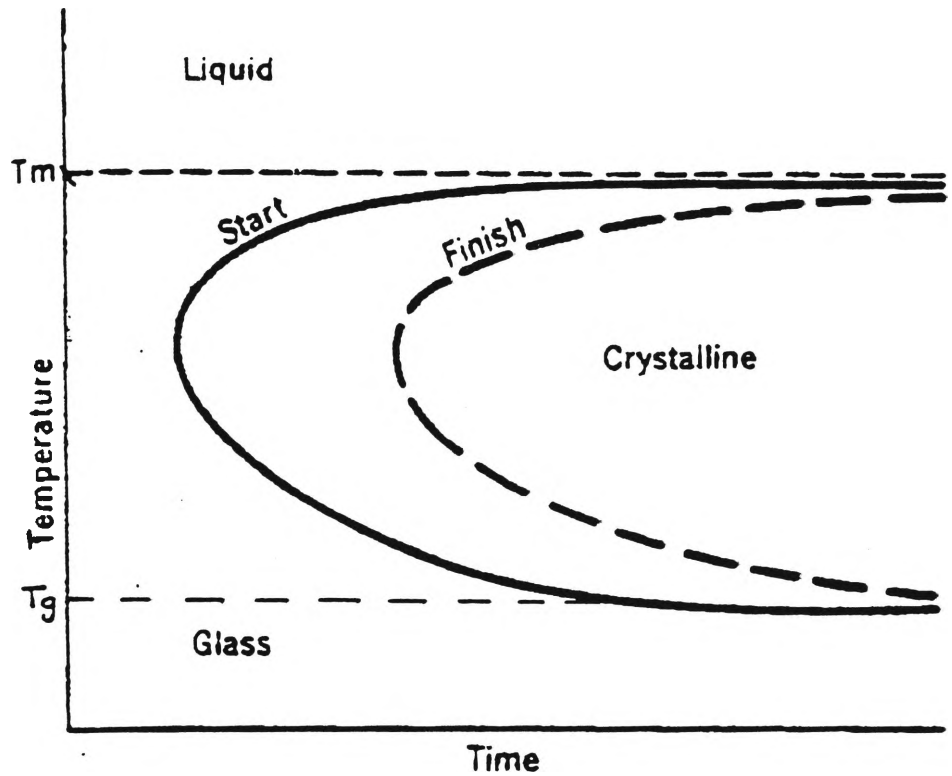

Fig.2.1.1 A time-temperature-crystallisation diagram. To obtain glass,the cooling curve from liquid state must avoid intersecting the crystallisation "start" line [4] .

Tm = melting point

Tg = glass transition temperature

Metallic glasses are produced by different chill-block melt-spinning techniques such as free-jet melt-spinning (FJMS), twin-roller quenching (TRQ) and planar flow casting (PFC). In the past decade, the PFC technique developed by Narasimhan [5] at Allied Corporation has become popular for the production of metallic glasses because this technique allows the production of continuous and wide ribbon. A schematic diagram of the technique is shown in Fig.2.1.2. A rectangular slotted nozzle, fixed close to the wheel, enables the formation of a stable molten metal puddle between the lips of the nozzle and the substrate (wheel) which moves at a high speed. The stable puddle enables continuous casting of amorphous ribbon. The high cooling rates required for glass formation generally limits ribbon thickness to less than 100μm. In principle, if the nozzle-substrate distance can be maintained constant across the width of the wheel to form a stable molten metal puddle, there is no limit to ribbon width. Ribbons up to 213 mm wide have been produced by this technique [6].

X-ray and electron diffraction are used to confirm the amorphous structure of the materials. For Pd-Si alloys the diffraction pattern is shown in Fig.2.1.3 [7]. For other amorphous alloys the diffraction pattern is similar to that of Fig.2.1.3 which indicates that the atomic arrangement of metallic glasses is essentially liquid-like.

2.2 Composition of amorphous alloys for magnetic applications

To produce metallic glasses from the melt generally requires some glass-forming alloy components such as the metalloids B, Si, C and P or the metals Ti, Zr. Some metal-metalloid based amorphous alloys have good soft magnetic properties. They have been categorised into three groups [8]:

(1) Fe-rich alloys with high magnetic saturation magnetisation. They are relatively inexpensive and have saturation magnetisation values of 1.7-1.75 Tesla. Their magnetostriction constant, $\lambda_S \approx 30 \times 10^{-6}$.

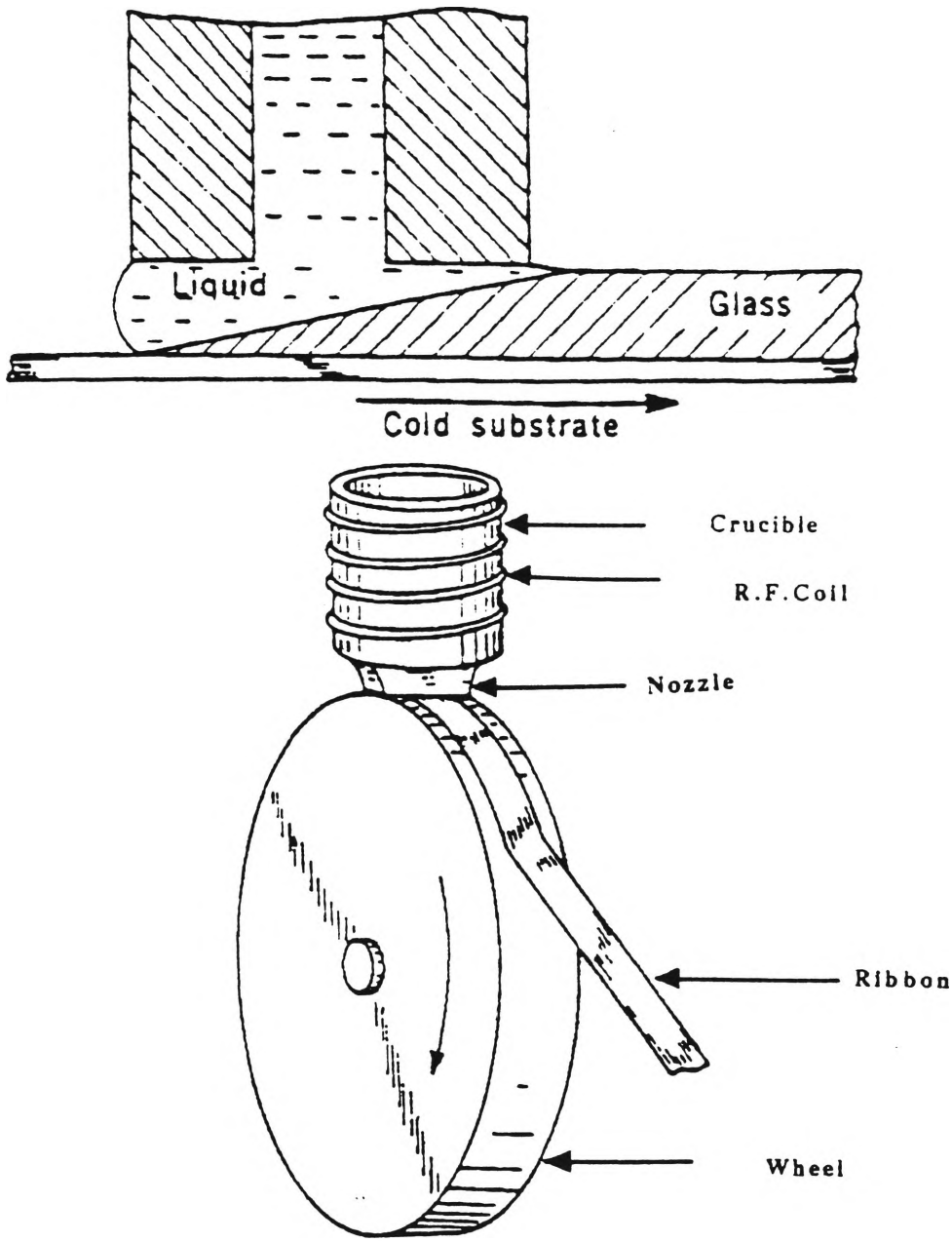

Fig.2.1.2 Schematic diagram of the planar flow casting technique [5].

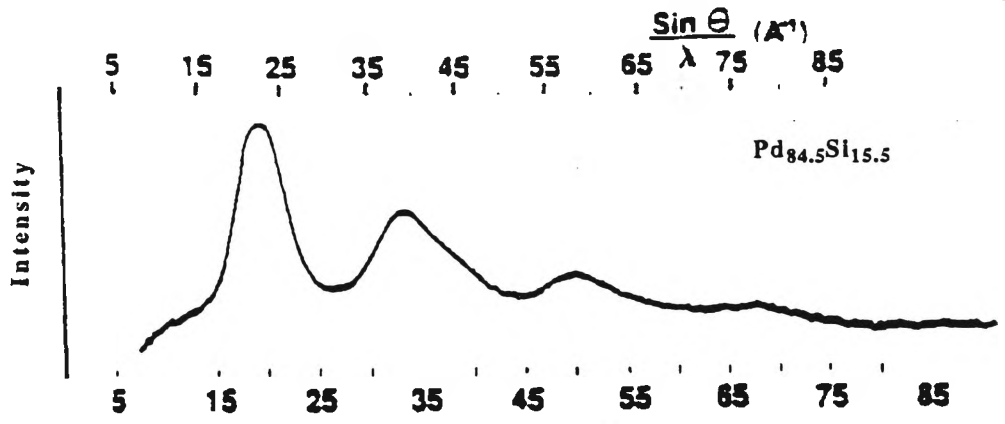

Fig.2.1.3 X-ray diffraction pattern for an amorphous Pd-Si alloy [7] .

(2) Fe-Ni-rich alloys with an intermediate saturation magnetisation. These alloys have saturation magnetisation values of 0.7-1.0 Tesla. Due to the presence of Ni, the glass forming ability and the ductility improves and the magnetostriction constant reduces to approximately 10×10^{-6}.

(3) Co-rich alloys with near zero-magnetostriction and high permeability. They have excellent soft magnetic properties but their saturation magnetisation is not as high as that of Fe-rich alloys.

In 1972, Chen and Polk [9] suggested a formula for thermally stable amorphous alloys.

$$M_aY_bZ_c$$

where M = any of Fe, Ni, Co, V, Cr or their combination

Y = any of P, B, C

Z = any of Al, Si, Sn, Sb, Ge, In and Be

a = 60-90 at%

b = 10-30 at%

c = 0.1-15 at%

The sum of a, b, c is 100%.

Adam and Fish [2] have reported that the most widely used general formula for the transitional metal (Fe, Co, and Ni) magnetic metallic glasses is:

$$M_a(Y, Z)_b$$

where Y is metalloid (e.g. B, P, C) and Z is a non-transitional element such as Si, Ge or Al. a is 75-85 at% and b is 15-25 at%.

2.3 Magnetic Circuits

The shape of the sample (e.g.toroidal, strip, rod, etc.) must be considered when carrying out magnetic measurements on it. For example, parameters such as path length and demagnetising fields must be taken into account so that magnetic properties can be measured with some accuracy.

A closed magnetic circuit with constant cross-section and homogenous flux distribution is the most common configuration for the measurement of magnetic properties of a material. Toroidal cores, formed by stamping or helical winding of a strip, are considered to form a closed magnetic circuit and have a homogeneous flux distribution. However, helically wound toroidal cores have a small gap between the successive laminations. Practically, this air gap can usually be neglected [10] since it is small compared to the total length of the strip.

To study the magnetic properties of ferromagnetic materials, one has to make a toroidal transformer. This is shown in Fig.2.3.1. The primary coil is wound uniformly around the specimen. The secondary coil consists of a relatively large number of turns wound on a small section and in close proximity to the specimen.

An alternating current is applied to the primary coil from a sine wave generator which creates a magnetic field (H) in the sample. The field strength (H) for the closed circuit can then be calculated from the following equation:

$$H = \frac{N_1 I}{l}$$

where H is the field strength in amps/metre

I is the current in amps

N_1 is the total number of turns in the primary coil

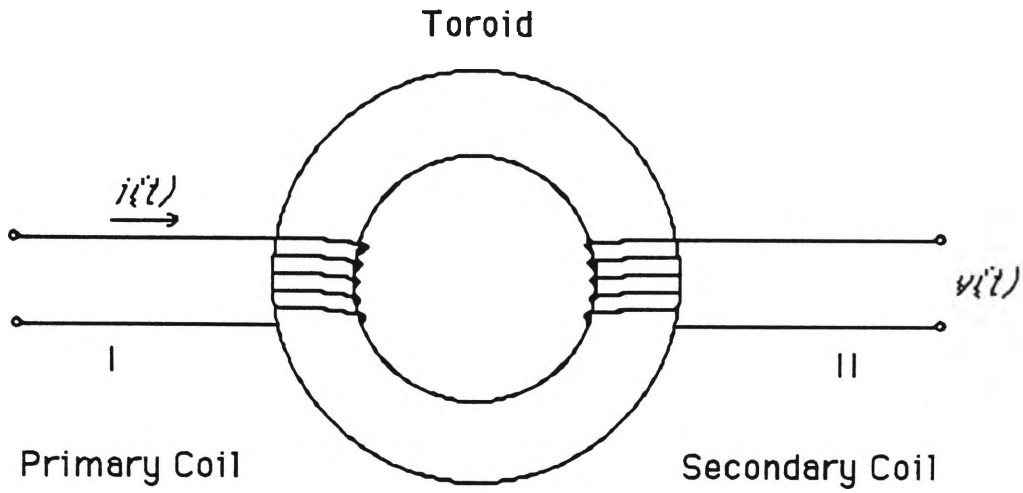

Fig.2.3.1 A toroidal sample for magnetic measurements.

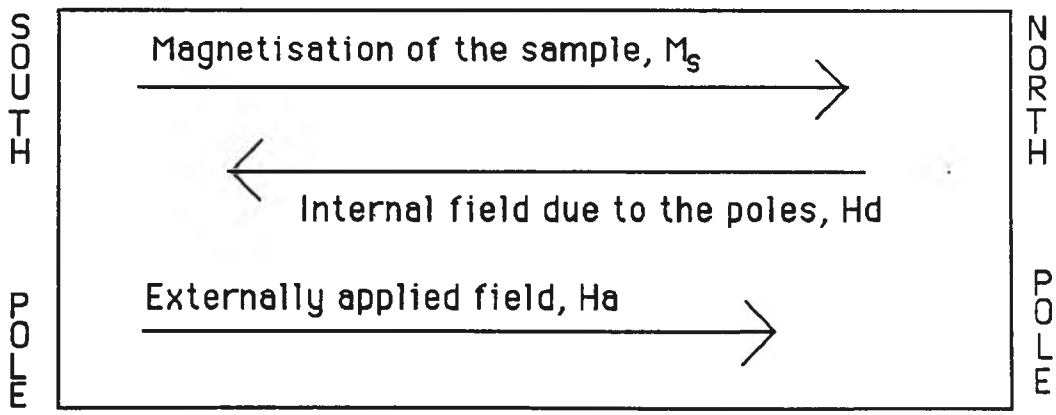

Fig.2.3.2 Magnetisation in strip or rod shaped specimen.

l is the mean magnetic length (i.e. the length of the core) in metres.

The alternating magnetic field (H) induces an alternating magnetic field (B) known as the magnetic induction, in the sample. This in turn produces a voltage in the secondary coil. The induced voltage (V) is directly proportional to the rate of change of the induction:

$$\frac{dB}{dt} = \frac{V}{N_2 A}$$

where V is the voltage induced in the secondary coil

N_2 is the number of turns in the secondary coil

A is the cross-sectional area of the specimen

So, the magnetic induction in the specimen is given as:

$$B = \int \frac{dB}{dt} dt = \int \frac{V}{N_2 A} dt$$

The magnetic induction (B) has the units of Tesla.

If magnetic measurements are carried out on strip or rod-shaped samples, then north and south poles arise at the ends of the specimen, as shown in Fig.2.3.2. These poles produce a demagnetising field (H_d) inside the specimen which weakens the externally applied field (H_a), by a fraction, N_{zz}, known as the demagnetising factor.

The relationship between different fields shown in Fig.2.3.2 can be represented by the following equation:

$$B = \mu_0 (H_a - N_{zz} M_s + M_s)$$

where μ_o is the permeability of free space

M_S is magnetisation of sample. It is the average magnetic moment per unit volume.

The demagnetising factor(N_{zz}) is calculated from the geometry of the sample, because N_{zz} is different for different shapes of samples as well as non-uniform within the specimen [11]. From the above equation it is clear that if N_{zz} is large, then a larger H_a is required to reach higher induction (B). In order to reduce H_a it is necessary to reduce N_{zz}, which can be accomplished by selecting a very thin and a narrow sample compared to its length. This can be understood from Fig.2.3.3 [11].

If the calculated values of H and B are plotted on X and Y axes respectively, the curve obtained is called a hysteresis loop. The energy dissipated in the sample per unit volume per cycle can be obtained by calculating the area of the hysteresis loop. This energy is given by the following equation:

$$E = \int H \, dB$$

The power dissipated per kilogram of the sample (core loss) is given by multiplying E by frequency and dividing by the density.

$$L = \frac{f}{\rho} \int H \, dB$$

where L is the core loss in watts/kg

f is the frequency in Hertz

ρ is the density of the sample in kg/m^3.

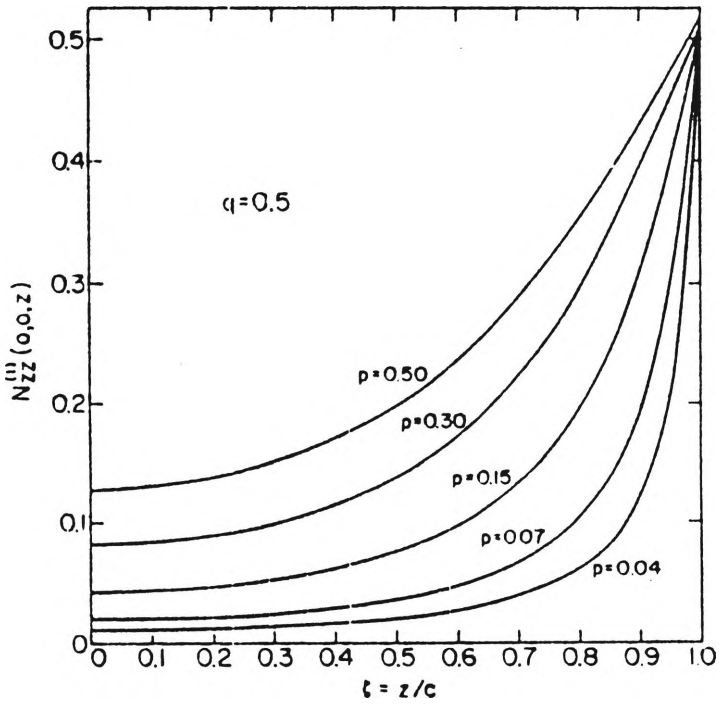

Fig.2.3.3 The diagram indicates the spatial variation of the first-order demagnetisation factor $N_{zz}^{(1)}$ along a co-ordinate axis of the rectangle specimen (x = y = 0) in terms of reduced variable $\xi = z/c$ (z is the distance from the centre of the rectangular specimen) for various thickness (q = a/c = 0.5, p = b/c). The $N_{zz}^{(1)}(-z) = N_{zz}^{(1)}(z)$ where 2a, 2b and 2c are the width, length and the thickness of the specimen. As the thickness of the specimen decreases, the $N_{zz}^{(1)}$ factor decreases. Note that the demagnetisation factor across the length is uniform for a very thin specimen and it is non-uniform only at the ends [11].

Magnetic properties of the specimen may be measured by AC , DC or pulse magnetic measurement methods [10].

2.3.1 D.C. Magnetic Measurement Circuit

An infinitely slow change in the magnetic field induced in the specimen is considered to be a DC (static) magnetic field. In this case the magnetic properties of a material are free from all dynamic influences, such as eddy currents. As a result, the static hysteresis loop is narrower than the dynamic loop.

The ballistic method is usually used to measure the DC field properties of a material. In this method, the shape of the specimen is one of several configurations such as ring, toroidal, link, double-lapped Epstein cores, or other standard shapes without air gaps. A schematic circuit diagram of this method is given in Fig.2.3.4 in which a calibrated ballistic galvanometer (G) is used. N_1 and N_2 are uniformly distributed primary and secondary coils, K is the battery reversing key and R is a resistance to control the current in the primary coil. The deflection of the galvanometer is noted when the polarity of the current is reversed. This test method is suitable for a testing range from very low magnetising force up to 15.9 kA/m or more. The flux density is measured with a high-sensitivity galvanometer which is calibrated by means of a standard mutual inductor before the measurement of the test materials. This method enables initial magnetisation curves and hysteresis loops to be plotted point by point and their related quantities determined [10].

2.3.2 A.C. Magnetic Measurement Circuit

When the applied magnetic field is AC then the magnetic properties of a material are measured by either the transformer method, ferrometer method, wattmeter method,

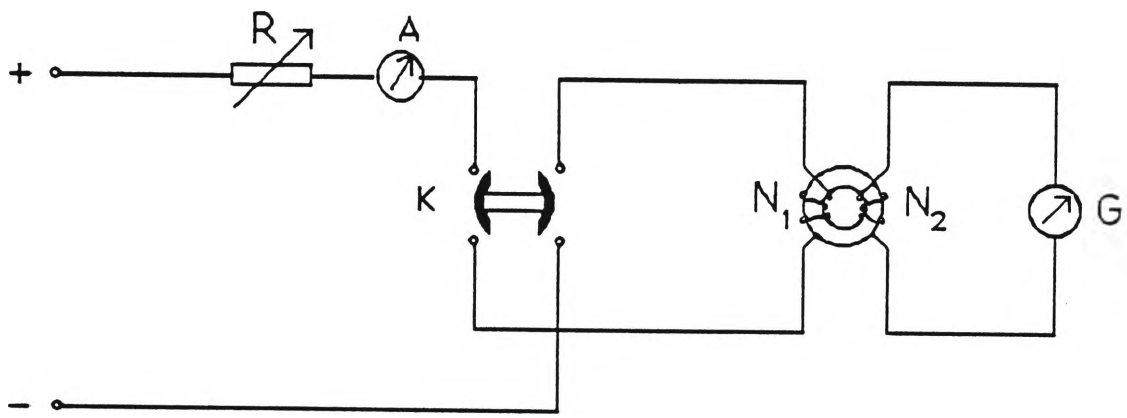

Fig.2.3.4 DC magnetic measurement circuit.

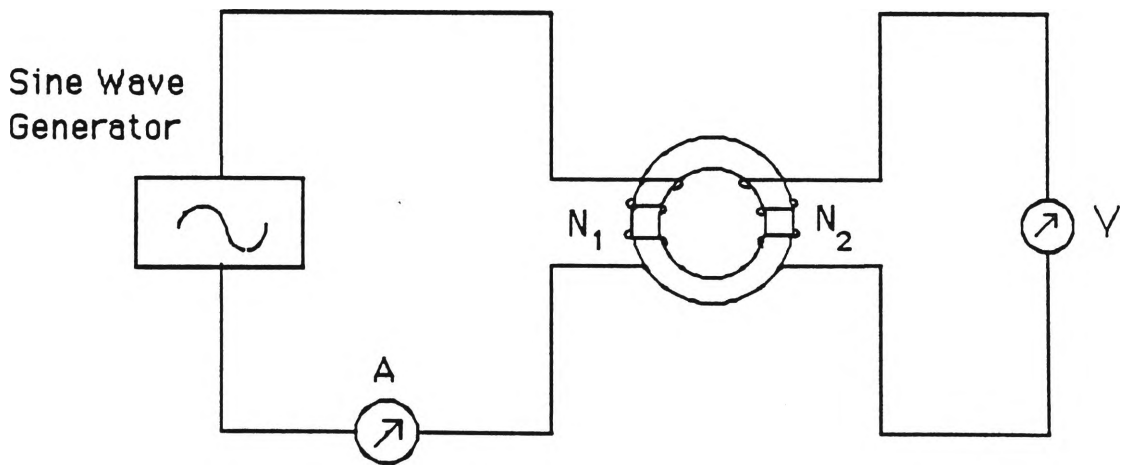

Fig.2.3.5 AC magnetic measurement circuit.

bridge method, oscillographic recording method or multiplier method. The simplest of all these methods is the transformer method.

(a) Transformer method

A schematic diagram of the transformer method is shown in Fig.2.3.5. In this method the magnetisation of the sample takes place from a sine wave generator or from the mains with low output resistance in order to avoid distortion in the sine voltage. The root mean square (rms) value of the magnetising current, I, and the rms or rectified value of secondary voltage, V, respectively are measured. The field strength and flux density are calculated using Laplace and Faraday's Laws. By this method many magnetic parameters at various excitations and frequencies can be measured.

(b) Multiplier method

The flux density (B) wave form becomes non-sinusoidal at higher excitation values of the applied magnetic field (H) and as a result, the sample appears to have a greater core loss due to harmonics in B [12]. The multiplier method is used to calculate core loss and eliminate the contribution from harmonics provided that both H and B are periodic and at least one of them is sinusoidal. Some groups try to keep B sinusoidal [13] by using an electronic feed back circuit. This introduces harmonics into H in such a way that B remains sinusoidal. The drawback in using this method is that the accuracy of the results depends on the phase of the feedback signal, which in turn is dependent on the impedance of the primary coil. As a result the circuit must be adjusted at different frequencies. The alternative method is to keep H sinusoidal and eliminate the harmonics mathematically from B. This is simpler since it does not require any feedback circuitry and is the method used by Khachan and Delamore [14]. This method is explained as follows.

The signal from the secondary coil is directly proportional to the rate of change of flux density, dB/dt. This can be written as a Fourier series:

$$\frac{dB}{dt} = B_1\omega \cos(\omega t + \phi_1) + \sum_{n>1} B_n\omega \sin(n\omega t + \phi_n)$$

where n is an integer

ϕ_n is the phase factor

ω is the angular frequency

t is time

In the above equation, the first and second terms represent the fundamental component at angular frequency (ω) and the harmonics in B, respectively. The core loss contribution from the fundamental frequency is obtained by eliminating the second term. This can be achieved by multiplying H by dB/dt and integrating over one cycle. Consequently, the core loss L, can be written as:

$$L = \frac{f}{\rho}\int_0^{1/2\pi f} H\frac{dB}{dt}\,dt$$

where f is the frequency

ρ is the density of the material.

2.4 Magnetism in Metallic Glasses

All pure metals and their alloys are magnetic but most of them are only weakly magnetic. Magnetism is divided into several categories depending on its cause and strength. Ferromagnetism is the strongest among diamagnetism, paramagnetism,

ferromagnetism, antiferromagnetism and ferrimagnetism. Ferri- and ferromagnetic materials are used as magnetic materials.

Electrons in an atom possess spin and orbital magnetic moments and as a result each atom behaves like a small magnet. At a critical separation of atoms, these 'small magnets' are intercoupled and this produces spontaneous alignment of atomic magnetic moments. In ferromagnetic materials the atomic magnets are parallel-aligned as shown in Fig.2.4.1. This alignment results in a net magnetisation over a small region called a ferromagnetic (Weiss) domain. In adjacent domains, the magnetisation vectors lie in different directions as shown in Fig.2.4.2. These magnetic domains are aligned in such a way that the total magnetisation of the whole body is zero. This condition is known as the **demagnetised state**. Domains are separated by domain walls, also known as Bloch Walls, and these domain walls have energy due to misalignment of atomic magnetic moments. The domain wall structure is shown in Fig.2.4.3. The typical width of these domain walls is 100 nm. More detail is given in Section 2.5.

The schematic hysteresis BH loop of a magnetic material is shown in Fig.2.4.4 [2]. The BH loop shows a non-linear dependence of the induced magnetisation (B) as a function of the applied field (H).

In the absence of an external magnetic field the material is in the demagnetised state, H = B = 0, {O in Fig.2.4.4}. As the magnetic field is applied, the material is magnetised and eventually reaches the **saturation induction** (B_S) {W in Fig.2.4.4}. B_S is the maximum achievable value of induced magnetisation. When the applied field is removed the material returns to the **remanent induction** (B_r). This is an indication of the magnetisation remaining in the material when the magnetic field is removed. To remove the remanent induction, a reverse field is applied $H = -H_C$ {X in Fig.2.4.4} and then to $-B_S$ {Y in Fig.2.4.4}. The next cycle of the applied field retraces the BH loop WXYZ. The area enclosed by WXYZ is the hysteresis loss component of the total core

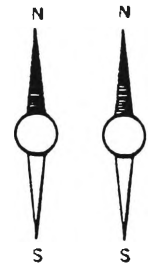

Fig.2.4.1 Ferromagnetism: Two magnetic moments are aligned parallel to each other [10].

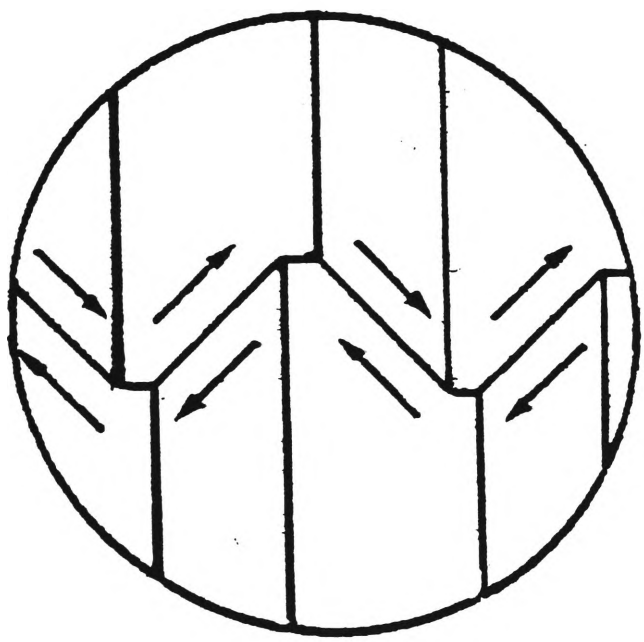

Fig.2.4.2 Ferromagnetic domains [10].

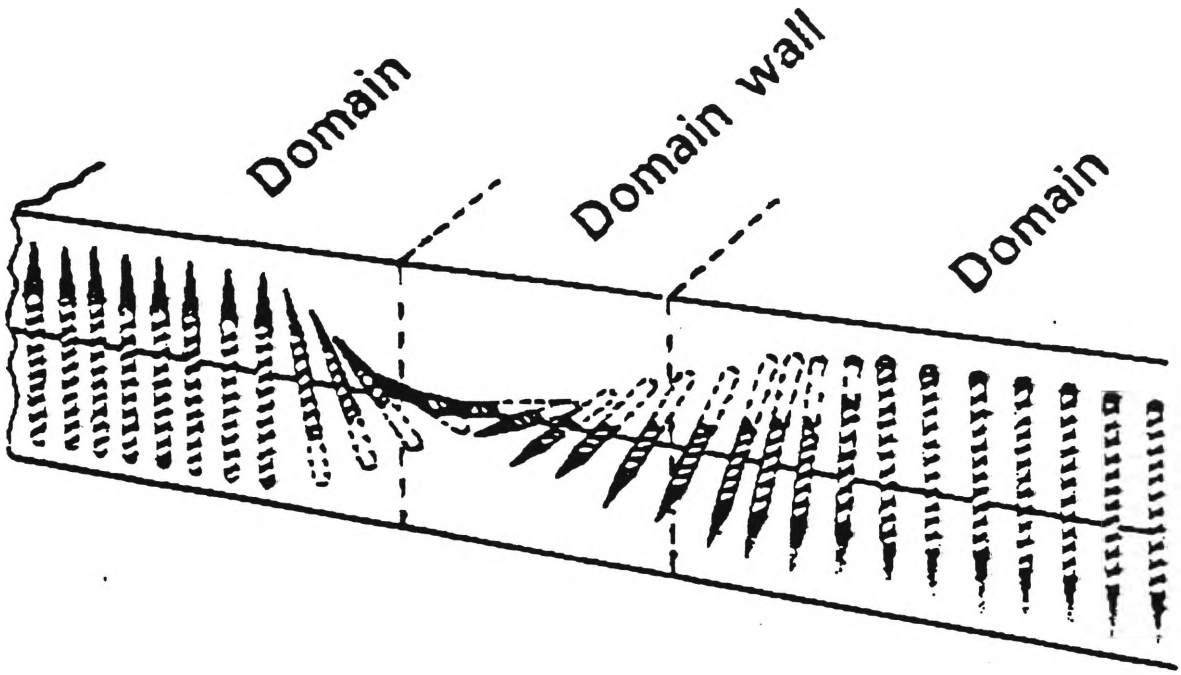

(a) domain wall structure

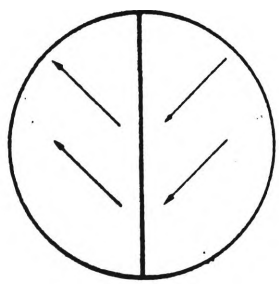

(b) 90° domain wall

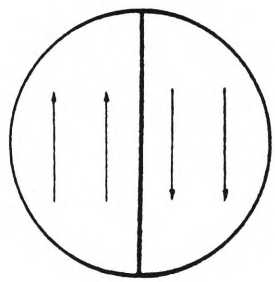

(c) 180° domain wall

Fig.2.4.3 Domain wall [10].

loss per cycle. When a magnetic material is first magnetised from the demagnetised state, it follows the initial magnetisation curve (from O to W in Fig.2.4.4). The ratio of flux density (B) to the applied field (H) when expressed in the same units gives the **permeability** (μ). The permeability at very low flux density or applied field is called the initial permeability (μ_i). At the knee of initial magnetisation curve the permeability reaches a maximum known as the maximum permeability (μ_{max}). The field required to remove the remanent induction (B_r) is called the coercive field strength or **coercivity** (H_c). **Core loss** is the energy lost in the sample which is dissipated as heat.

The maximum induced flux density depends on the material composition while the other properties such as core loss, coercivity, remanence etc. depend on the ease with which magnetic domains change size through wall motion and/or reorient to accommodate the external field.

Some alloys change their dimensions when subjected to a magnetic field. This is known as **magnetostriction**. Iron-based alloys elongate in the direction of magnetisation and contract in the perpendicular direction while nickel-based alloys behave in the opposite sense to that of iron-based alloys [10]. The **saturation magnetostriction** (λ_s) is defined as the fractional change in length when the sample is brought from a demagnetised state to the fully saturated state and ranges from ~30 X 10^{-6} for Fe-based glasses to near-zero for glasses containing Co [8]. Co-based alloys can be made zero magnetostrictive by adding a small amount of Fe, Ni or Mn. These glasses have high permeability and minimal stress sensitivity.

2.5 Domain Structure and its behaviour in an applied magnetic field

The above section dealt with the behaviour of magnetic material in the presence of an external magnetic field at the macroscopic level. At a microscopic level, the shape

of the hysteresis loop is determined by the movement of domains when subjected to an external magnetic field.

The domain pattern observed in amorphous alloys is very irregular and depends on the distribution of magnetic anisotropy. Guobin et al. [15] have found that the domain structure also depends on the method of preparation irrespective of the composition. Domains can be of two types [16,17]:

1) Wide domains with the magnetisation vector lying within the ribbon plane. The domain pattern is either like stripes, oriented in parallel or perpendicular to the ribbon length, or has a star-like structure as shown in Fig.2.5.1. The domain width is approximately 100-300 μm.
2) Narrow domains with magnetisation vectors lying perpendicular to the ribbon plane. As a result, magnetic surface charges occur which can be suppressed by the development of closure domain structures as shown in Fig.2.5.2. Their width is approx. 1-30 μm.

Domain structure changes under the influence of an external magnetic field, so that the average magnetic moment contained within that structure increases its alignment with the external magnetic field. The change in the domain structures of Fig.2.5.1 and Fig.2.5.2 under an external magnetic field is shown in Fig.2.5.3 and Fig.2.5.4.

1) In the case of longitudinal anisotropy, a shift of domain walls occurs as shown in Fig.2.5.3a.
2) In the case of transverse anisotropy, the domain walls remain stable and magnetic vectors inside domains rotate towards the external field direction as shown in Fig.2.5.3b.

(a) stripes (b) star-like.

Fig.2.5.1 Wide domains with the magnetisation vector lying within the ribbon plane [17].

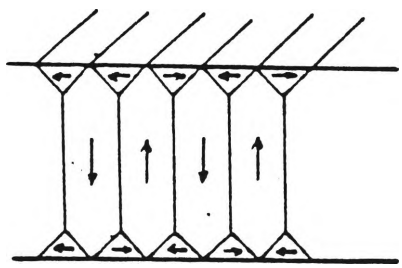

Fig.2.5.2 Model of narrow domains with magnetisation vectors perpendicular to ribbon plane. The closure domains are also shown [17].

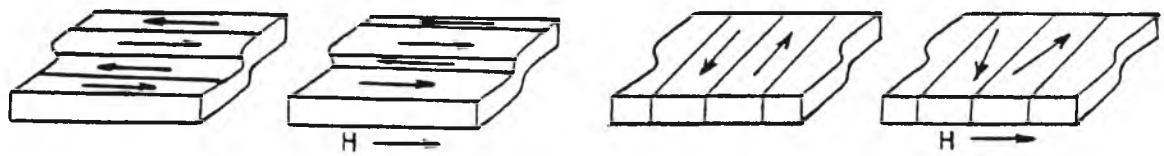

(a) In case of longitudinal anisotropy (b) In case of transverse anisotropy

Fig.2.5.3 The change in the domain structure under magnetic fields [17].

(a) At low magnetic field (b) At high magnetic field

Fig.2.5.4 The change in narrow domain structure under low and high magnetic fields. [17].

3) In the case of magnetic vectors being perpendicular to the ribbon plane, domain wall displacement dominates at lower magnetic fields (Fig.2.5.4a) while domain wall rotation dominates at higher fields (Fig.2.5.4b).

Fig.2.5.5 shows the initial magnetisation curve which is divided into four parts according to the behaviour of domains in the presence of an external magnetic field [17].

Region I results from reversible shifts of wide domain walls

Region II results from irreversible shifts of wide domain walls

Region III results from magnetisation processes inside narrow domains

Region IV results from reversible rotation in a saturated sample

In the low field region, Region I, (i.e. when $H < 0.1\ H_c$), Rayleigh's law is satisfied:

$$M = \chi_0 H + \alpha H^2$$

where χ_0 is the initial susceptibility, α is the Rayleigh constant and M is the magnetisation of the sample at an applied magnetic field, H. The first term in the above equation describes the reversible, while the second term describes the irreversible part of the magnetisation at low fields.

At higher fields, Region II, ($0.1H_c < H < H_c$), magnetisation occurs by large irreversible Barkhausen jumps which cause irregularities in the loop and magnetic noise. Magnetic noise is at a minimum in near-zero magnetostrictive alloys. The Barkhausen effect is due to barriers to the movement of domain walls. When domain walls acquire enough energy from the field, they overcome the barrier and continue the movement until new barriers are encountered. This makes the movement of the domain boundary non-uniform, jerky and irreversible. This process consists of many steps as

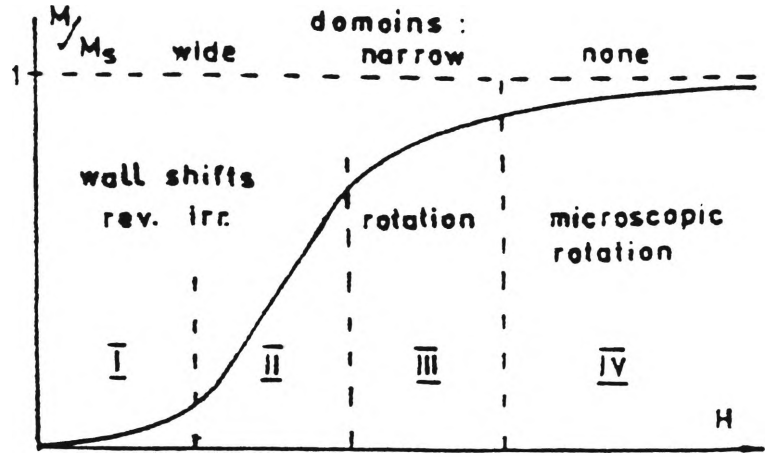

Fig.2.5.5 Initial magnetisation curve [17].

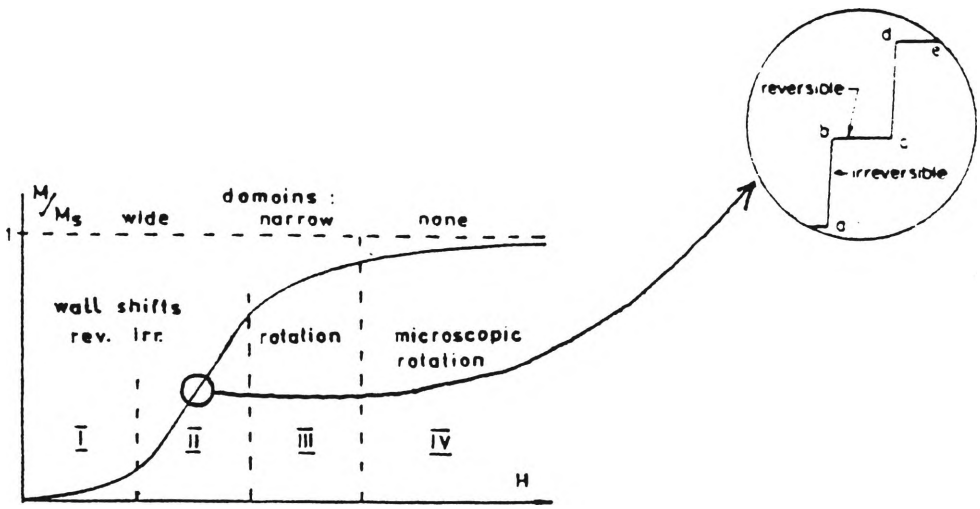

Fig.2.5.6 Barkhausen jump [49].

shown in Fig.2.5.6. Each step consists of an irreversible jump in induction from point a to b, c to d etc, and a reversible but much slower rise in induction from point b to c, d to e, etc. According to Kronmuller [16] the main hysteresis losses occur in this region and are given by

$$\Delta L_H = 4M_S H_C$$

where M_S is the magnetic moment per unit volume.

In Region III, (i.e. $H_C < H < 2K_O/M_S$, where K_O is an anisotropy constant due to induced anisotropy or magnetoelastic coupling energy) the domains with magnetisation vectors perpendicular to the ribbon plane and the closure domains are magnetised parallel to the applied magnetic field by domain wall displacement and microscopic rotations [16]

In the very high field region, Region IV, (i.e. when $H > 2K_O/M_S$), magnetisation occurs by microscopic, reversible rotation in regions of inhomogeneous spin states around defect structures which arise due to the magnetoelastic interactions between defect structure and M_S [16].

During magnetisation of a material, domain wall motion may vary from area to area due to pinning caused by surface roughness [18,19], ragged edges [19] or stresses introduced during manufacture [18]. As a result, in some regions of the ribbon, domain walls are highly mobile while in other regions they are stationary and pinned [18]. This non-uniformity gives rise to higher coercive force and hence the core loss is increased. Core loss is defined as the energy loss per cycle in a material subjected to an AC magnetic field. It is denoted as L_T. Core loss is composed of hysteresis loss (L_H) classical eddy current loss (L_E) and anomalous eddy current loss (L_A) [17].

Hysteresis loss is proportional to the area of the DC hysteresis loop and to the frequency of the applied field [17]. At frequencies below 500 Hz, the major contribution to core loss is hysteresis loss [20]. Hysteresis loss increases with an increase in coercivity due to pinning of domain walls. This pinning of domain walls can be reduced by smoothing the surface [18] or by annealing, which relieves stress induced during manufacturing. Luborsky [19] showed that ribbon manufactured in air has a coercivity 2 to 3 times higher than ribbon manufactured in vacuum because the air-cast ribbon had rougher surfaces and ragged edges.

The second component of the total core loss is the classical eddy current loss (L_E). It is due to the macro eddy currents induced surrounding the volume of the material by the changing external magnetic field. It is proportional to square of the frequency, to the electrical conductivity and to the square of the ribbon thickness.

The third factor in the core loss is anomalous or excess eddy current loss. It is the difference between the total core loss and the sum of the classical eddy current loss and hysteresis loss. The excess eddy current loss is due to the micro eddy current produced by domain wall movement [17]. It has been suggested that the principal cause of excess eddy current loss in amorphous ribbon is wide effective domain wall spacing [21]. Excess eddy current losses are responsible for up to 90% of total loss at higher frequency [50]. The eddy current loss is less in thinner samples as shown in Fig.2.5.7 [23].

Classical separation of core loss as a function of frequency into its components is shown in Fig.2.5.8 [24].

At higher frequencies, domain wall motion is rapid to accommodate the rate of change of magnetisation. Since the magnitude of eddy current losses is directly proportional to domain wall motion, eddy currents increase with increase of domain

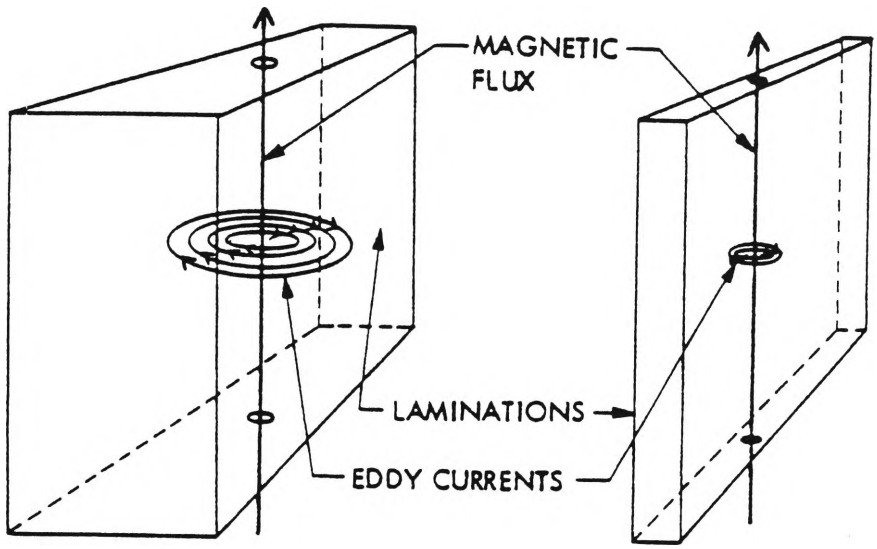

Fig.2.5.7 Eddy currents in both thick and thin samples [23].

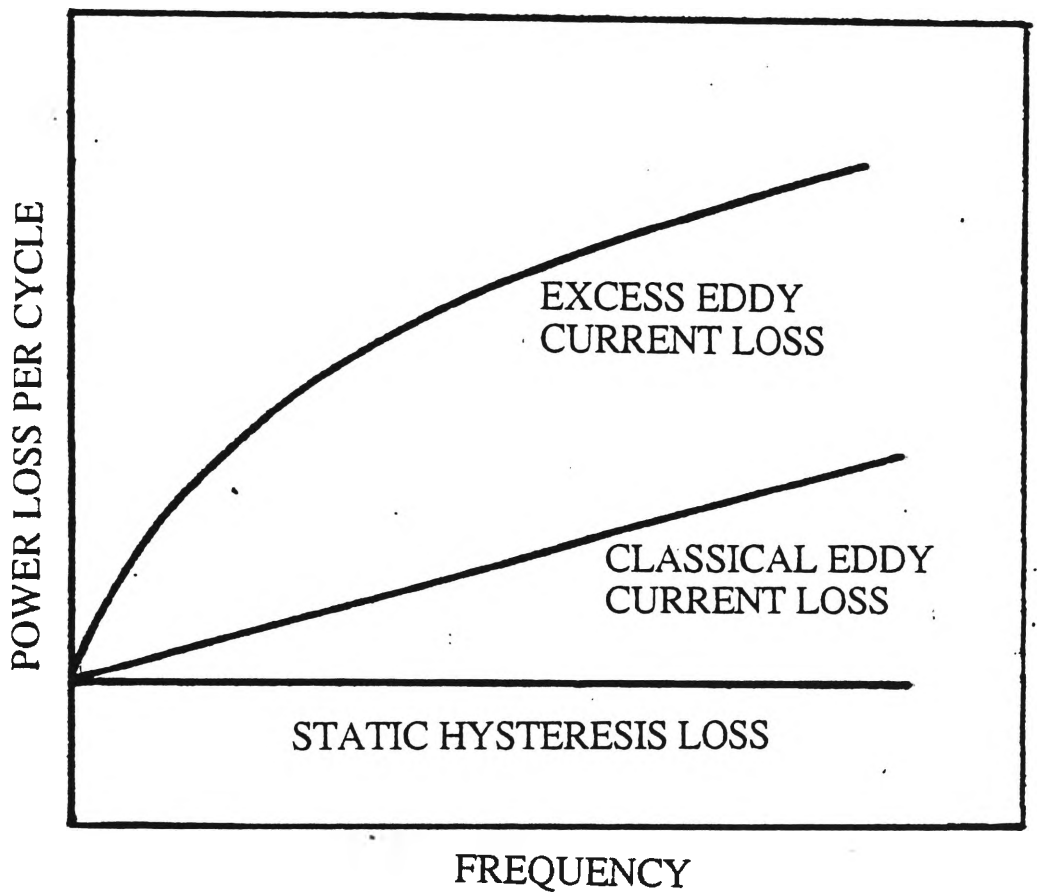

Fig.2.5.8 Classical separation of core loss as a function of frequency [24].

wall velocity and decrease with decrease of domain wall velocity [25,26]. If the domain wall motion is restricted at high operating frequency then the eddy current losses can be reduced significantly. To reduce the eddy current loss it is necessary to refine the domain size (i.e. reducing the domain width) or pin domain walls. The refinement of domain size increases the number of domain walls while pinning of domain walls reduces the domain wall motion. The refinement of domains and wall pinning can be achieved by introducing 1 to 5% crystals in the structure which reduces domain wall spacing from ~1 mm to ~100 μm [25,26,27,43,44]. Fig.2.5.9 [27] shows the decrease in core loss at higher frequencies with the introduction of crystals. In Fe-based alloys, it has been found that α–Fe crystals refine the ferromagnetic domain structure effectively [43,44]. Domain refinement due to crystallisation is shown in Fig.2.5.10 [26].

2.6 Heat Treatment of Metallic Glasses

Since metallic glasses are produced by rapidly cooling the molten metal, the as-quenched state shows a highly disordered structure which undergoes changes upon subsequent annealing above room temperature.

Annealing relieves the quenched-in stresses and improves the magnetic properties of the material and may also change the ductility, viscosity and density of the sample [17]. Commercial annealing is performed in a furnace of the type shown in Fig.2.6.1 with inert atmosphere and strict temperature control [28]. For magnetic annealing, a field is applied to the core in a direction depending on its intended application. During commercial annealing the temperature is monitored at different sections of the ribbon as shown in Fig.2.6.2.

Annealing in a nitrogen atmosphere is said to reduce core losses compared to annealing in air because boron has a tendency to oxidise on the surface of the ribbon

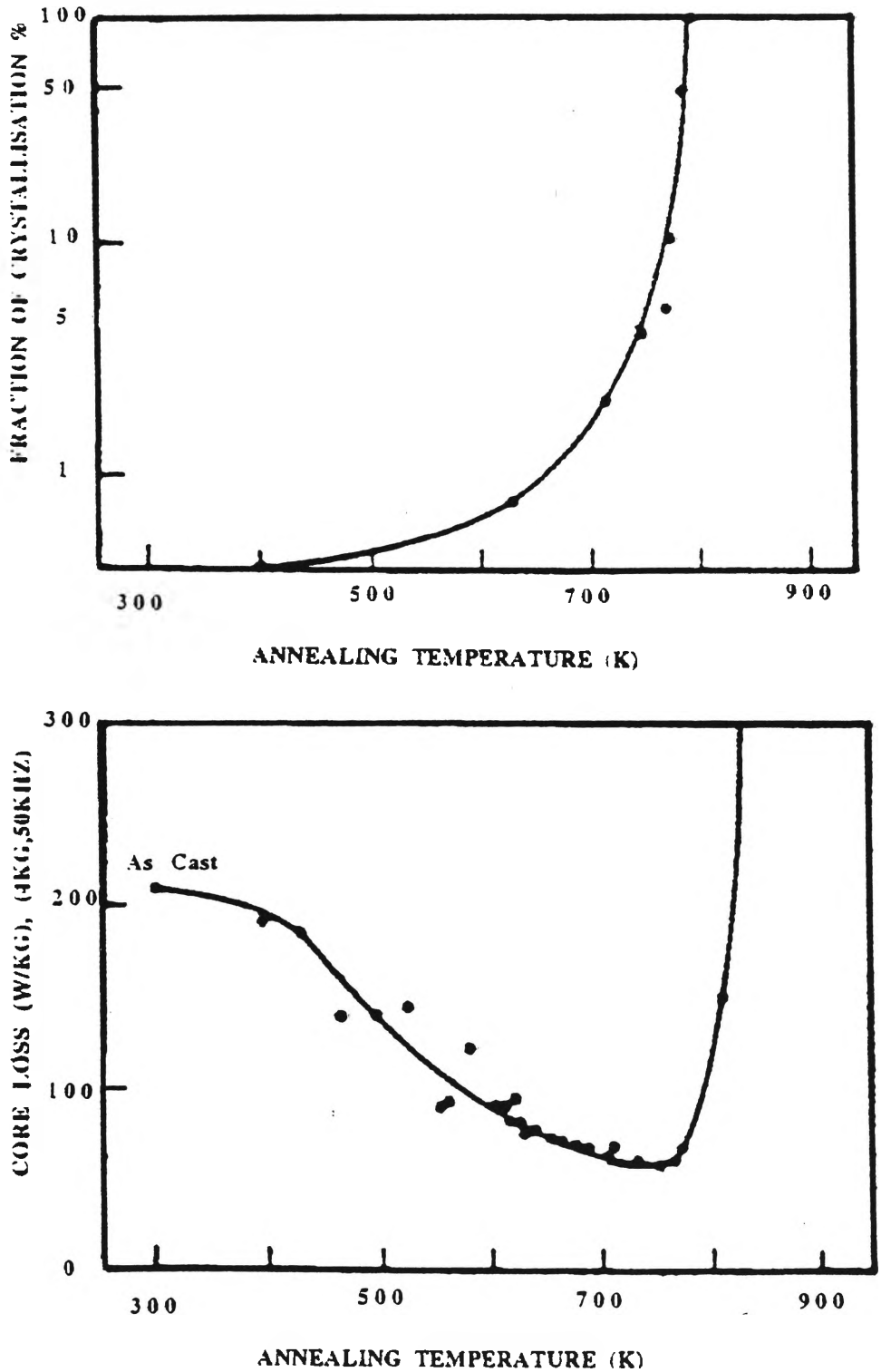

Fig.2.5.9 Decrease in core loss with the introduction of precipitates in $Co_{bal}Fe_4Ni_2Si_{15}B_{14}$ (METGLAS® 2714A) [27].

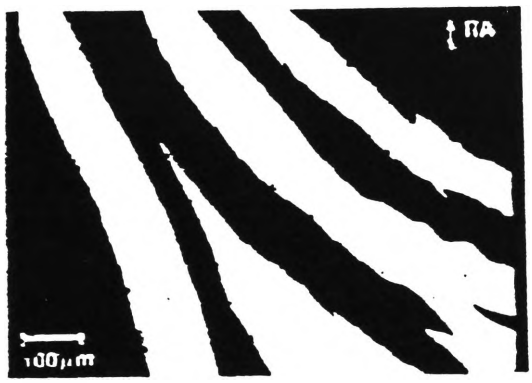

(a) annealed for 15 mins. at 633 K

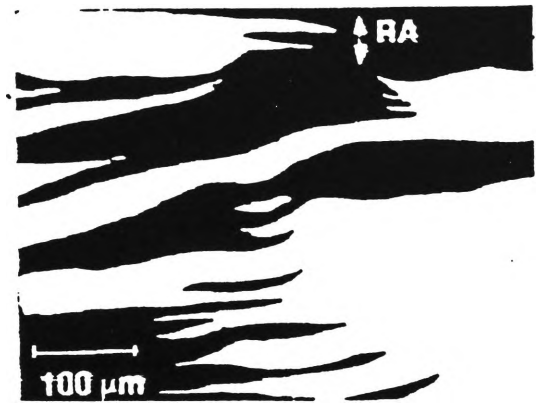

(b) annealed for 15 mins. at 673 K

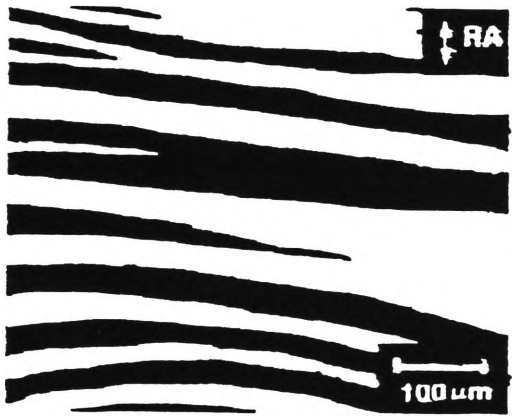

(c) annealed for 15 mins. at 653 K

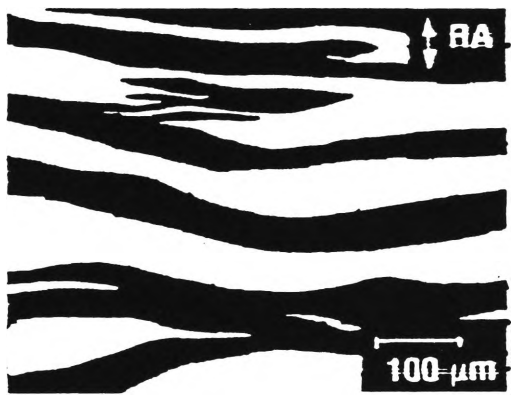

(d) annealed for 15 mins. at 713 K

Fig.2.5.10 Tracings of scanning electron micrographs from the metallic glass $Fe_{75}Ni_4Mo_3B_{16}Si_2$. Note the change in direction of the domains with respect to the ribbon axis (RA) [26].

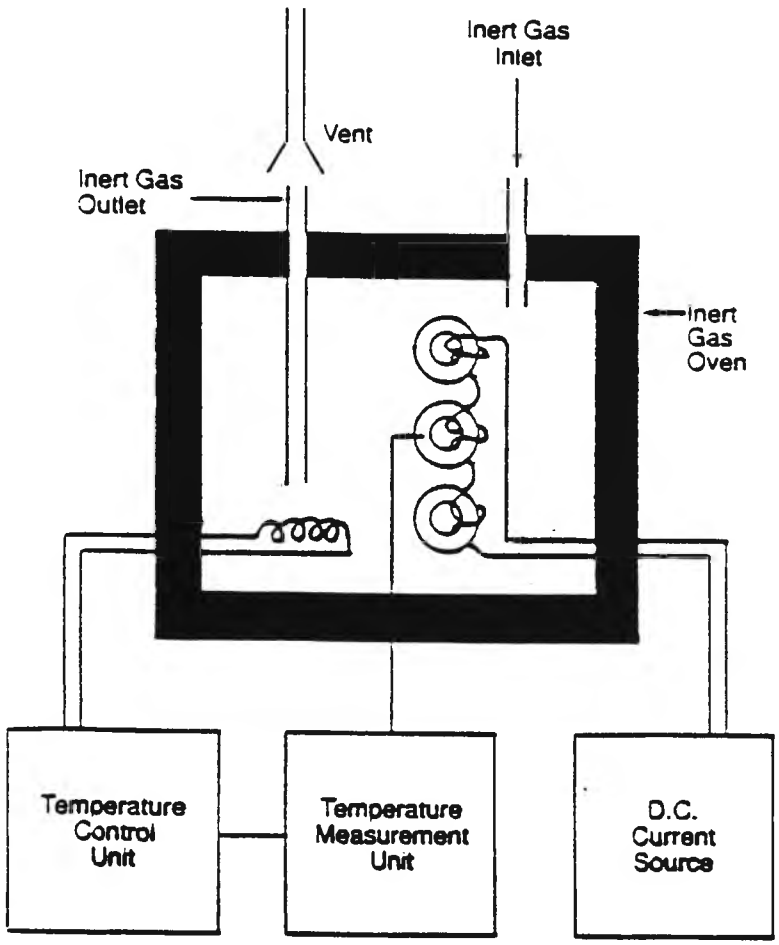

Fig.2.6.1 Commercial annealing furnace [28].

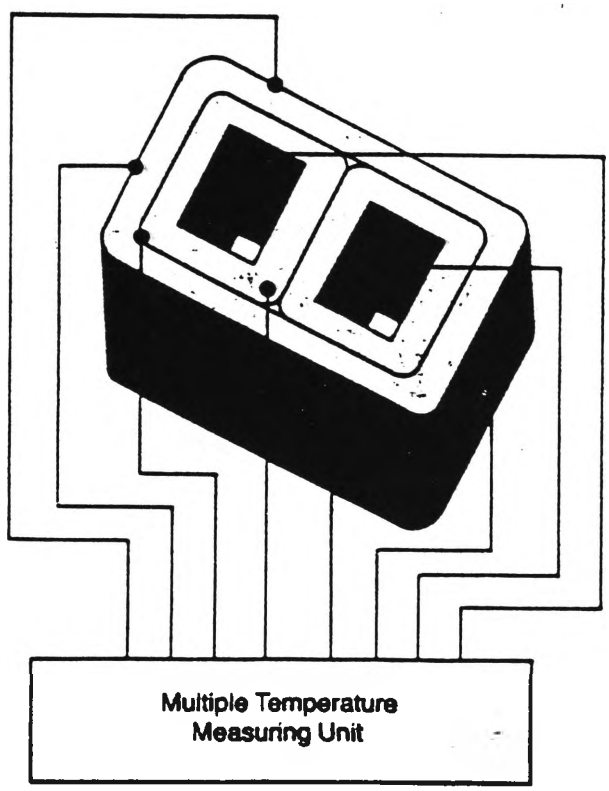

Fig.2.6.2 Multiple temperature measuring unit used to monitor temperature of large core [28].

when the boron-containing ribbon is annealed in an oxidising atmosphere [22]. Oxidation may cause local crystallisation and, as a result, magnetic properties deteriorate.

The low temperature annealing of metallic glasses has two functions [25]:

1) heat treatment at relatively lower temperatures relieves the stresses induced during casting and minimises stress anisotropy. As a result, one impediment to domain alignment is removed and this increases the ease with which domains align in the direction of the external magnetic field, therefore increasing the maximum permeability [17].
2) annealing in a magnetic field below the Curie temperature causes atomic ordering which induces an anisotropy in the sample. If the anisotropy is induced along the direction of magnetisation during use then the sample magnetises easily and excellent soft properties are obtained.

During the annealing of amorphous alloys, three types of atomic arrangements occur, prior to crystallisation [29]:

i) compositional short-range-order (CSRO)

ii) diffusion

iii) topological short-range-order (TSRO)

On annealing the amorphous alloys, unlike atoms interchange their position. This type of short-range-ordering is called compositional short-range-ordering. In ferromagnetic atomic species, this type of ordering gives rise to metal-metal atomic pairs and as a result, the Curie temperature (T_C) increases [25,30,31] and changes in magnetic anisotropy also occur.

In topological short range ordering (TSRO), each atom in the amorphous alloy retains its neighbours but the interatomic distances and angles are slightly changed and hence the atoms in the random structure become more densely packed [31].

Due to the change in structure during stress relief annealing, the density of the material also changes by approximately 0.1 to 0.2%. The density of the amorphous alloys is approximately 2% lower than that of their crystalline counterparts [32,33,34].

The structural relaxation in the metallic glasses is due to both CSRO and TSRO.

If an amorphous alloy has $T_C < T_X$ (T_C is Curie temperature and T_X is crystallisation temperature) then annealing in an external magnetic field below T_C induces an anisotropy known as field-induced anisotropy. This anisotropy can be explained in light of the directional CSRO. Due to magnetic annealing, the magnetic moments in each domain are aligned in the direction of the applied magnetic field [30]. Generally, field annealing is carried out at higher temperatures but below the Curie temperature for better results [35]. This produces a square hysteresis loop which has easy magnetisation. If annealing is carried out in the absence of a magnetic field below T_C then the domain walls are pinned due to inducement of anisotropy. This results in stabilisation of domain walls and an increase of coercivity and core loss [17]. If the annealing is carried out above T_C then the effect of magnetic and non magnetic annealing is the same. If $T_C > T_X$ then annealing is carried out in rotating magnetic field below T_X [17,36] so that internal stresses are relieved without inducing uniaxial anisotropy.

The shape of the hysteresis loop also depends upon the different magnetic annealing treatments. Fig.2.6.3 shows this effect for a $Fe_{39}Ni_{39}Mo_4Si_6B_{12}$ alloy [8].

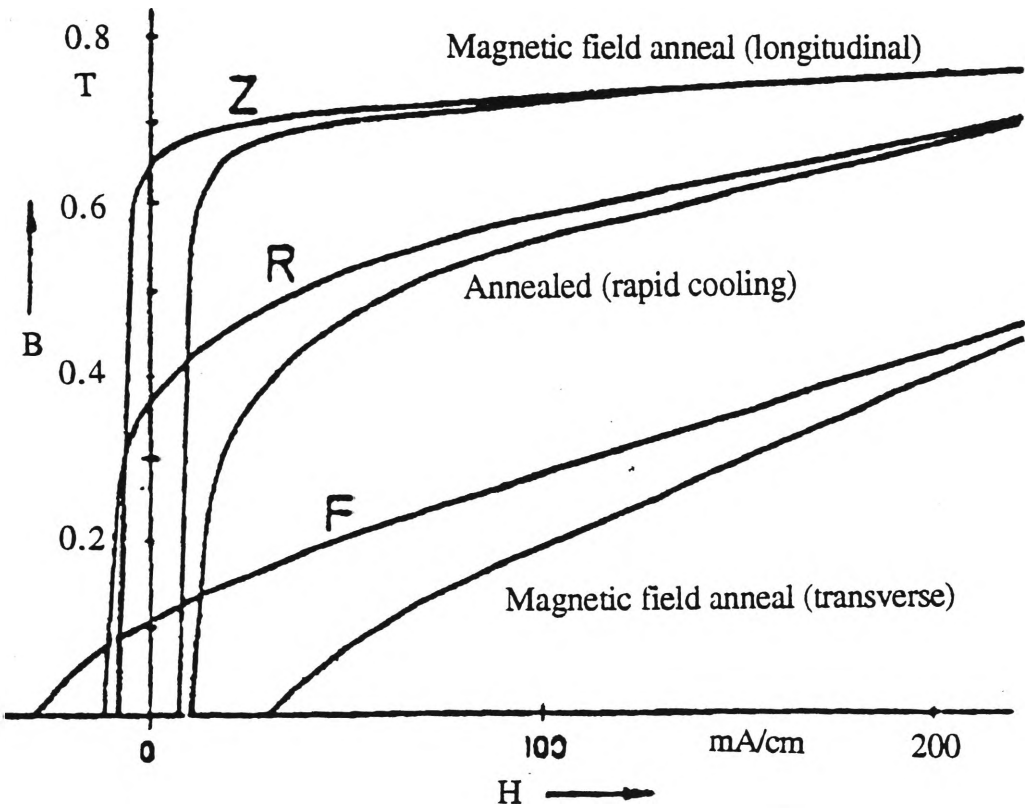

Fig.2.6.3 Hysteresis loops of $Fe_{39}Ni_{39}Mo_4Si_6B_{12}$ ribbon under different annealing treatments [8].

1) Rectangular hysteresis loops (Z type) are produced if the sample is subjected to longitudinal magnetic field annealing and slow cooling below T_C (e.g. at 100°C/h). This introduces high field-induced anisotropy. The shape of the loop indicates that the domains are aligned parallel to the applied magnetic field. These Z type loops have a small coercive field strength and an easy approach to saturation.
2) Round hysteresis loops (R type) are produced if the sample is rapidly cooled (e.g. at 1000°C/h) after conventional annealing. The R type loop is obtained because a small value of field-induced anisotropy is introduced.
3) Flat hysteresis loops (F type) are produced if the sample is annealed in a transverse magnetic field and slowly cooled below T_C. This introduces transverse field-induced anisotropy and high initial permeability.

Magnetic annealing reduces the magnetic field strength required to obtain a specific magnetisation condition, thereby reducing core loss [37]. The difference in core loss with and without magnetic annealing is shown in Fig.2.6.4 [22]. The change in the shape of the hysteresis loop due to non-field and field annealing in METGLAS® 2714A alloy is shown in Fig.2.6.5 [28].

Magnetostrictive anisotropy due to internal stresses can be annealed out by a heat treatment at temperatures high enough to induce sufficient diffusion [30].

If the annealing is carried out with the sample under stress then stress-induced anisotropy appears [33]. This anisotropy is larger than the field-induced anisotropy and it can appear even above the Curie temperature. The stress plus field-induced anisotropy is greater than the individual stress or field-induced anisotropies alone but it is not the sum of both anisotropies [33].

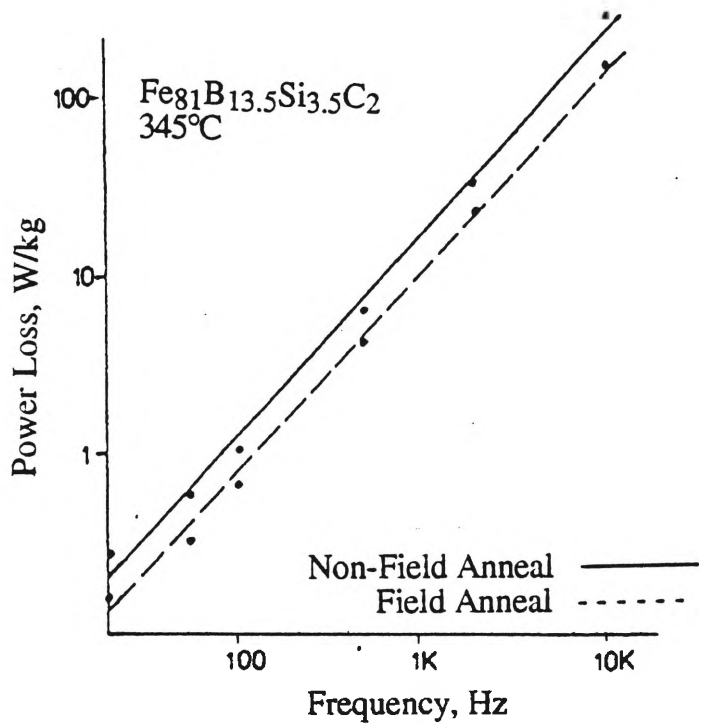

Fig.2.6.4 Variation of power loss with frequency for $Fe_{81}B_{13.5}Si_{3.5}C_2$ ribbon annealed with and without an applied magnetic field [22].

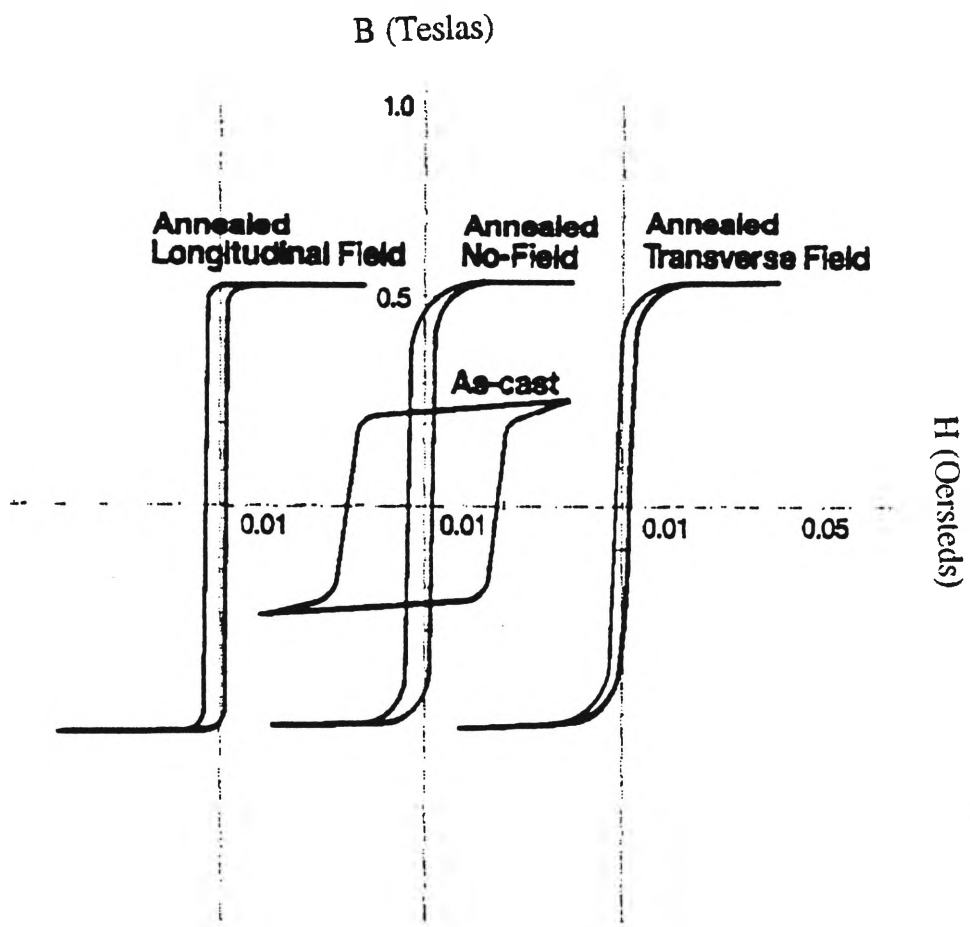

Fig.2.6.5 The effect of field and non-field annealing on the shape of hysteresis loops in METGLAS® 2714A [28].

The embrittlement of metallic glasses during stress relief annealing is a major disadvantage. During the annealing, excess free vacancies in the material are removed and result in an increase in viscosity. The increased viscosity is thought to reduce the ability of the glass to deform plastically ahead of growing crack tips and hence produces embrittlement [38].

2.7 Asymmetrically displaced hysteresis loop

When crystals form in some cobalt-based alloys, the hysteresis loop is asymmetrically displaced [39,40,41] as shown in Fig.2.7.1. If the annealing is carried out in a magnetic field, then the shift of the hysteresis loop is much higher than that of annealing in the absence of a magnetic field as shown in Table 2.7.1 [39]. The shift of the hysteresis loop increases with an increase in temperature as shown in Fig.2.7.2. If the hysteresis loop is measured by applying a magnetic field perpendicular to the magnetic path of the core, then the hysteresis loop may originate from the centre as shown in Fig.2.7.3 [39]. The cause of the shift in cobalt-based alloys is not yet known but different suggestions have been put forward. Surface crystallisation could be one of the reasons [40] although this is disputed by Yamauchi and Yoshizawa [39]. Kohmoto et al. [41] have suggested that the cause of the shift is the presence of two phases in the sample, one crystalline with high coercivity and the other the amorphous matrix with lower H_C. When the sample is magnetised, all the domains align in one direction. When the magnetisation field is reversed, the magnetisation vector in the crystalline region opposes the rotation of the domains and as a result, the shift occurs in Co-based alloys. This topic is discussed further in Section 5.5.

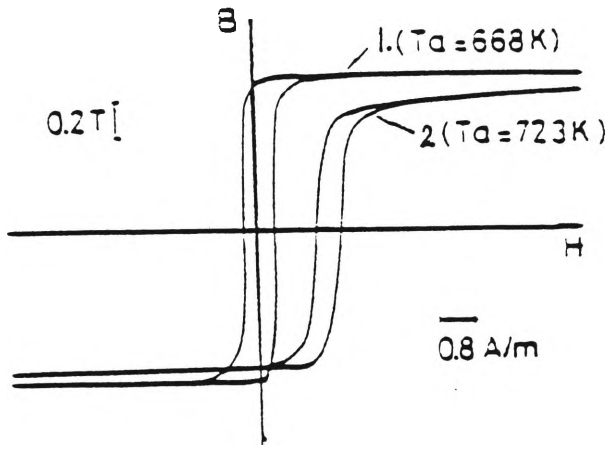

(a) Symetrical and asymmetrical BH loops of $(Co,Fe,Mn,Nb)_{76}Si_{15}B_9$ annealed for 30 mins. at (1) 668 K and (2) at 723K [39].

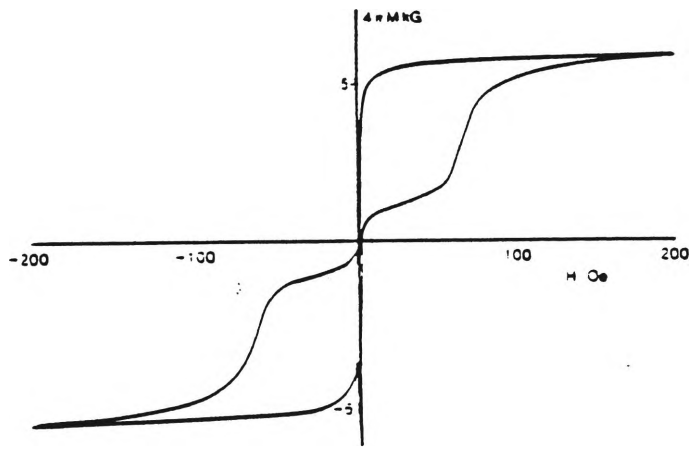

(b) Asymmetrically displaced hysteresis loop of $Co_{66}B_{30}Si_4$ annealed for 15 mins. at at 550°C [40].

Fig.2.7.1 Asymmetrically displaced hysteresis loops of some cobalt-based alloys.

W.Q.: Annealed at 708 K for 0.5 h, water quenched;
M.F.A.: Annealed at 708 K for 0.5h, water quenched;
again annealed at 493 K for 4 h in magnetic field

Composition	W.Q.		M.F.A.	
	ΔH_s(A/m)	H_c(A/m)	ΔH_s(A/m)	H_c(A/m)
$(Co,Fe)_{75}B_{25}$	0	7.84	13.6	6.96
$(Co,Fe,Mn)_{75}B_{25}$	0.08	1.28	0.16	1.24
$(Co,Fe)_{76}Si_{15}B_9$	0.40	0.80	3.28	0.96
$(Co,Fe,Mn,Nb)_{76}Si_{15}B_9$	0.08	0.32	1.12	0.80

Table 2.7.1 H_c and ΔH_s of typical cobalt-based amorphous alloys [39].

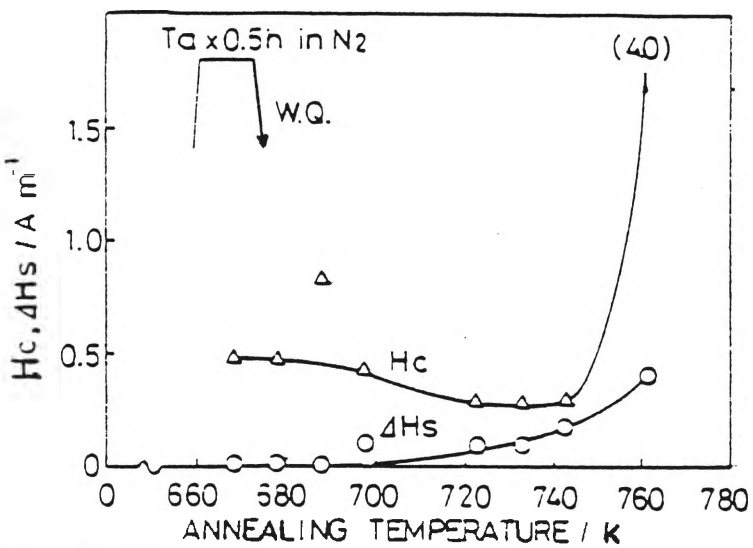

Fig.2.7.2 Change of H_c and ΔH_s in $(Co,Fe,Mn,Nb)_{76}Si_{15}B_9$ alloy as a function of annealing temperature T_a [39].

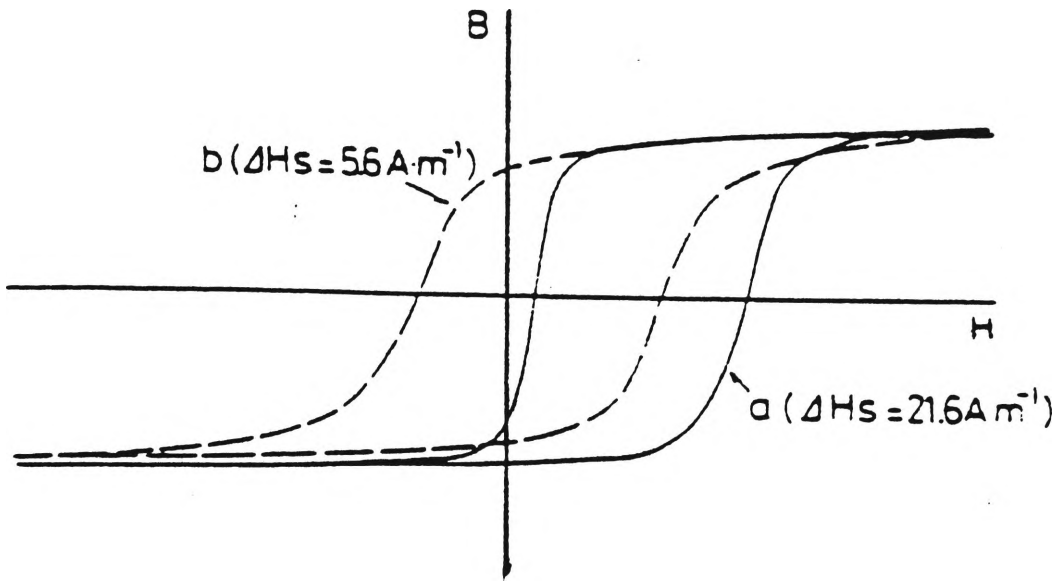

Fig.2.7.3 The effect of applied magnetic field on asymmetrically displaced hysteresis loops [39].

(a) measured as annealed in magnetic field

(b) measured after applying a magnetic field of 184 A/m perpendicular to the magnetic path.

Note that ΔH_s is reduced.

Chapter 3

3.0 EXPERIMENTAL WORK

3.1 Alloy and Ribbon Preparation

All the metallic ribbons investigated were prepared from high purity components (see Table 3.1.1). 10 g of constituents were alloyed by induction heating under a reduced argon atmosphere. These alloys were then homogenised by remelting the alloy buttons on a water-cooled copper hearth in an arc furnace again under an argon atmosphere. The alloy buttons were cast into rods, suitable for the melt-spinning crucible, while they were still in the arc furnace.

Ribbons were made by planar flow casting (PFC) on a stainless steel wheel 300 mm in diameter. PFC operational parameters are given in Table 3.1.2.

$Co_{75}Si_{10}B_{15}$ and $Fe_{72}Si_{10}B_{18}$ ribbons were prepared for the experiments presented in this work, while a $Fe_{60}Ni_{20}Si_{10}B_{10}$ ribbon was already present in the department. This ribbon was wider then the slot in the secondary coil used for the magnetic measurements, hence it was cut along the thinnest part across the length. Care was taken while cutting to minimise strain in the ribbon.

3.2 Density Measurement

The density of the amorphous alloys is required for the calculation of core loss measurements in the magnetic testing.

The most common method for density measurements of solids is that which uses Archimedes' law. Reproducibility of the measurements in a liquid medium is

Element	Purity (wt. %)
Co	99.6
Si (pieces)	99.999+
B (pieces)	99.9
Fe (rod)	99.98

Table 3.1.1 Percentage of purity of the elements used in ribbon preparation.

Alloy Composition	PFC Wheel Speed (r.p.m.)	PFC Ejection Pressure (k Pa)	Ribbon Thickness (μ)
$Co_{75}Si_{10}B_{15}$	2000	70	40
$Fe_{72}Si_{10}B_{18}$	2000	70	30
$Fe_{60}Ni_{20}Si_{10}B_{10}$	-unknown-	-unknown-	25

Table 3.1.2 Planar flow casting (PFC) operational parameters and ribbon thickness.

restricted by the nonreproducibility of the surface tension forces (meniscus effect) and trapping of gas bubbles on the surface of the specimen. Konczos and Sas [33] found that toluene has a more stable meniscus than the normally-used high density organics such as bromoform or tetrabromethane.

A jig similar to that described in Ref. 33 was prepared using 0.3 A tinned copper fuse wire to support the specimen in the measuring liquid. This jig was designed to fit a Mettler AE240 balance. It was found that the density measurement was reproducible if the mass was measured with sufficient accuracy. Fig.3.2.1 shows the density measuring jig of Ref. 33. The density measured for different alloy compositions is given in Table 3.2.1.

3.3 Annealing Procedure

Metallic glass strips were cut with a sharp guillotine into 10 cm lengths. Two 10 cm long ribbons were sealed in a glass tube under a low pressure argon atmosphere because it has been shown by Overshot and Price [22] that annealing in air produces samples with a greater core loss than those annealed in a non-oxidising atmosphere. Care was taken during sealing that the ribbon did not get hot. The sealed glass tube was then placed in a small resistance furnace and annealed while subjected to a 795 A/m DC magnetic field along the axis of the ribbon. A magnetic shield, made from a mild steel cylinder (diameter 50 mm), was placed around the magnetic coil and sample assembly to isolate the sample from other magnetic fields which may arise from the furnace winding or the Earth's magnetic field. After annealing for 1 hr, the ribbons were taken out of the furnace. During annealing, the temperature was measured by a K-type thermocouple placed in an identical glass tube adjoining the one which contains the sample. The temperature was measured with a Fluke model 52 thermometer, which contains cold junction compensation. The arrangement of the annealing equipment is shown in Fig.3.3.1.

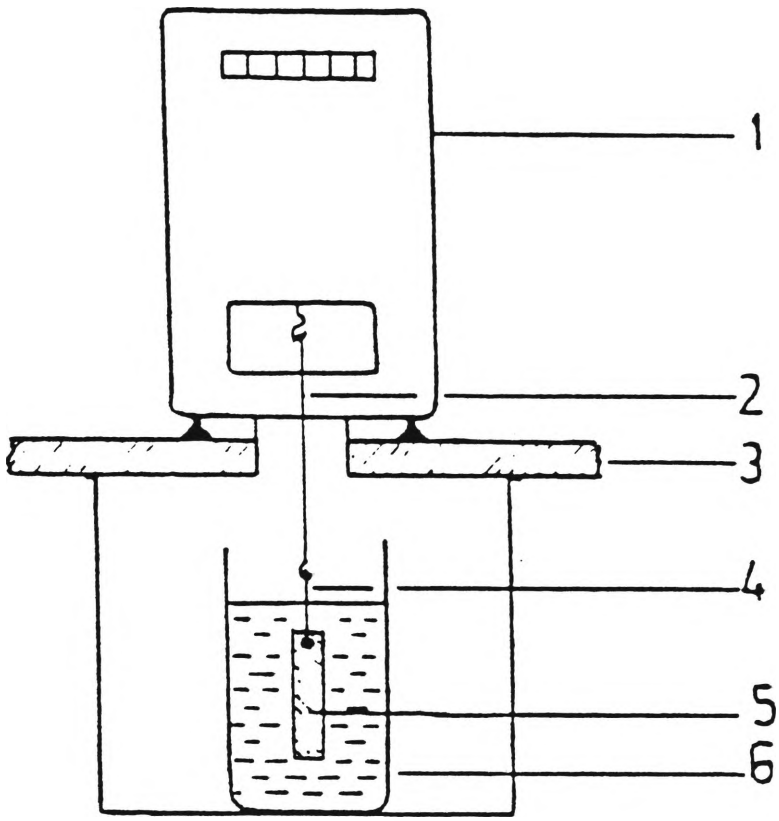

Fig.3.2.1 Density measurement apparatus for metallic glasses [33].

1- digital electronic microbalance

2- quartz fibre

3- table

4- gold plated tungsten wire

5- sample

6- glass filled with organic liquid.

Alloy composition	Density (gm/cm^3)
$Co_{75}Si_{10}B_{15}$	7.84
$Fe_{60}Ni_{20}Si_{10}B_{10}$	7.21
$Fe_{72}Si_{10}B_{18}$	6.95

Table 3.2.1 Density of alloys used in this work.

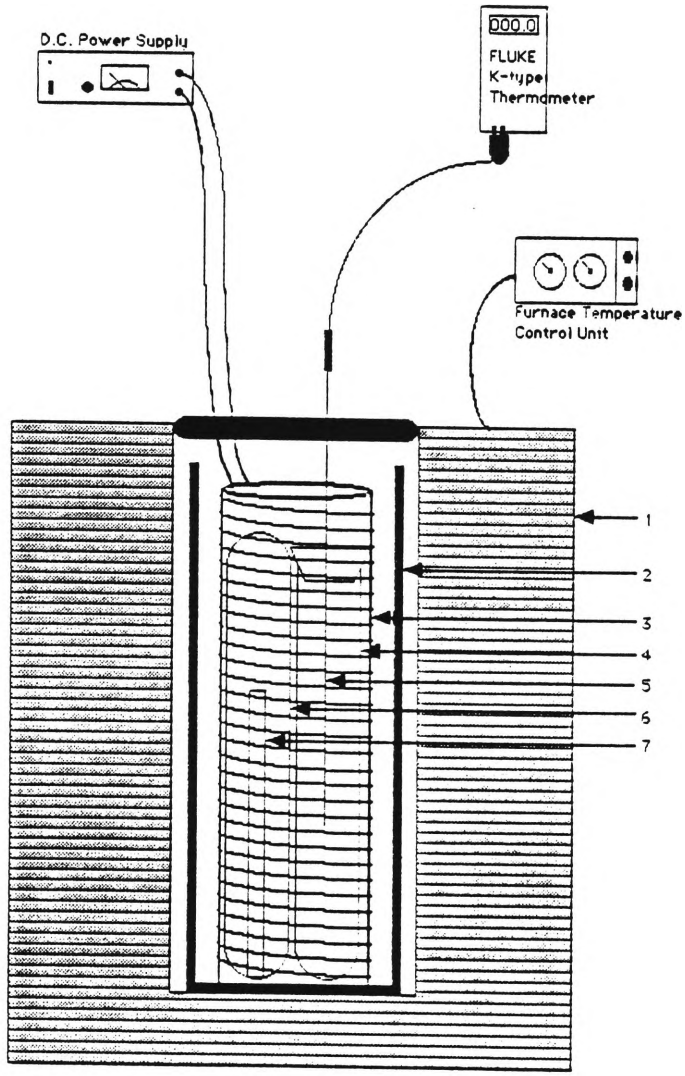

Fig.3.3.1 Annealing equipment

1- resistance furnace

2- magnetic shield

3- solenoid for DC magnetic field

4- reference glass tube in which temperature is measured

5- thermocouple

6- sealed glass tube

7- metallic ribbon

3.4 Magnetic Testing Technique

Magnetic measurements were carried out on both as-cast and annealed 10 cm lengths of ribbon using a computer-assisted method [14] as described below. The advantage of this method is that it allows magnetic properties of a material to be measured without winding primary and secondary coils for different samples. The schematic diagram is shown in Fig.3.4.1.

The solenoid (primary coil) was made by winding a single layer of 660 turns of 0.5 mm enamelled copper wire around a cylindrical Perspex former 300 mm long and 30 mm outer diameter. This ensures that the magnetic field in the central 100 mm region is reasonably homogeneous. The search coil (secondary coil) consists of 200 turns of very fine enamelled copper wire wound closely around the central 10 mm section of a 100 mm X 10 mm single strip of metallic glass. The search coil is loose enough to allow the sample to be slipped in or out.

The solenoid is driven by a sinewave generator (Silicon Chip digital sine/square generator) via a LM1875T audio power amplifier IC. The voltage induced in the search coil, (proportional to dB(t)/dt), is fed directly into the Y-channel of a Hitachi VC-6050 8 bit digital storage oscilloscope. The magnetising current passing through the solenoid is measured from the voltage across a 46 ohm resistor placed in series with the solenoid. This voltage is fed to the X-channel of the oscilloscope. The digital storage oscilloscope has the facility of adding the X and Y channel signals to previous accumulations and then obtaining an average. This improves the quality of the signal by increasing the signal to noise ratio. A maximum of 256 accumulations can be carried out. This is an advantage over systems which use an analog multiplier [10] to multiply the instantaneous waveforms of H(t) and dB(t)/dt. Since the data analysis was carried out via software (written in Quick Basic), several properties could be displayed simultaneously. The only parameters required by the program are the density of sample,

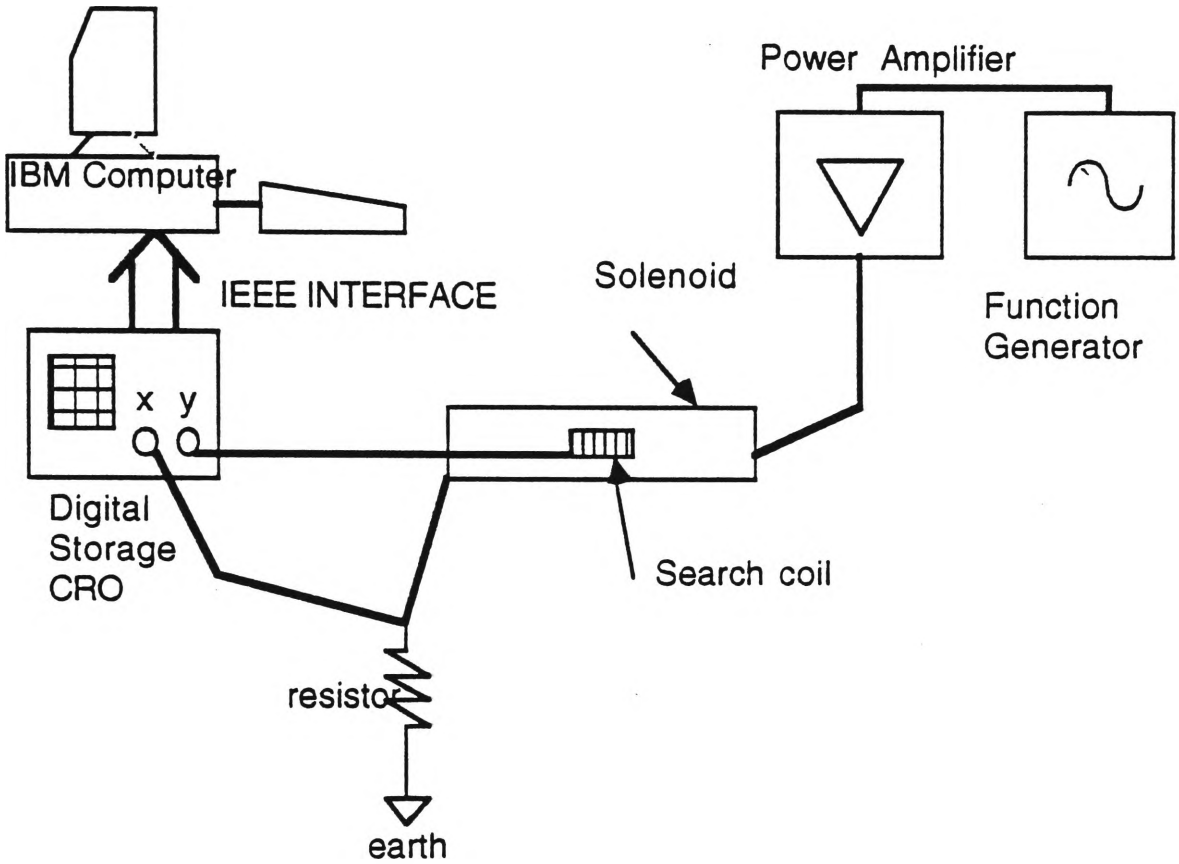

Fig.3.4.1 Set-up of the magnetic measurement instrument.

its cross-sectional area and the frequency. The X and Y channel data were transferred from the oscilloscope to the computer via an IEEE-488 (GPIB) interface. The resolution of the sinusoidal data, from the X-channel, was increased by fitting it to a sinusoidal curve within the program which improved the accuracy of the results. Since the sample was loose enough to be slipped in or out of the search coil, this meant that there is space between the sample and the search coil. As a result, a minute contribution to the induced voltage in the search coil originates from the applied magnetic field, H(t), in this space. This was subtracted mathematically. This is known as an air flux correction. The core loss was calculated using the following formula:

$$P = \frac{f}{\rho}\int_0^{1/2\pi f} H(t)\,\frac{dB(t)}{dt}\,dt$$

where f is the frequency

ρ is the density of the material

H(t) calculated from X-channel data

dB(t)/dt from Y-channel data

Here H(t) is sinusoidal and since dB(t)/dt is periodic, the integration is carried out over one cycle ($1/2\pi f$). This eliminates the contribution to the core loss from any harmonics present in the dB(t)/dt data. The demagnetising factor(N_{zz}) was calculated from the following equation:

$$N_{zz} = 0.45\left\{4\pi - 8\arctan\left\{\frac{\sqrt{10^2 + 100^2}\ \text{x}\ 100}{\text{cross-section}}\right\}\right\}$$

This equation is an application of the result presented by Joseph and Schlomann [11]. The Y channel data were integrated using the trapezium method in order to obtain B(t). The hysteresis loop could then be displayed. The two X-intercepts of the hysteresis loop were used to calculate the coercivity ($H_c = (H_{c1} - H_{c2})/ 2$) and horizontal shift ($\Delta H_s = (H_{c1} + H_{c2})/ 2$) due to the Earth's magnetic field or other sources. The

remanence was obtained from the Y-axis intercepts of the hysteresis loop. The software allows the user to view, save or load the data at any stage in the analysis.

During magnetic measurements, the following points must be taken into consideration to increase the accuracy of the results:

1) The primary coil must be placed exactly in a magnetic east-west direction to null out the effect of the Earth's magnetic field. If the solenoid is not aligned this way, then the Earths magnetic field will shift the hysteresis loop horizontally. The alignment of the solenoid can be checked by using an as-cast sample of ribbon and rotating the solenoid until the shift due to the Earth's magnetic field is 0.5 A/m or less. The solenoid can also be aligned with the aid of a compass.
2) The test sample must be parallel to the axis and in the centre of the primary coil where a uniform magnetic field is produced.
3) Any noise superimposed on the H(t) or dB(t)/dt voltages must be reduced by averaging over a number of repeated accumulations using the oscilloscope.
4) X and Y channel signals must be collected simultaneously.

<u>Limitations and difficulties with the magnetic measurement instrument :</u>

1) The maximum operating frequency (50 kHz) of the equipment is limited by the cut-off frequency of the power amplifier and the resolution of the oscilloscope.
2) For low frequency measurements the signals are very weak and electrical noise further reduces the signal to noise ratio (S/N) of the dB/dt waveform. In this case a large number of signals are collected and averaged in order to increase the S/N. However, even with the maximum 256 accumulations, the signal to noise ratio at 1 Hz does not reach the same level as that for higher frequencies.
3) Acoustic noise, due to magnetostriction of Fe alloy samples at higher frequencies, influenced the position of the dB/dt waveform. As a result of

acoustic vibrations, the sample's position in the solenoid shifted slightly, hence it was realigned after each set of high frequency measurements.

4) At high magnetic field strength and high frequency, the back emf in the magnetising coil starts to become noticeable as the field strength starts to deviate from a sinusoidal shape.

3.5 Differential Scanning Calorimetry

A Mettler TA3000 Series DSC30 instrument was used to determine the peak crystallisation temperature and the Curie temperature of the metallic ribbons.

When a sample crystallises it releases heat energy which appears as an exothermic peak on the DSC trace. The area under exothermic peak is calculated to determine the total heat release during crystallisation. The temperature corresponding to the peak is known as the crystallisation temperature. Around the Curie temperature, electrons absorb energy from the system and as a result their magnetic alignment is disturbed. This removal of energy from the system decreases its heat capacity which is evident on the DSC trace as an endothermic peak [42].

The endothermic peak corresponding to the Curie temperature of some ferromagnetic alloys was not easily detected by the DSC. In these cases a magnetic susceptibility method was used to determine the Curie temperature.

3.6 Optical Microscopy and Transmission Electron Microscopy

It is extremely useful to correlate magnetic measurements with optical or electron metallographic evidence. Low magnification structural investigations were conducted using a Nikon Optiphot optical microscope while higher magnification

microstructural examination was carried out on a Jeol JEM-2000FX transmission electron microscope (TEM).

Optical microscope observations were conducted on polished and etched samples of partially-crystallised glassy ribbon specimens mounted in a cold-setting resin. Due to the extremely brittle nature of the heat treated ribbon, the specimens had to be carefully ground, initially on 600 grit and finally on 800 grit SiC paper, before being polished on 6 micron and 1 micron diamond laps, to minimise fragmentation of the samples. A list of etchants used for the various alloy compositions is given in Table 3.6.1.

In some cases optical microscopy was carried out before and after removing the surface of the annealed specimen. The surface of the sample was removed using dilute nitric acid.

The foils required for the TEM investigations were initially produced in a Struers Tenupol twin-jet electro-polisher, however it was found that a dimple grinder gave better and quicker thinning of the foil. Approximately 10-15 microns of the surface of the foil were removed from both sides, and the final thinning was done in an Edwards Auto 306 ion beam thinner.

Alloy composition	Etchant
Co-Si-B	Acidic Ferric Chloride
Fe-Ni-Si-B	10% Nital
Fe-Si-B	10% Nital

Table 3.6.1 List of chemical etchant used for optical metallographic investigations.

Chapter 4

4.0 RESULTS

4.1 Results calculation

The results shown in this chapter for $Co_{75}Si_{10}B_{15}$, $Fe_{72}Si_{10}B_{18}$ and $Fe_{60}Ni_{20}Si_{10}B_{10}$ ribbons were arranged and calculated using following procedure, taking one set of results as an example.

Fig.4.1.1 shows the shapes of hysteresis loops generated at different applied magnetic fields, at 400 Hz frequency, for $Fe_{60}Ni_{20}Si_{10}B_{10}$ ribbon annealed for 60 mins. at 343°C. As the applied magnetic field (H) is increased the induction (B), coercivity (H_c), remanence (B_r) and core loss (L_T) increases. The values corresponding to each hysteresis loop of Fig.4.1.1 are shown in Table 4.1.1.

The values in Table 4.1.1 were used to plot B vs. H, L_T vs. B, H_c vs. B as shown in Fig.4.1.2. Fig.4.1.2a is effectively the initial magnetisation curve. At the knee of the initial magnetisation curve the value of B/H is maximum called the maximum permeability (μ_{max}). It is a dimensionless quantity. Since the value of H is in A/m, it is converted into Tesla by multiplying by the value of the permeability of free space ($\mu_0 = 4\pi \times 10^{-4}$) to calculate μ_{max}. Fig.4.1.2b and Fig.4.1.2c are used to find core loss and coercivity at particular induction (B). Tables similar to Table 4.1.1 were obtained for all frequencies i.e. 50 Hz, 400 Hz, 1 kHz, 5 kHz, 10 kHz, 25 kHz and 50 kHz at each annealing temperature, (which depends on the Curie temperature (T_c) and crystallisation temperature (T_x) of the material under investigation). From these data, plots similar to that of Fig.4.1.2 were plotted for each alloy. This calculated data was then used to plot the core loss (L_T) vs. annealing temperature (T_a), coercivity (H_c) vs. annealing temperature (T_a), and maximum permeability (μ_{max}) vs. annealing temperature (T_a).

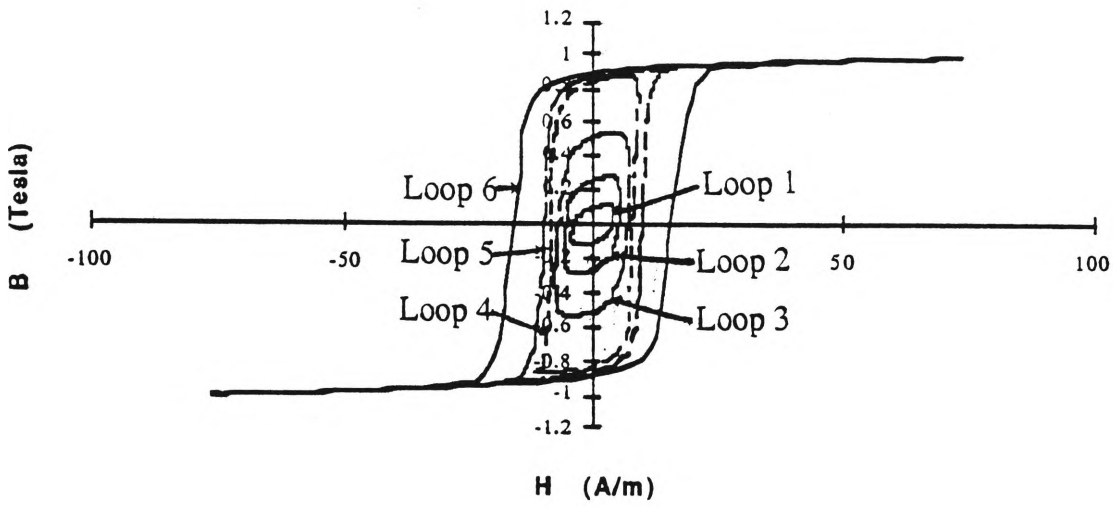

Fig.4.1.1 The shape of hysteresis loops at different applied magnetic field for $Fe_{60}Ni_{20}Si_{10}B_{10}$ ribbon , with 400 Hz operating frequency, annealed for 60 mins. at 343°C.

Loop No.	Applied magnetic field (H) A/m	Magnetic Induction (B) Tesla	Coercivity (H_c) A/m	Remnance (B_r) Tesla	Core loss (L_T) W/kg	Frequency (f) Hz	Shift (ΔH_s) A/m
1	3.16	0.12	3.72	0.10	0.08	401	0.04
2	3.87	0.28	5.41	0.26	0.29	402	0.12
3	4.49	0.54	6.85	0.51	0.72	401	0.19
4	7.67	0.87	8.18	0.82	1.51	401	0.51
5	16.28	0.92	9.71	0.86	1.91	401	0.17
6	70.81	1.00	15.75	0.89	3.25	400	-0.42

Table 4.1.1 Data for Fig.4.1.1.

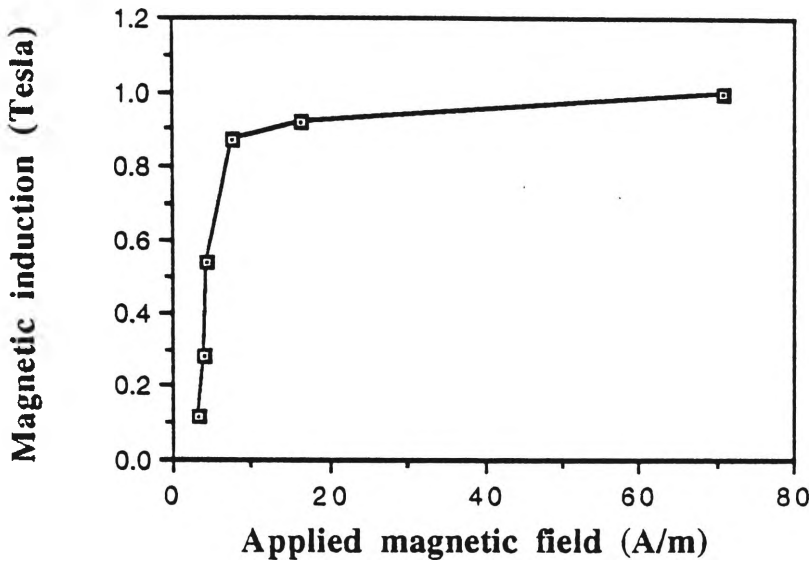

Fig.4.1.2a The maximum value of B/H is obtained at the knee of the curve. This is the maximum permeability, (μ_{max}).

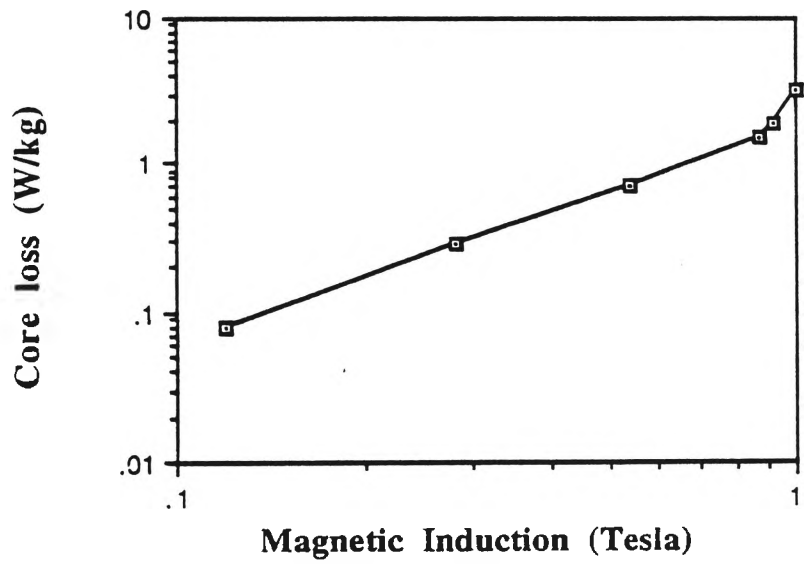

Fig.4.1.2b Core loss as a function of magnetic induction.

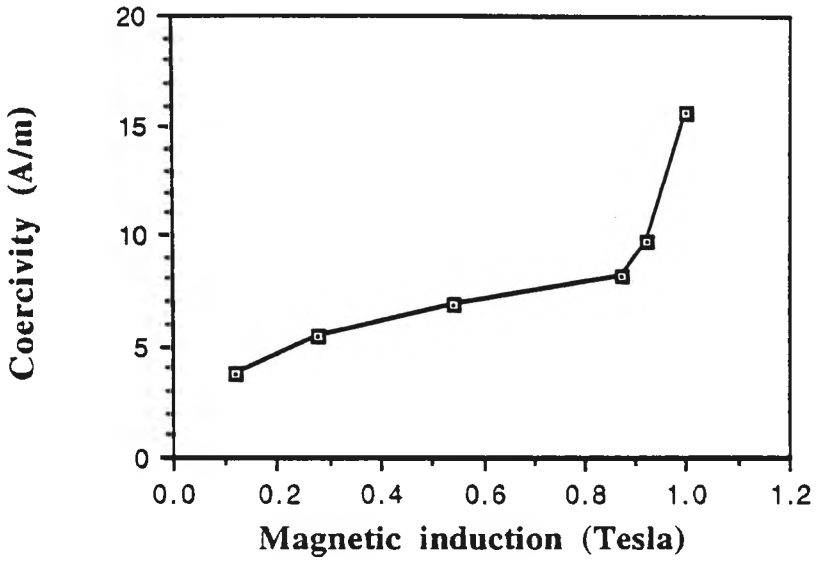

Fig.4.1.2c Coercivity as a function of magnetic induction.

4.2 Magnetic properties of $Co_{75}Si_{10}B_{15}$ ribbon

The crystallisation of the $Co_{75}Si_{10}B_{15}$ alloys was measured by dynamic DSC at a rate of 20°C/min. The thermogram showed two peaks, the first peak at 521°C and a large second peak at 564°C as shown in Fig.4.2.1. The endothermic peak corresponding to the Curie temperature was not distinguishable on the DSC trace for these alloys, hence the Curie temperature was measured by the susceptibility method. The Curie temperature of this alloy is approximately 360°C as shown in Fig.4.2.2.

The changes in the core loss (L_T) with annealing temperature (T_a) at 0.6 Tesla induction for different frequencies are shown in Figs.4.2.3. Fig.4.2.4 combines the information for Fig.4.2.3 on a single graph. As the annealing temperature increases, the core loss decreases up to a certain temperature and then starts to increase rapidly as the soft magnetic properties deteriorate. The core loss increases sharply when the sample has begun to crystallise. At lower frequencies the minimum core loss is obtained at lower annealing temperatures while at higher frequencies the minimum core loss is obtained at higher annealing temperatures. The core loss values at all frequencies for the ribbon annealed at 472°C have been estimated by extrapolating the log-log graph of core loss vs. induction because to reach the induction of 0.6 Tesla, a very high applied magnetic field is required. Due to the limitations of the instrument these higher magnetic fields could not be achieved.

The coercivity (H_c) vs. annealing temperature (T_a) plot at 0.6 Tesla induction is shown in Fig.4.2.5. The coercivity changes with annealing temperature. At lower frequencies, it is a minimum at the same annealing temperature at which the core loss is minimum but at higher frequencies the coercivity is not a minimum at the same temperature at which the core loss is minimum. As the material loses its soft magnetic properties on crystallisation, the coercivity increases sharply.

Fig.4.2.6 shows the maximum permeability (μ_{max}) vs. annealing temperature (T_a) graph at different frequencies. The value of maximum permeability is high for lower operating frequencies and lower at the higher operating frequencies.

Fig.4.2.7a shows the comparison of the core loss at different inductions, for 50 Hz operating frequency, between as-cast ribbon and ribbon annealed at 384°C for 60 mins. Fig.4.2.7b shows the comparison of the core loss at different inductions, for 50 kHz operating frequency, between as-cast ribbon and ribbon annealed at 446°C for 60 mins. These are the temperatures at which core loss is at a minimum for 50 Hz and 50 kHz frequencies respectively.

Figs.4.2.8a-h show the hysteresis loops at 400 Hz frequency for ribbons annealed at different temperatures. The change in the magnetic properties of the material with the heat treatment is evident here. As the annealing temperature increases the loop becomes narrower, (i.e.decrease in coercivity), and taller, (i.e. increase in induction) and as a result, optimum properties are obtained at a particular annealing temperature. The hysteresis loops are plotted at 200 A/m ± 10 A/m applied magnetic field.

Fig.4.2.9 shows the hysteresis loops at different frequencies for as-cast $Co_{75}Si_{10}B_{15}$ ribbon. As the frequency increases the hysteresis loop becomes wider and as a result the coercivity and core loss increase. These hysteresis loops are plotted at 200 A/m ± 10 A/m applied magnetic field. Due to the instrumental limitations the hysteresis loop for 50 kHz frequency is plotted at 100 A/m ± 10 A/m.

At higher frequencies, the soft magnetic properties improve if the sample has 1 to 5 % crystalline precipitates [27] but in cobalt-based ribbons the hysteresis loop is shifted from the origin with the formation of crystallites. Fig 4.2.10 shows the shifted

hysteresis loop in a 472°C annealed sample at 1 Hz frequency. The full line hysteresis loop in Fig.4.2.10 is for the as-annealed ribbon. After chemically removing 25% of the mass of the ribbon by etching in dil. HNO_3, the dotted hysteresis loop is obtained. Both hysteresis loops were measured at the same applied magnetic field. The hysteresis loop obtained after chemically removing 25% of the ribbon surface showed a decrease in the shift.

Fig. 4.2.11 shows optical micrographs of the $Co_{75}Si_{10}B_{15}$ ribbon annealed for 60 mins. at 472°C and the same ribbon after chemically removing 25% of the total mass.

Fig.4.2.12 shows the increase in the shift with increase in annealing temperature at 1 Hz frequency.

Fig.4.2.13 and Fig.4.2.14 show TEM micrographs of samples annealed at 446°C and 458°C, together with an electron diffraction pattern from one of the α-Co crystals.

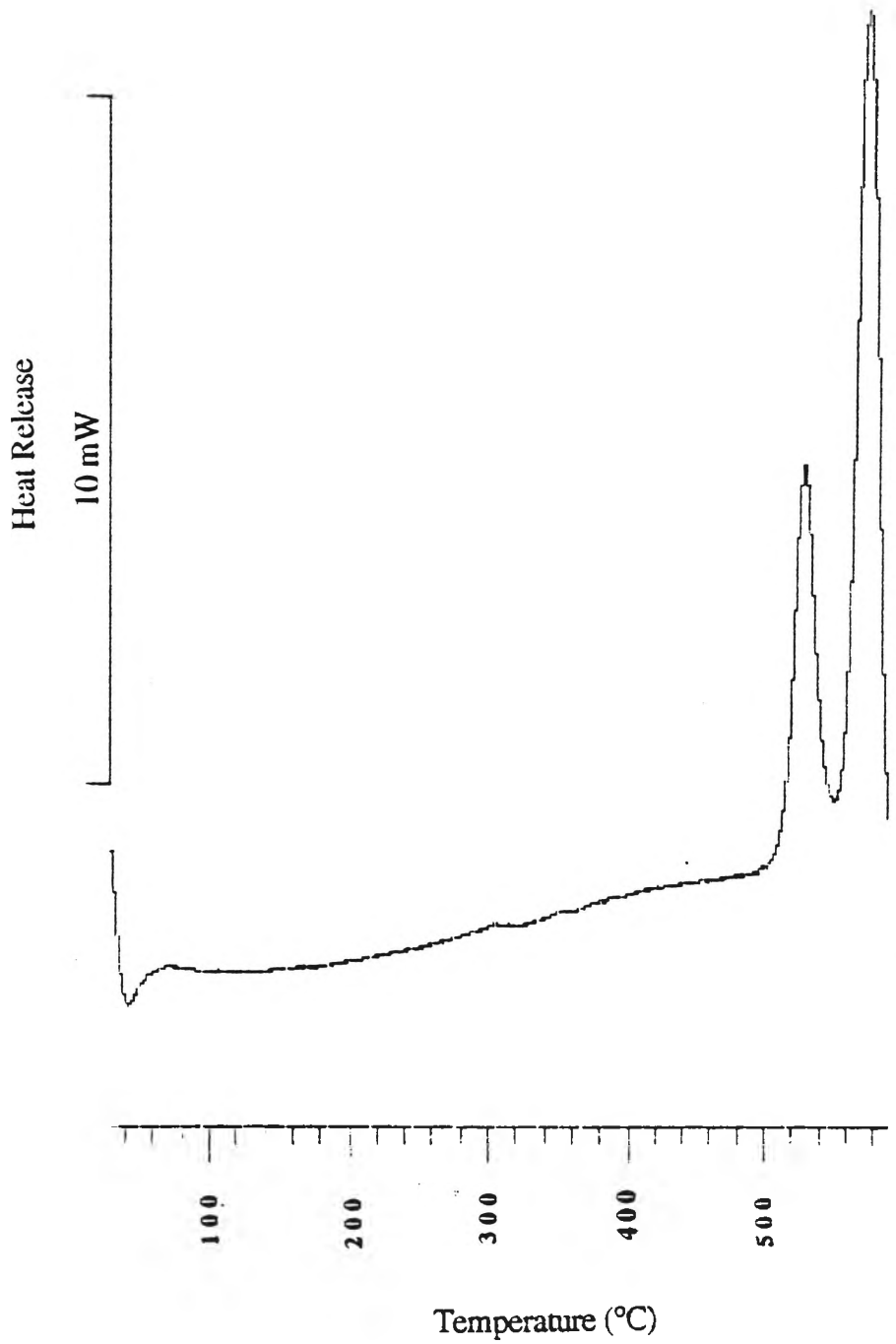

Fig.4.2.1 Dynamic DSC thermogram for $Co_{75}Si_{10}B_{15}$ (20°C/min.).

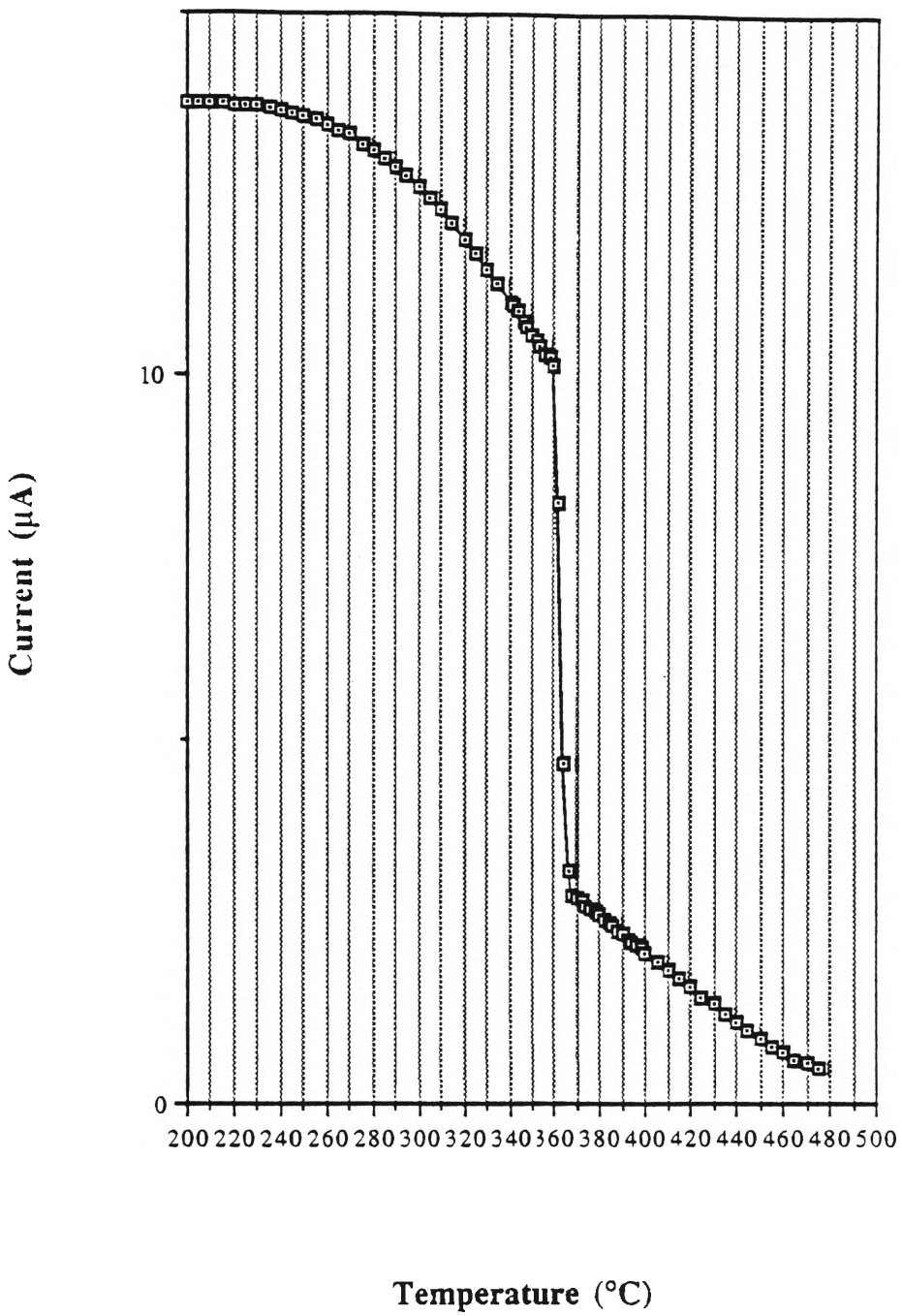

Fig.4.2.2 Measurement of Curie temperature for $Co_{75}Si_{10}B_{15}$ ribbon by the susceptibility method.

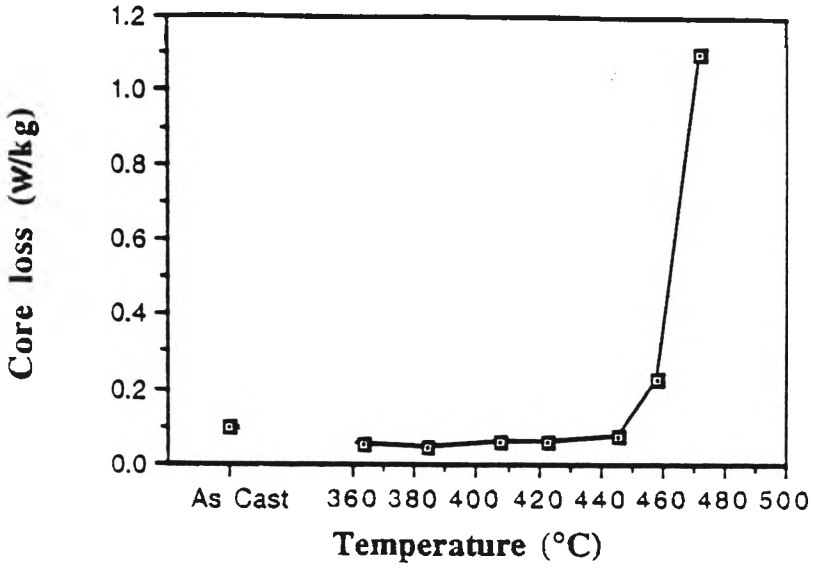

(a) at 50 Hz

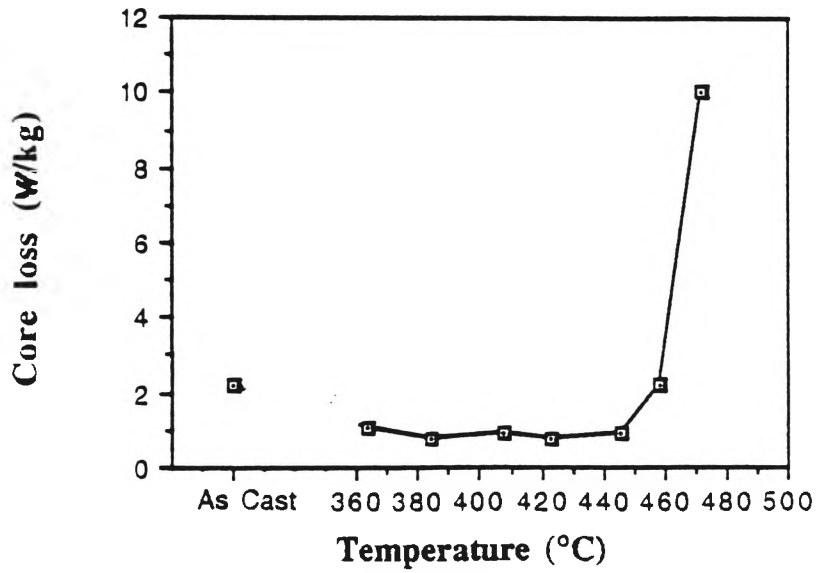

(b) at 400 Hz

Fig.4.2.3 (continue)

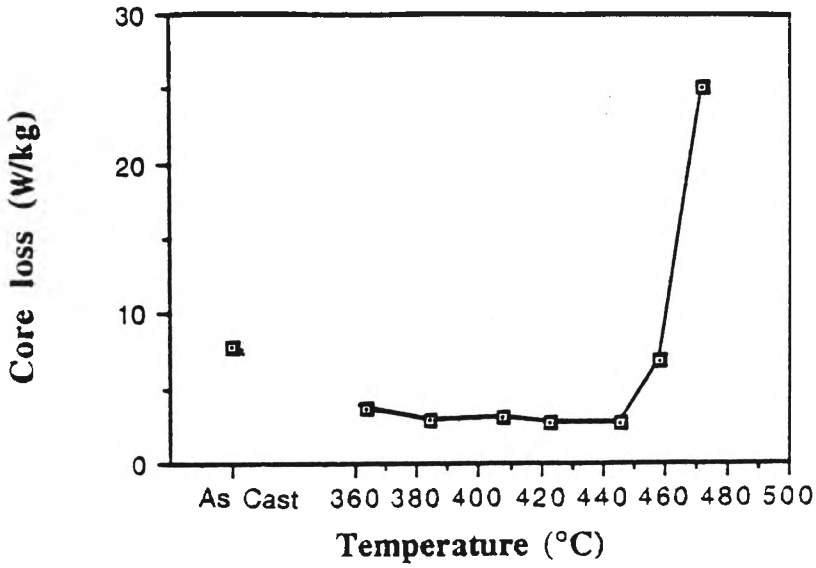

(c) at 1kHz

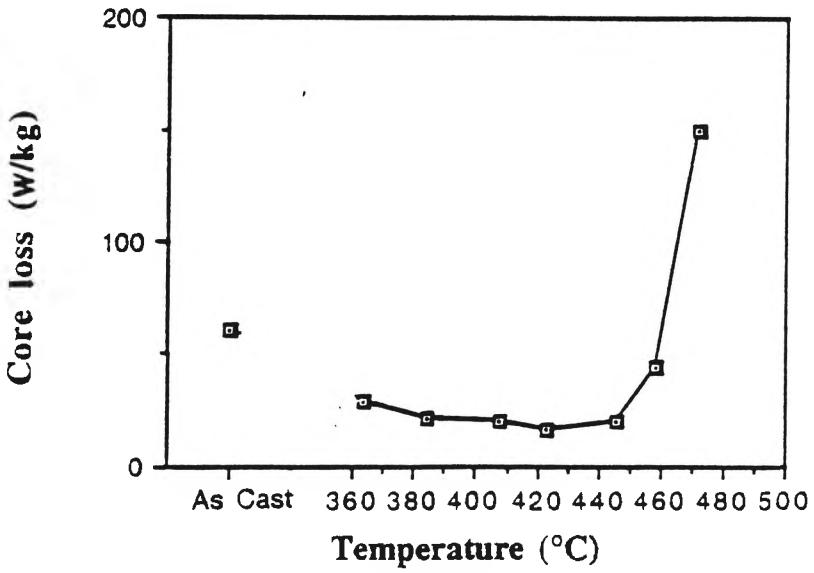

(d) at 5kHz

Fig.4.2.3 (continue)

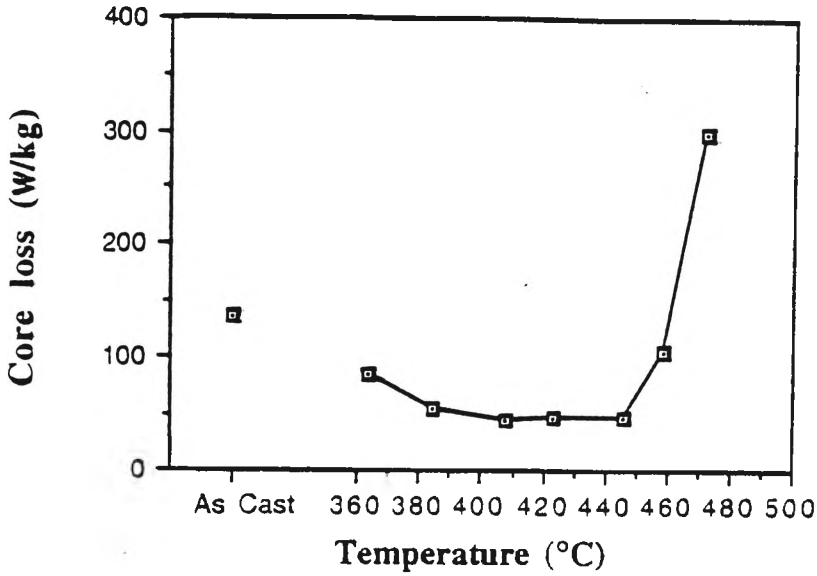

(e) at 10kHz

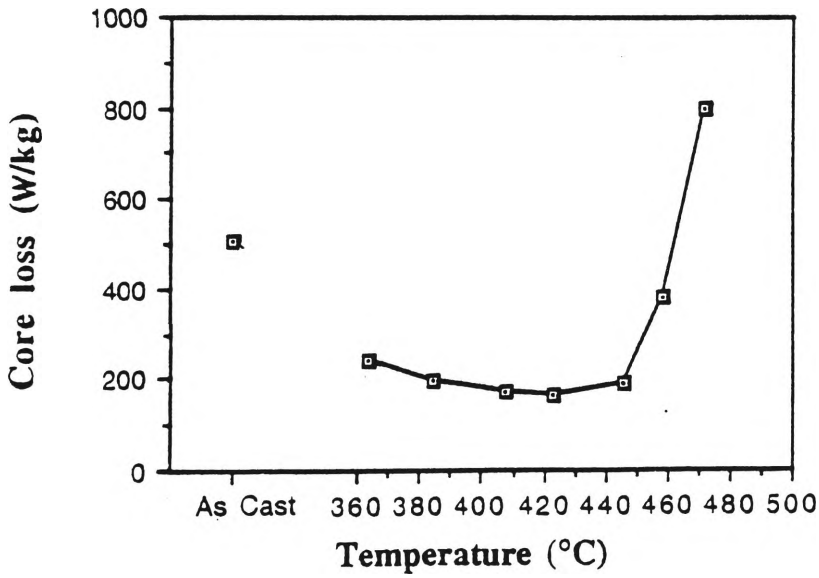

(f) at 25kHz

Fig.4.2.3 (continue)

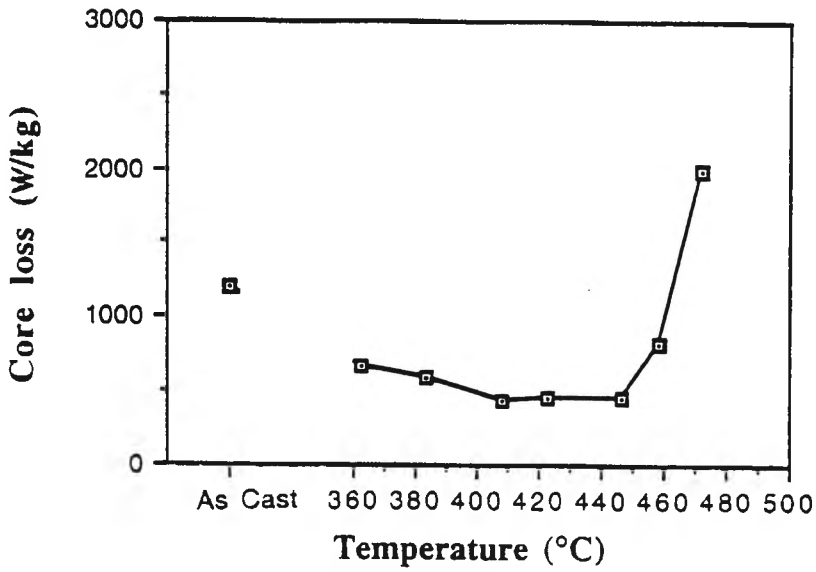

(g) at 50 kHz

Fig.4.2.3 Core loss (L_T) vs. temperature (T_a) at B = 0.6 Tesla for $Co_{75}Si_{10}B_{15}$.

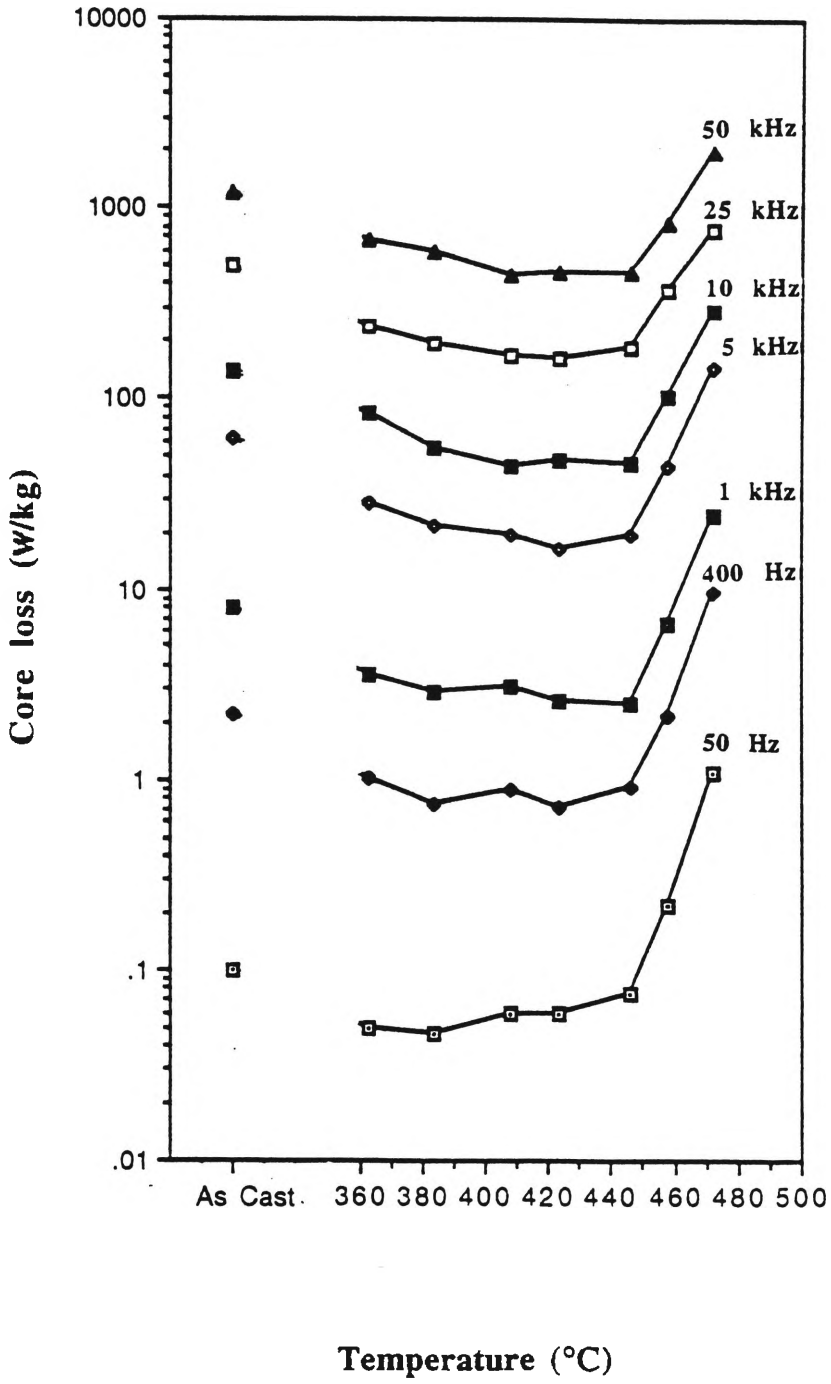

Fig.4.2.4 Core loss (L_T) vs. temperature (T_a) at B = 0.6 Tesla for $Co_{75}Si_{10}B_{15}$ at different frequencies.

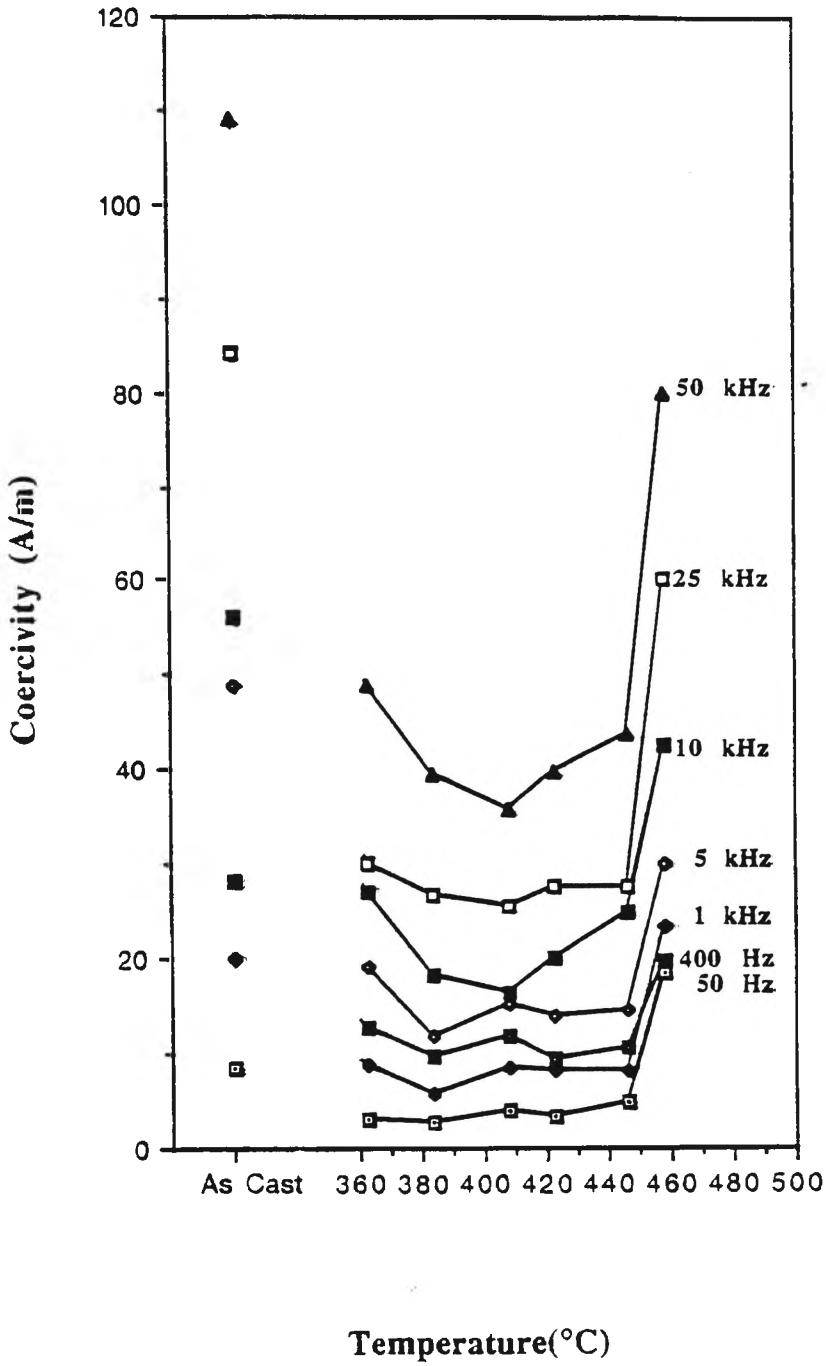

Fig.4.2.5 Coercivity (H_c) vs. temperature (T_a) at B = 0.6 Tesla for $Co_{75}Si_{10}B_{15}$ at different frequencies.

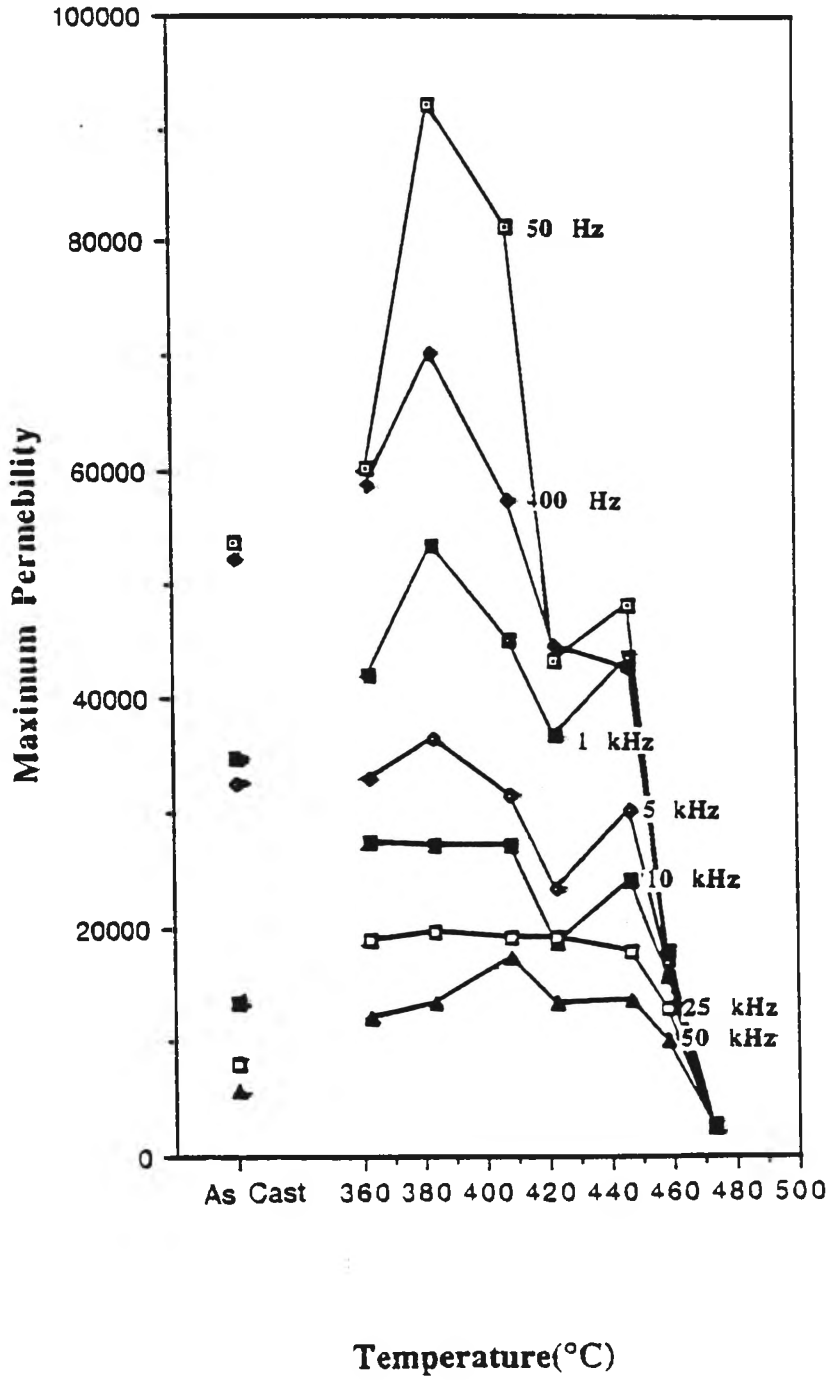

Fig.4.2.6 Maximum permeability (μ_{max}) vs. temperature (T_a) for $Co_{75}Si_{10}B_{15}$ at different frequencies.

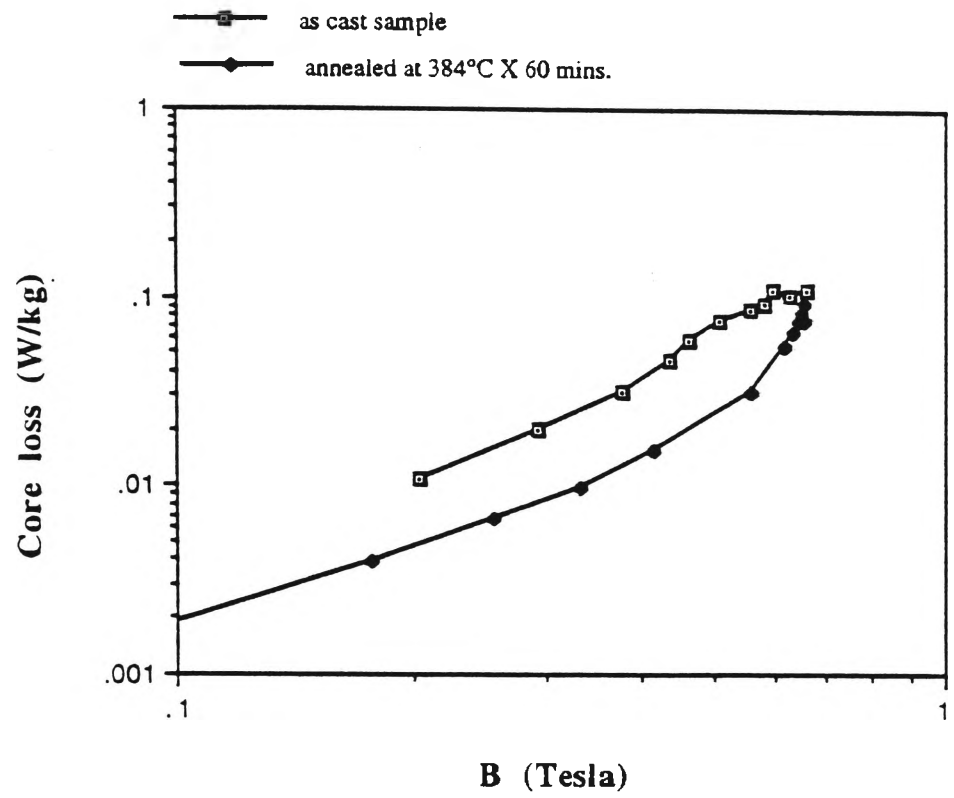

(a) at 50 Hz

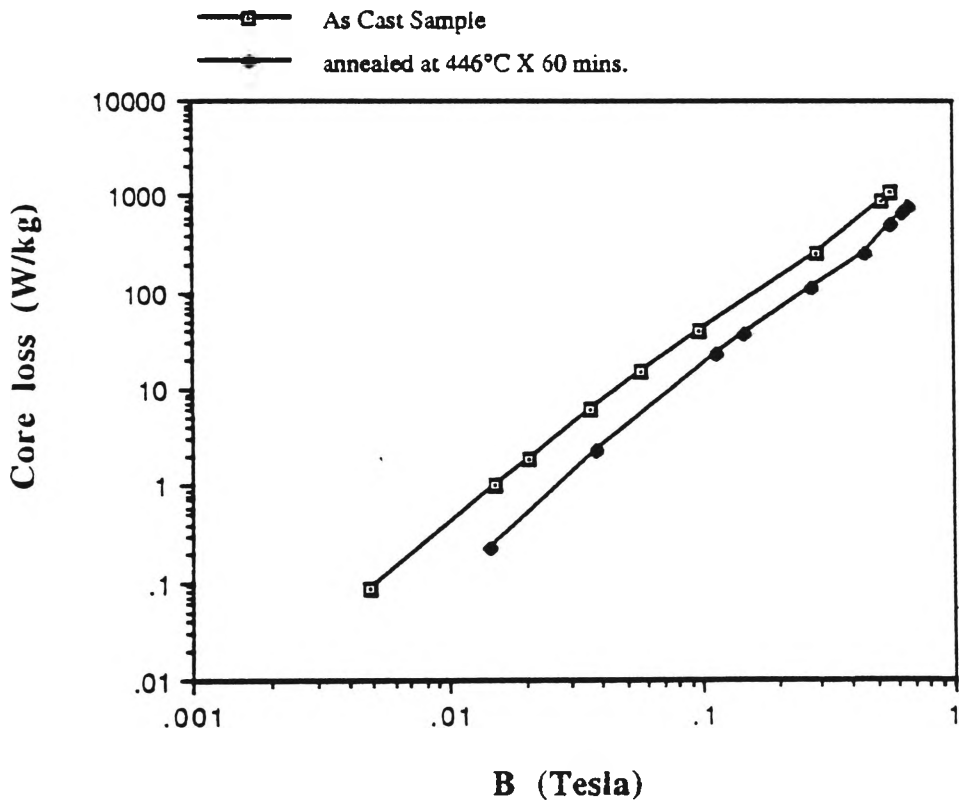

(b) at 50 kHz

Fig.4.2.7 Comparision of core loss at different inductions between as-cast $Co_{75}Si_{10}B_{15}$ ribbon and the ribbon annealed at optimum temperature..

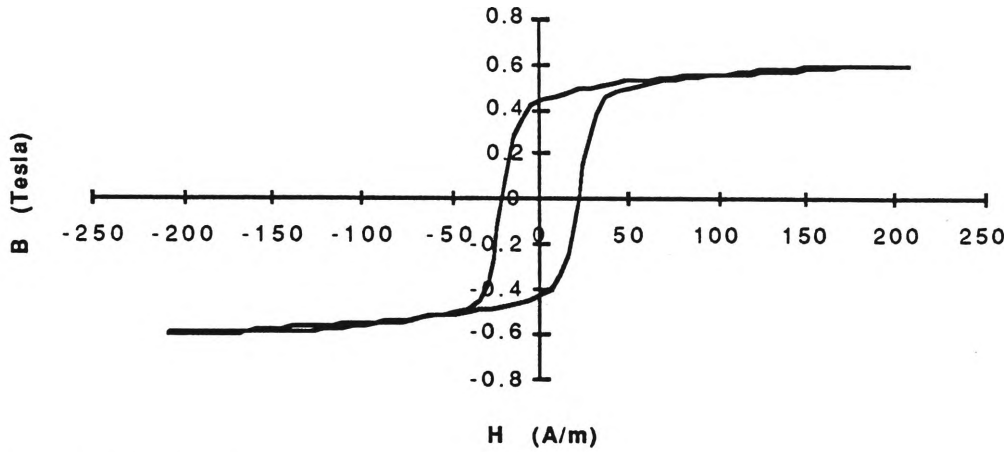

(a) For as-cast ribbon

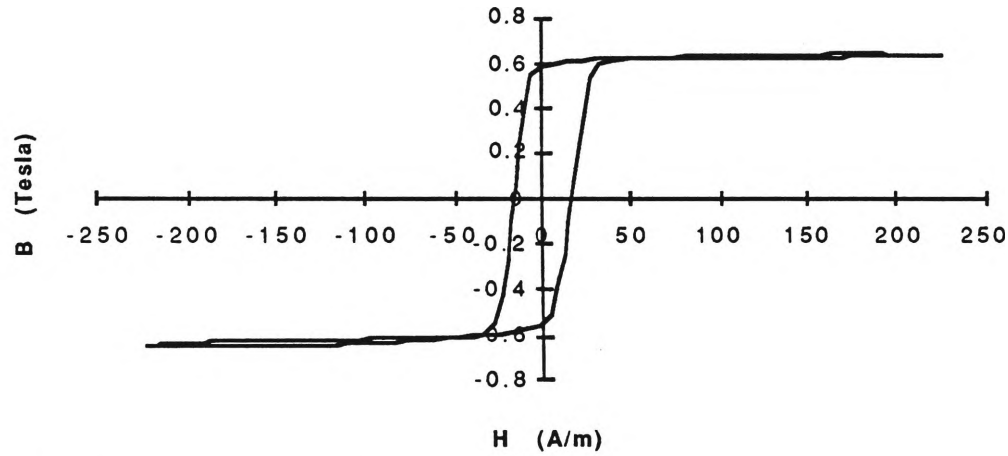

(b) For ribbon annealed at 363°C

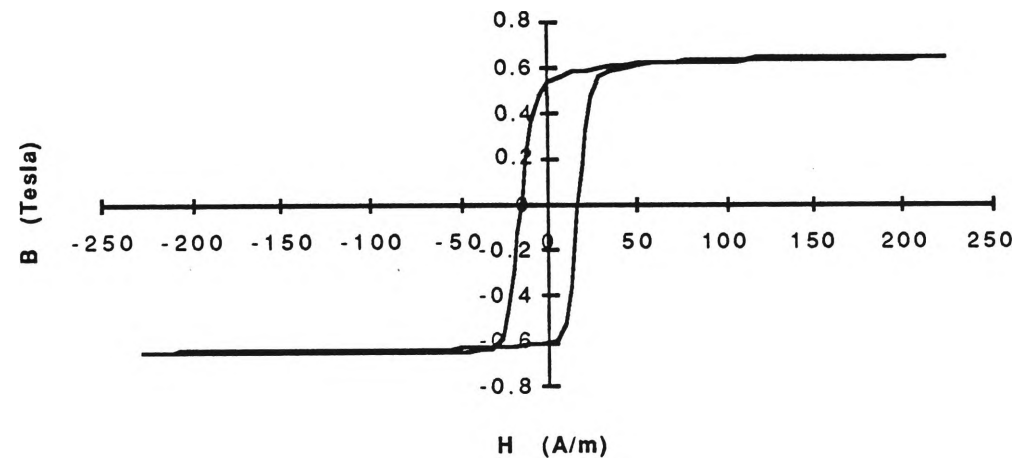

(c) For ribbon annealed at 384°C

Fig.4.2.8 (continue)

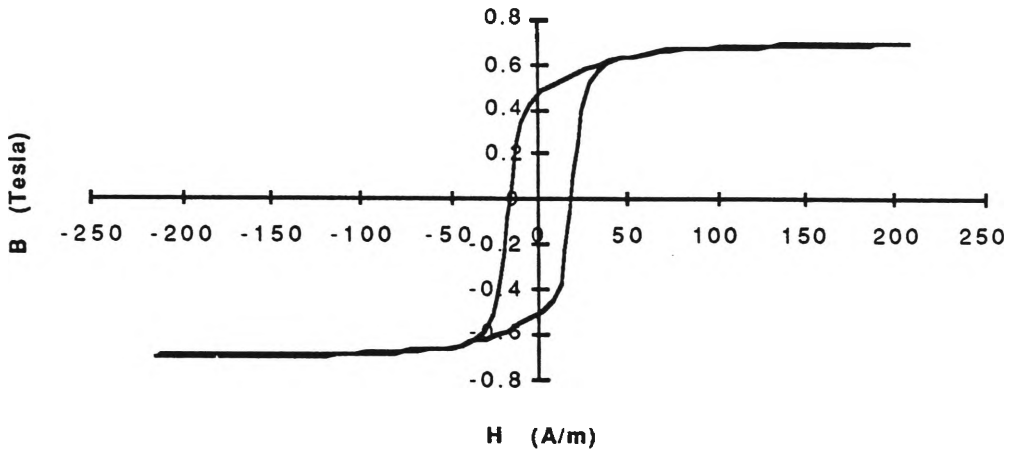

(d) For ribbon annealed at 408°C

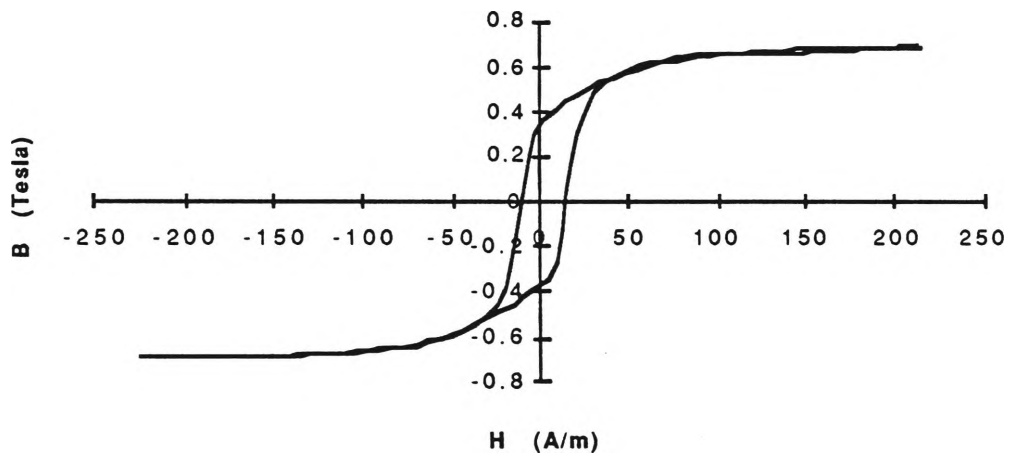

(e) For ribbon annealed at 423°C

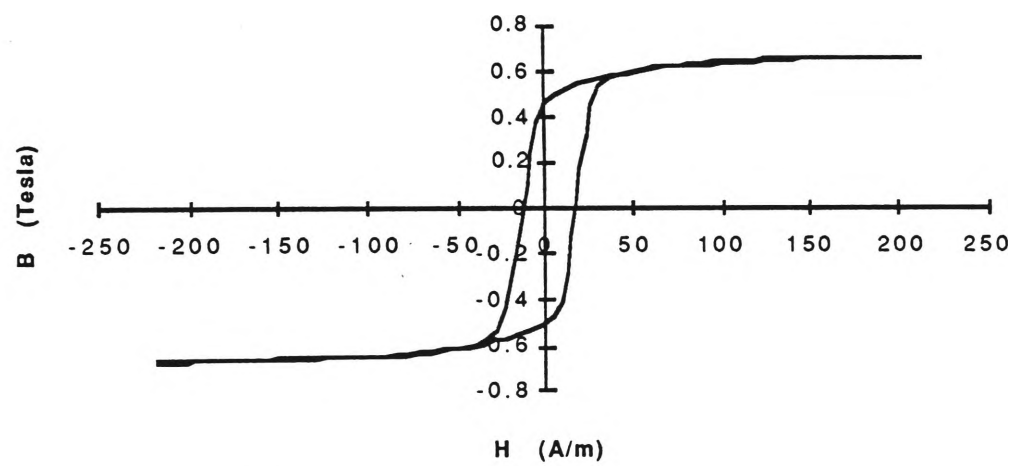

(f) For ribbon annealed at 446°C

Fig.4.2.8 (continue)

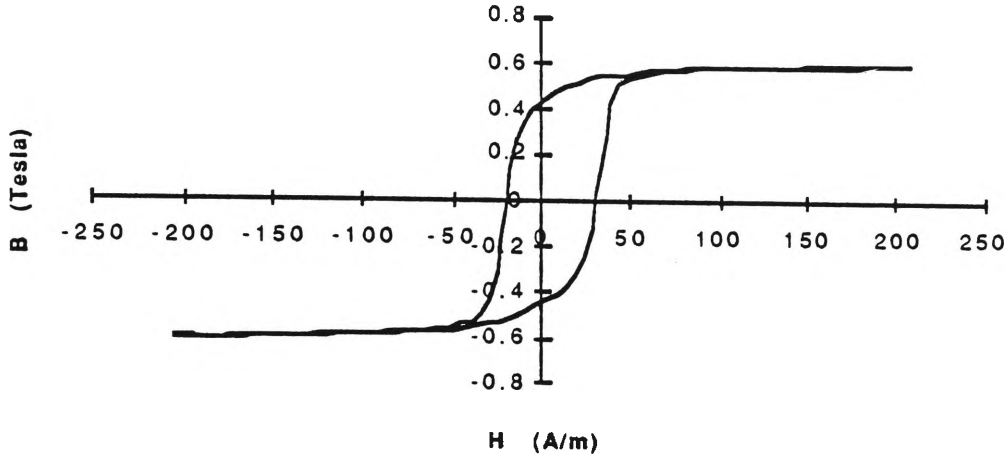

(g) For ribbon annealed at 458°C

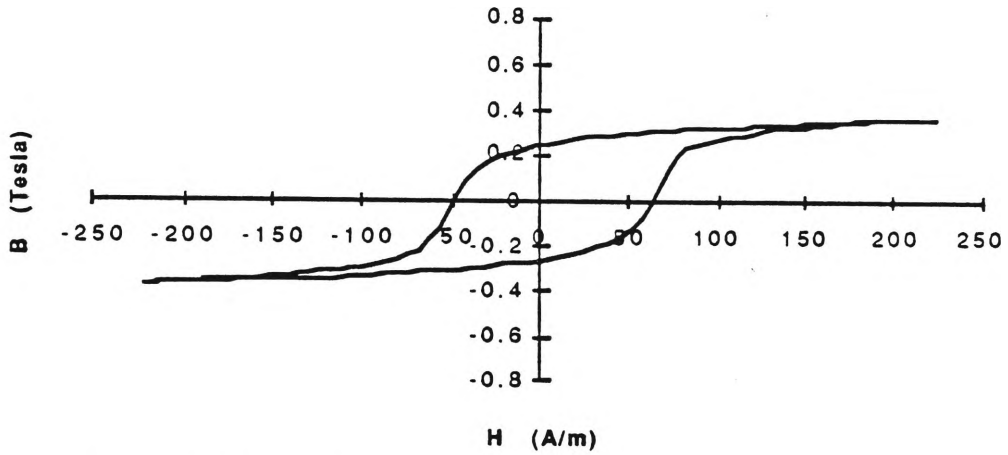

(h) For ribbon annealed at 472°C

Fig.4.2.8 Hysteresis loops for $Co_{75}Si_{10}B_{15}$ ribbon annealed at different temperatures. The loops were measured at 400 Hz with an applied magnetic field of 200 A/m ± 10 A/m.

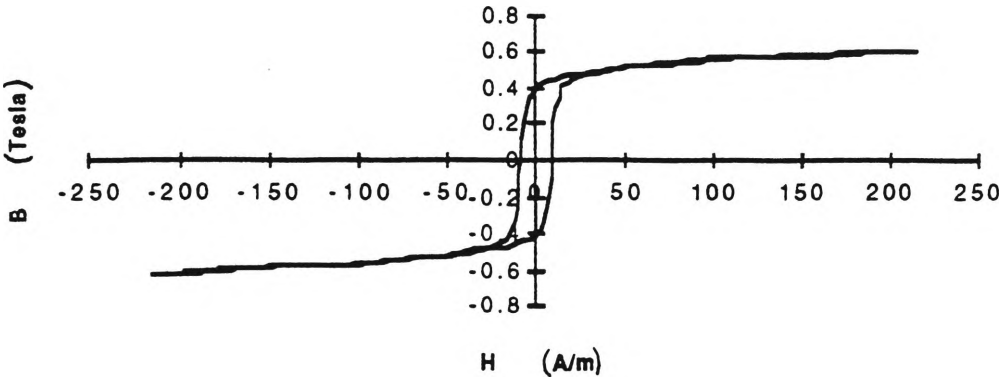

(a) at 50 Hz

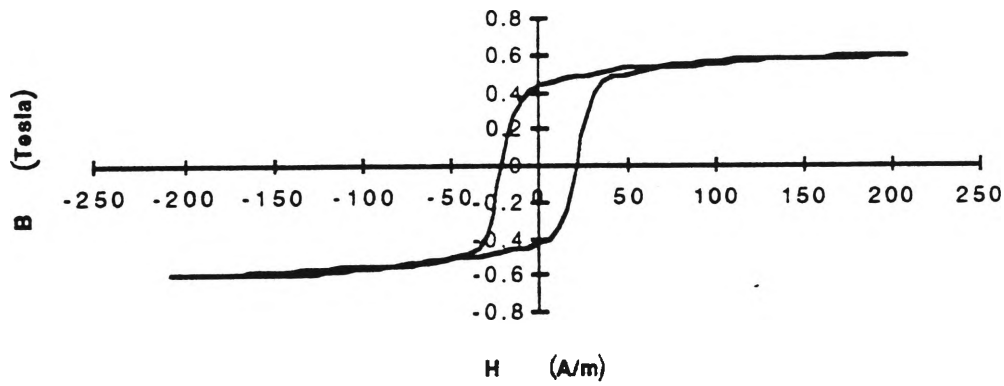

(b) at 400 Hz

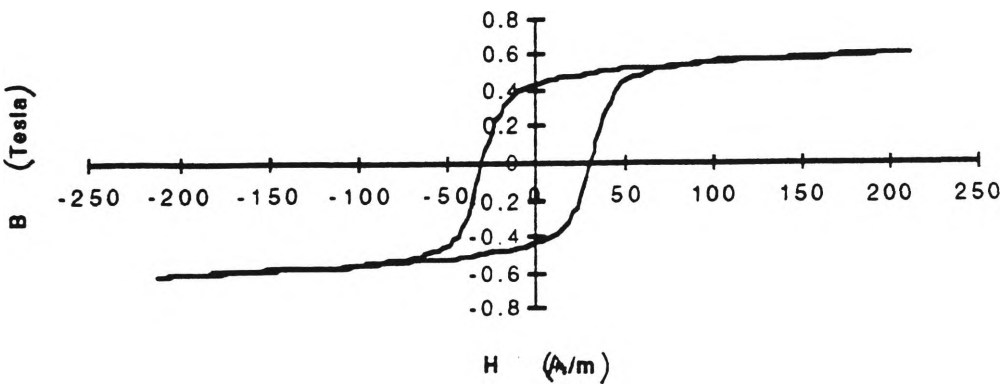

(c) at 1 kHz

Fig.4.2.9 (continue)

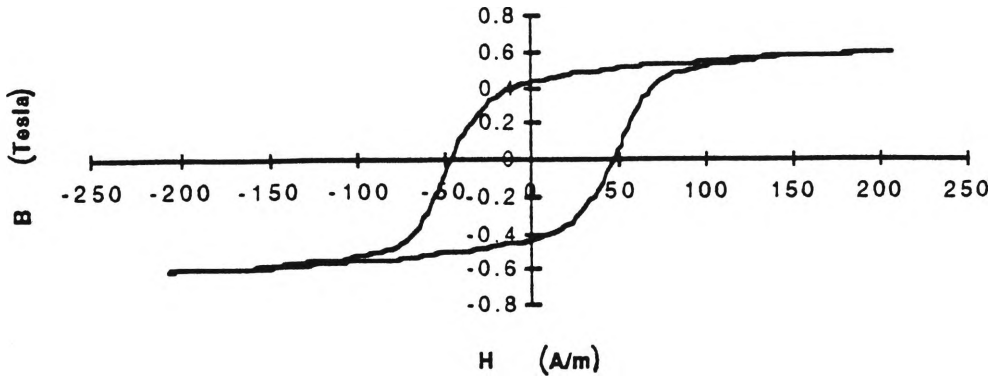

(d) at 5 kHz

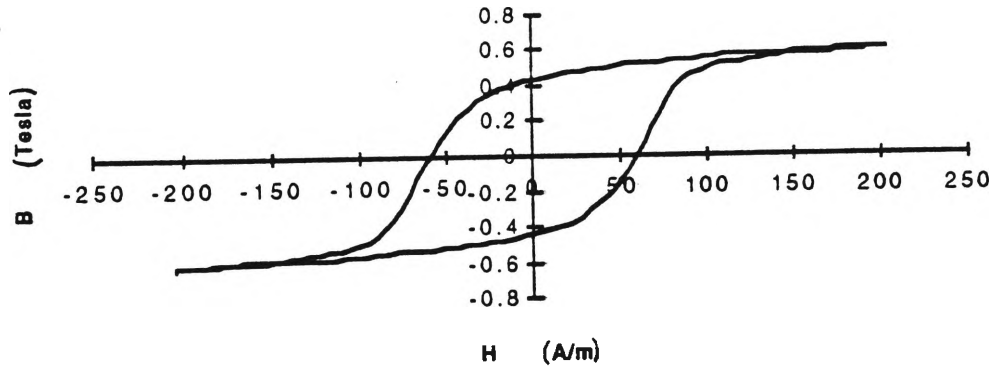

(e) at 10 kHz

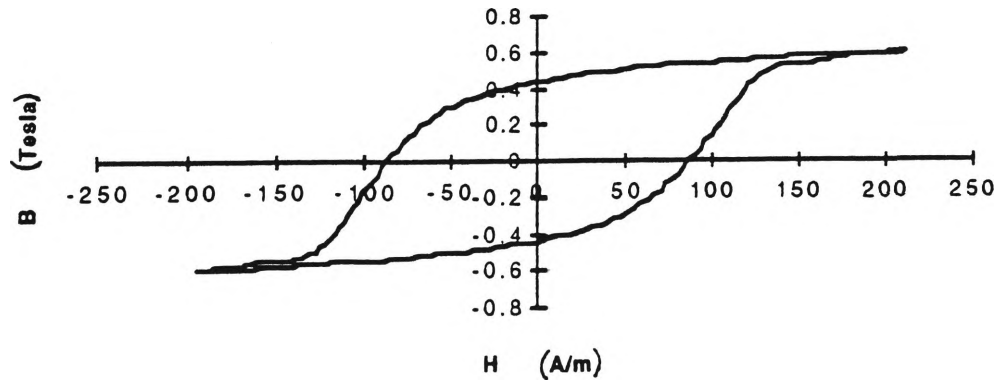

(f) at 25 kHz

Fig.4.2.9 (continue)

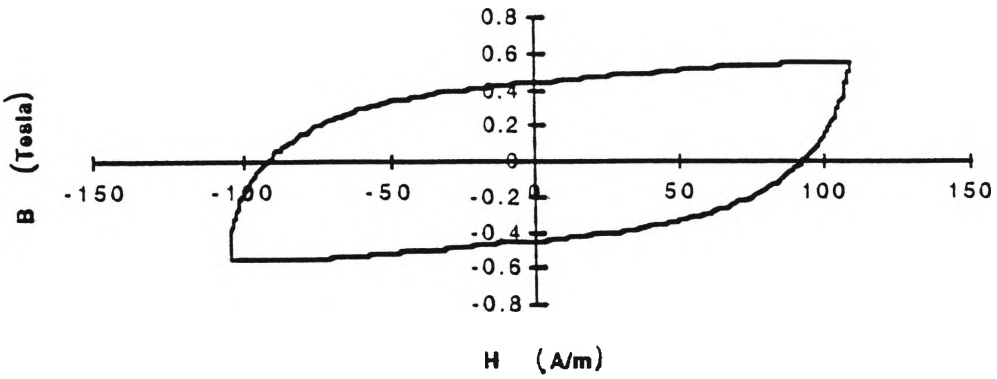

(g) at 50 kHz (an applied magnetic field was 100 A/m ± 10 A/m)

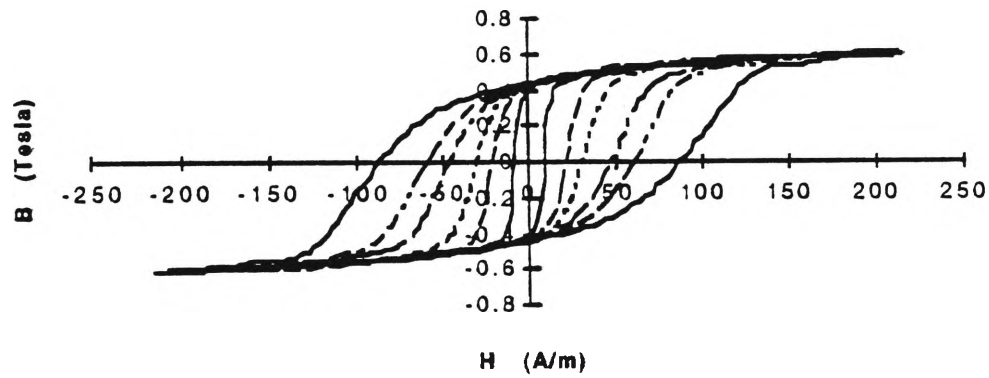

(h) superposition of figures a-f

Fig.4.2.9 The change in the shape of the hysteresis loop for the as-cast $Co_{75}Si_{10}B_{15}$ ribbon with frequency. The hysteresis loops were measured with an applied magnetic field of 200 A/m ± 10 A/m.

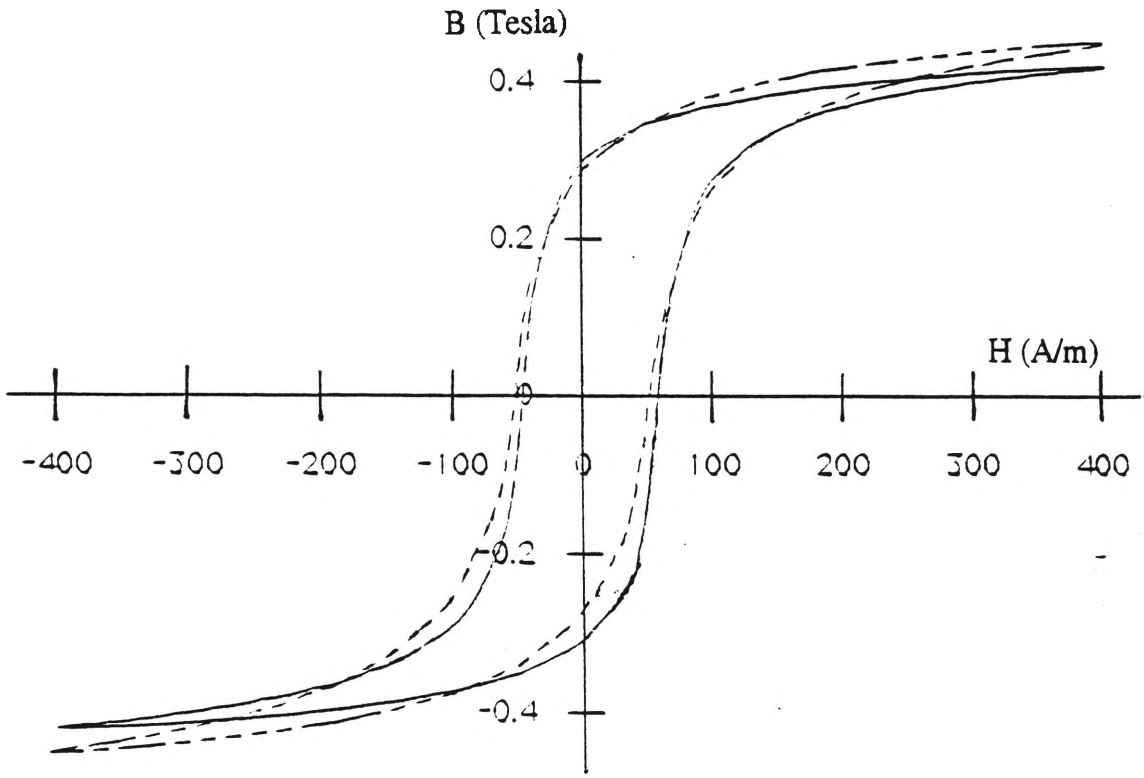

Fig.4.2.10 Hysteresis loop measured at 1 Hz frequency for $Co_{75}Si_{10}B_{15}$ ribbon annealed for 60 mins. at 472°C (full line). The as-annealed ribbon had ΔH_s = 6.4 A/m and B = 0.42 Tesla. The dotted hysteresis loop was measured after chemically removing 25 % of the total mass of the sample. This loop had ΔH_s = 3.6 A/m and B = 0.45 Tesla. Both the loops were measured at 400 A/m ± 5 A/m.

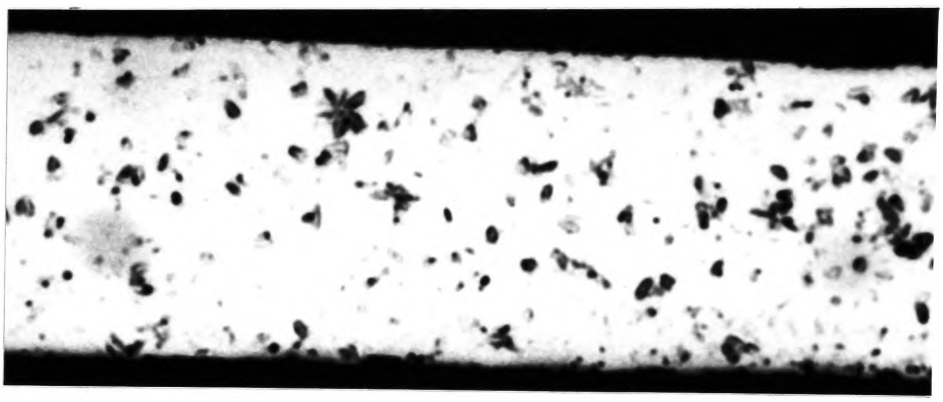

(a) as annealed ribbon

(b) after chemically removing 25 % of the total mass of the ribbon

Fig.4.2.11 Optical micrographs of cross-section for $Co_{75}Si_{10}B_{15}$ ribbon annealed for 60 mins. at 472°C (X 500).

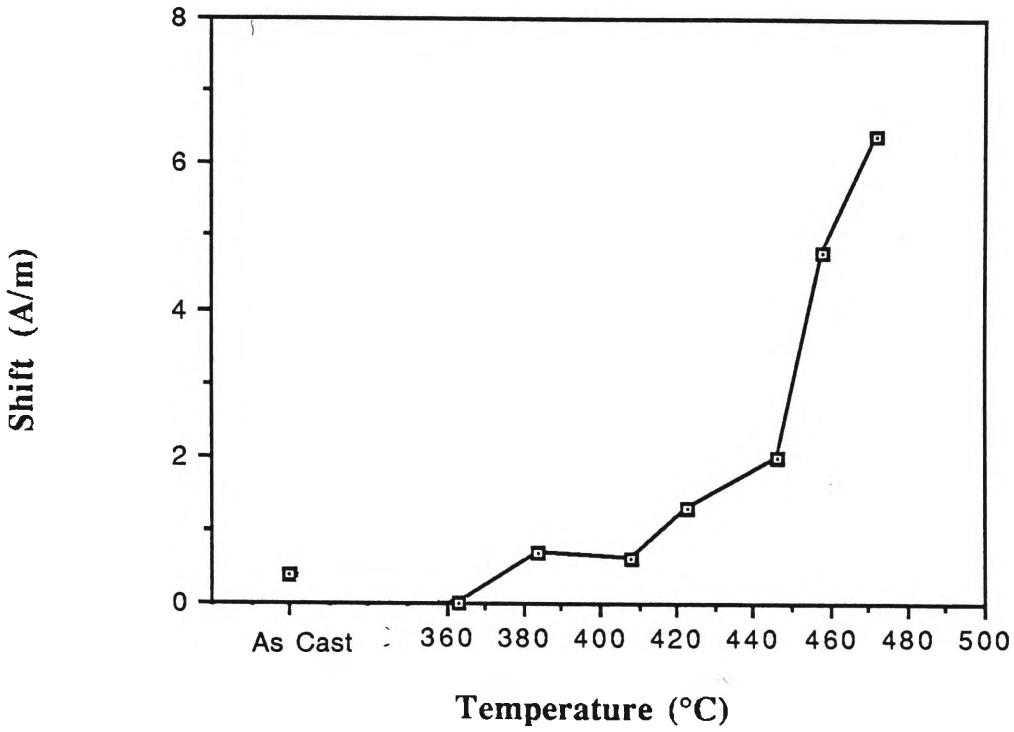

Fig.4.2.12 Shift in the hysteresis loop measured at 1 Hz frequency in $Co_{75}Si_{10}B_{15}$ alloy. The applied magnetic field was 250 A/m.

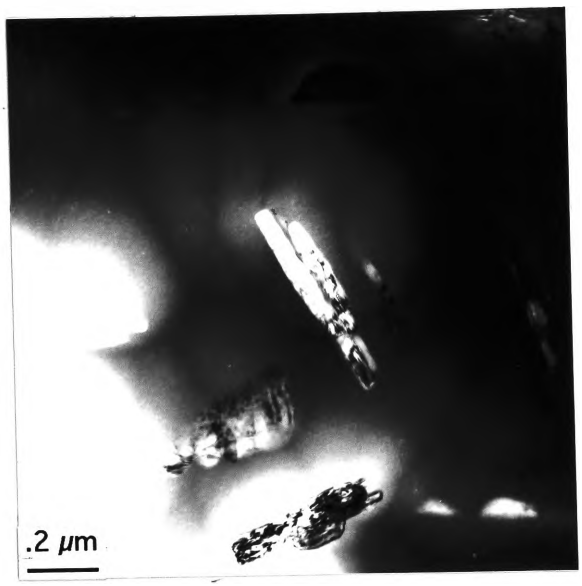

(a) ribbon annealed for 60 mins. at 446°C

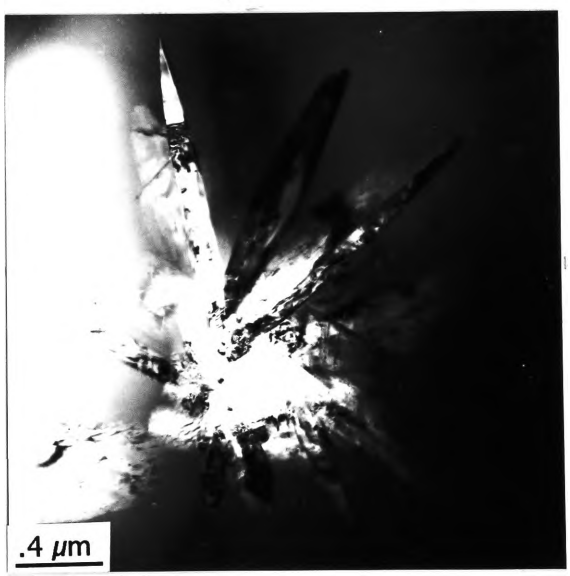

(b) ribbon annealed for 60 mins. at 458°C

Fig.4.2.13 TEM micrograph for $Co_{75}Si_{10}B_{15}$ ribbon annealed for 60 mins. at 446°C and 458°C.

(a)

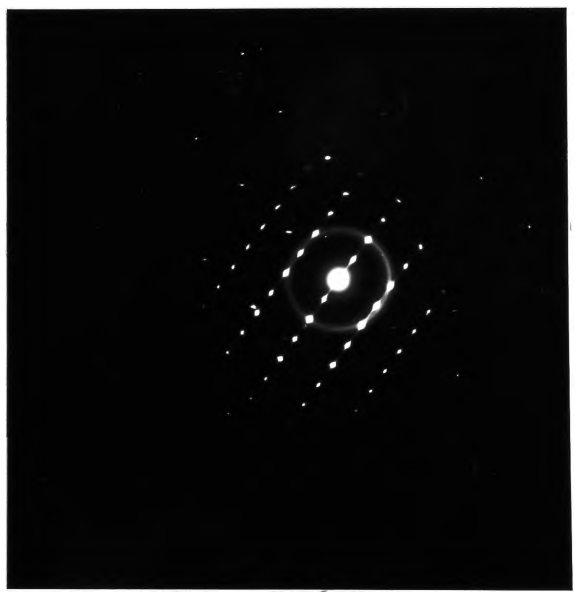

(b)

Fig.4.2.14 Partially-crystallised $Co_{75}Si_{10}B_{15}$ ribbon annealed for 60 mins. at 458°C.

(a) BF image of the ribbon

(b) EDP from area shown in (a).

4.3 Magnetic Properties of $Fe_{60}Ni_{20}Si_{10}B_{10}$ ribbon

The crystallisation process in the $Fe_{60}Ni_{20}Si_{10}B_{10}$ ribbon was measured by dynamic DSC at a rate of 20°C/min. The DSC thermogram shown in Fig.4.3.1 showed two peaks, the first peak at 465°C and second peak at 508°C. The DSC thermogram also showed a small endothermic peak at 410°C as shown in Fig.4.3.2. The Curie temperature as measured by the susceptibility method is shown in Fig.4.3.3. The temperature measured by the susceptibility method confirms the endothermic peak temperature corresponding to Curie temperature in the DSC thermogram, (410°C).

Figs.4.3.4a-g show the core loss vs. annealing temperature relationship at 0.9 Tesla induction for different frequencies. As the annealing temperature increases, the core loss decreases up to a certain temperature and then starts to increase as the properties of the sample deteriorate. In this graph, the as-cast ribbon's data at 25 kHz and 50 kHz frequencies have been estimated because to reach 0.9 Tesla induction at higher frequency, a very high applied magnetic field is required. The estimated values are taken from log-log graphs of core loss vs. induction. Due to the limitations of the instrument, these higher magnetic fields cannot be achieved. Due to the same limitation, core loss data for the 420°C annealed sample are estimated for 5 kHz, 10 kHz and 25 kHz frequencies. The change in the core loss with annealing temperature at different frequencies is also shown in Fig.4.3.5.

The change in the coercivity with annealing temperature at 0.9 Tesla induction is shown in Fig.4.3.6. As with core loss, the coercivity changes with annealing temperature and is a minimum at particular temperature. As the material loses its soft magnetic properties, the coercivity increases slowly and when the sample crystallises the coercivity increases sharply.

Fig.4.3.7 shows the plot of maximum permeability vs. annealing temperature for different frequencies. The hysteresis loop of the ribbons annealed at 420°C does not reach the saturation level for 25 kHz and 50 kHz frequencies because of the instrument limitation. Hence the μ_{max} corresponding to 420°C are not plotted.

The core losses at different inductions and at all frequencies for a ribbon annealed at 322°C are shown in Fig.4.3.8.

Figs.4.3.9a-h show hysteresis loops at a frequency of 400 Hz for samples annealed at different temperatures for 60 mins. The change in the properties of the material with heat treatment is evident here. As the annealing temperature increases, the loop becomes narrower and squarer; as a result core loss and coercivity are minimised at a particular annealing temperature.

Figs.4.3.10a-f show the hysteresis loops at different frequencies for the $Fe_{60}Ni_{20}Si_{10}B_{10}$ as-cast sample. As the frequency increases, the hysteresis loop becomes wider and as a result the core loss and coercivity increase. These hysteresis loops are plotted at 200 A/m ± 10 A/m applied magnetic field.

Figs.4.3.11a-g show the change in the shape of the hysteresis loop with the increase of annealing temperature at 1 Hz frequency.

An optical micrograph of an $Fe_{60}Ni_{20}Si_{10}B_{10}$ sample annealed at 420°C is shown in Fig.4.3.12.

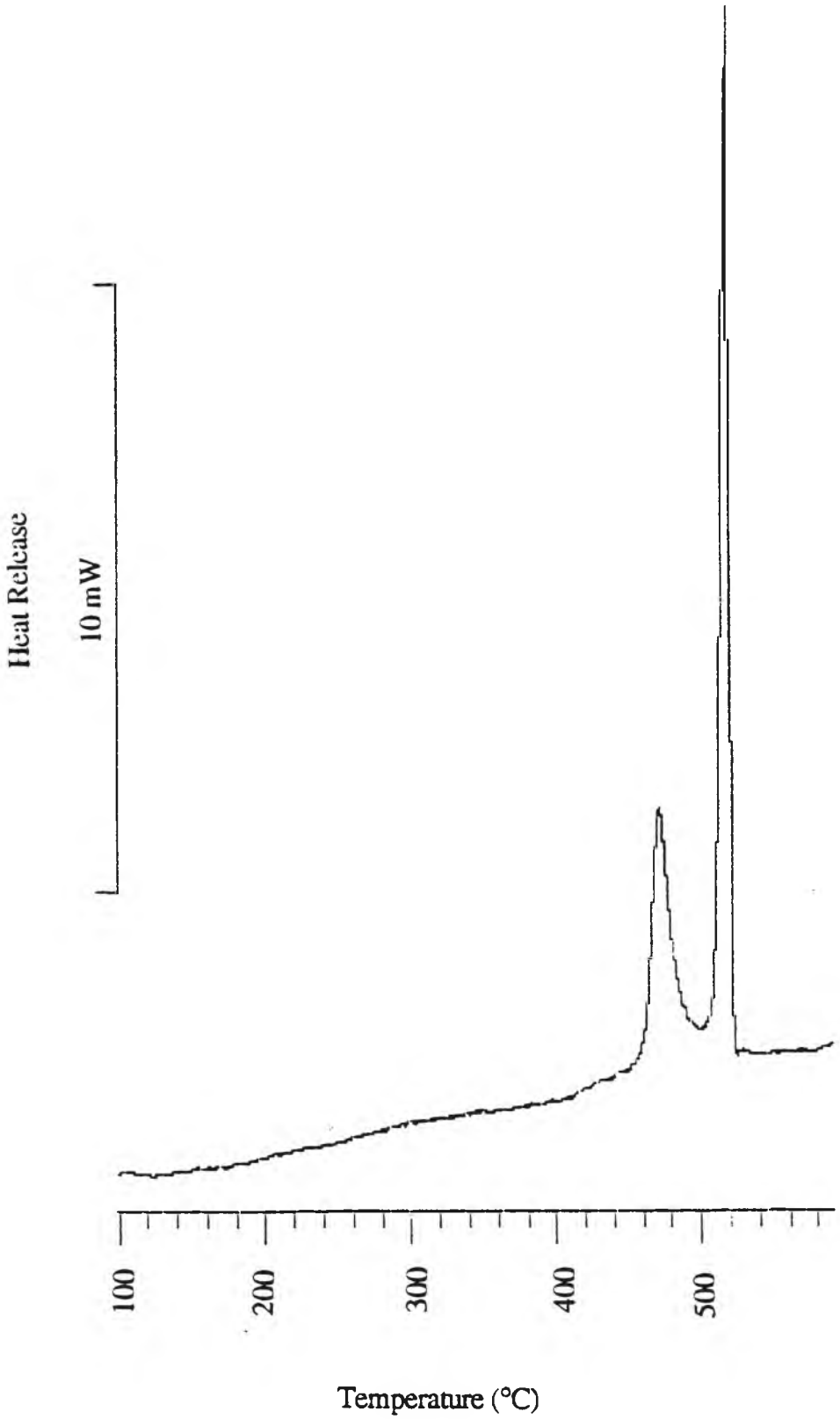

Fig.4.3.1 Dynamic DSC thermogram for $Fe_{60}Ni_{20}Si_{10}B_{10}$ (20°C/min.).

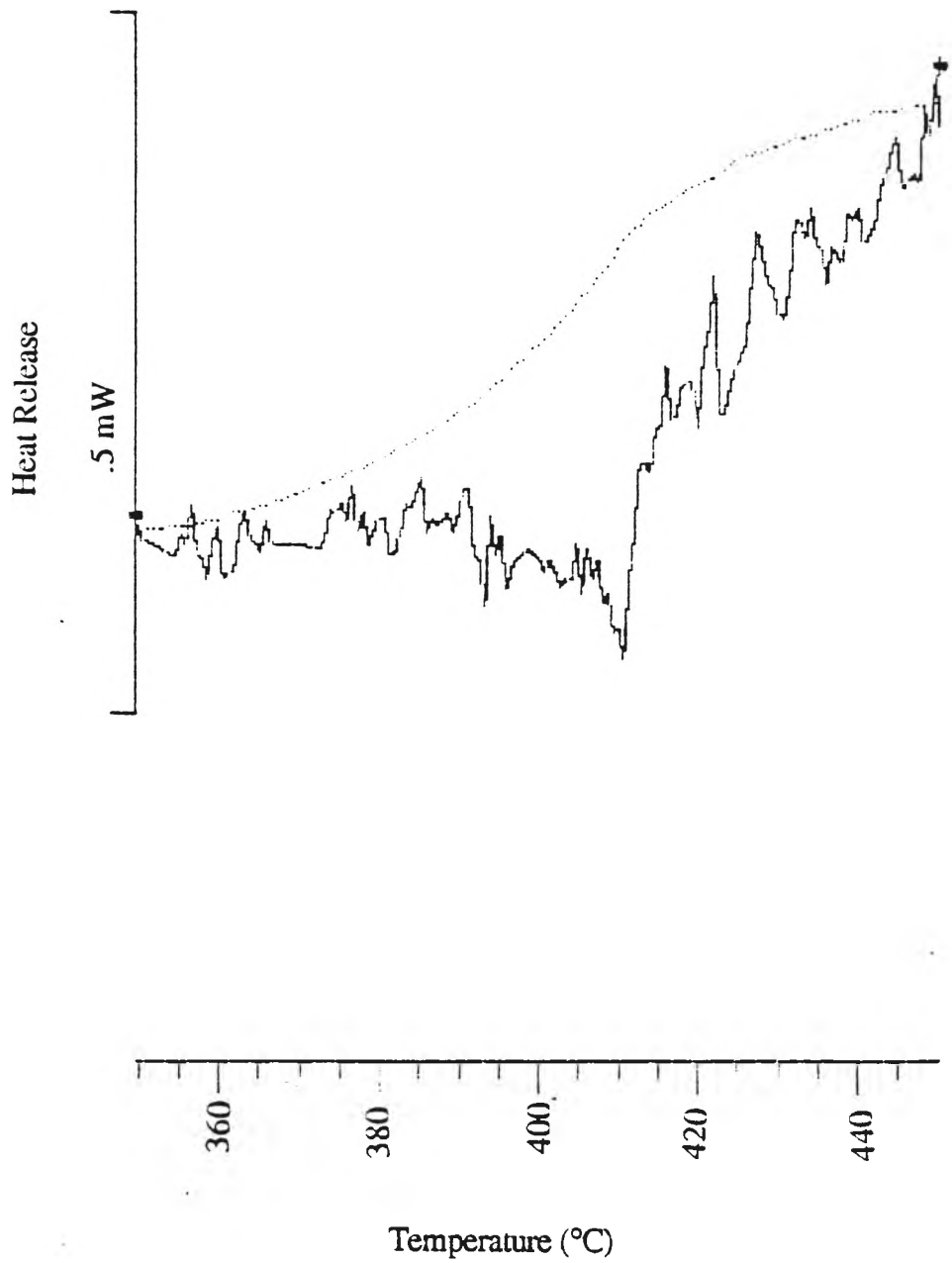

Fig.4.3.2 Curie temperature for $Fe_{60}Ni_{20}Si_{10}B_{10}$ measured by DSC.

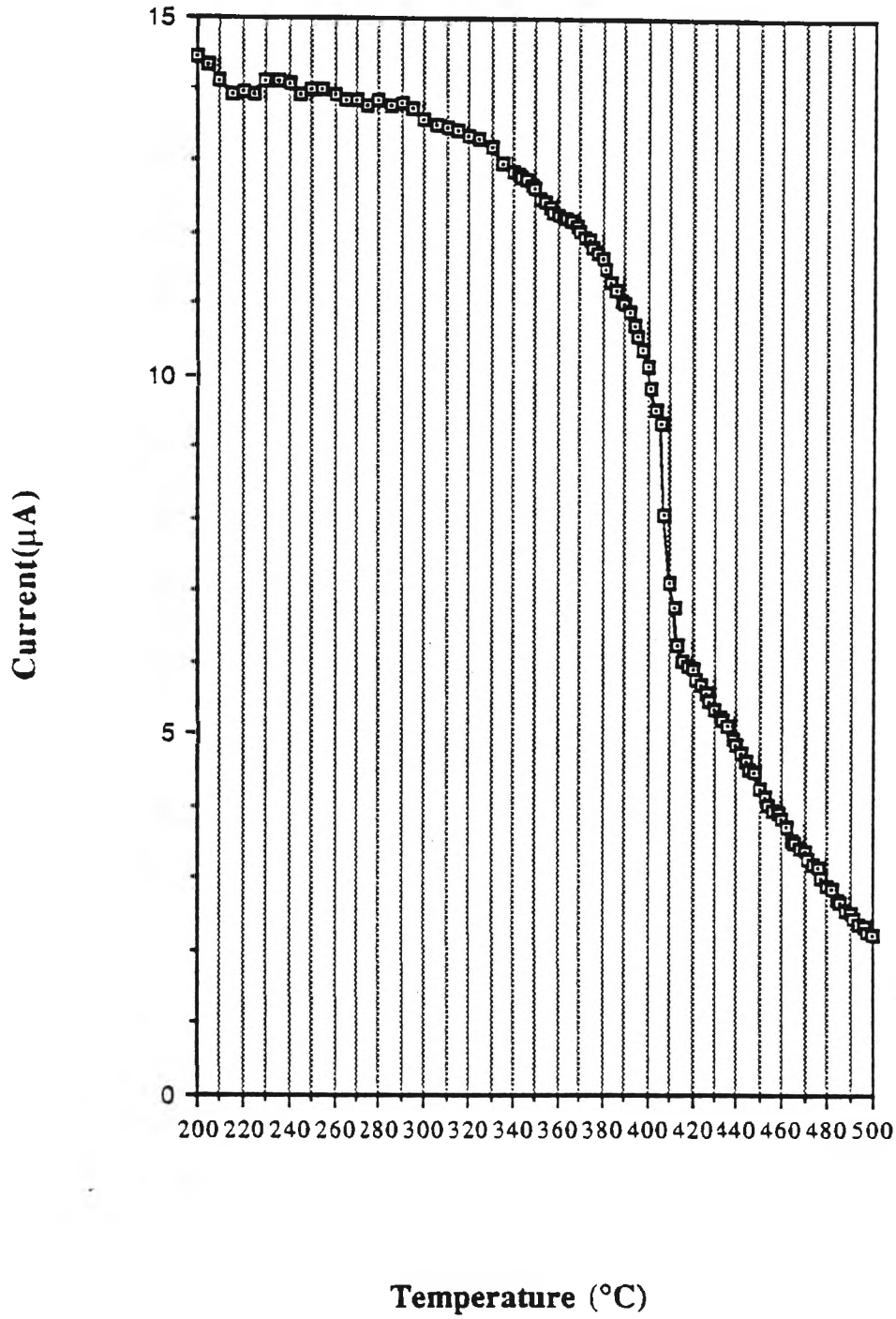

Fig.4.3.3 Curie temperature for $Fe_{60}Ni_{20}Si_{10}B_{10}$ measured by susceptibility method.

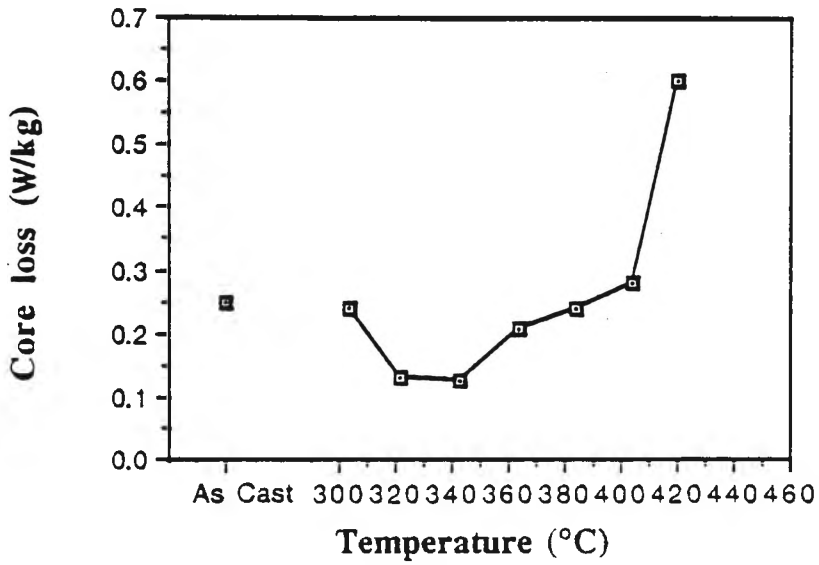

(a) at 50 Hz

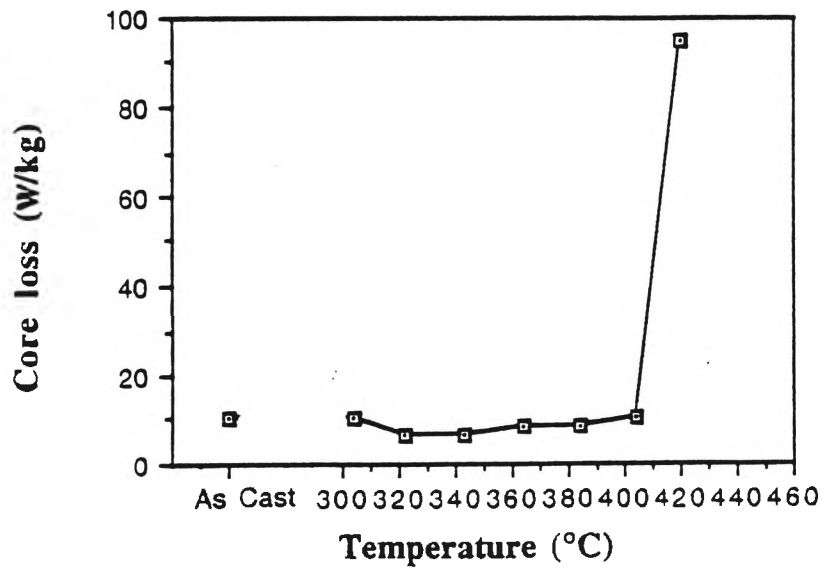

(b) at 400 Hz

Fig.4.3.4 (continue)

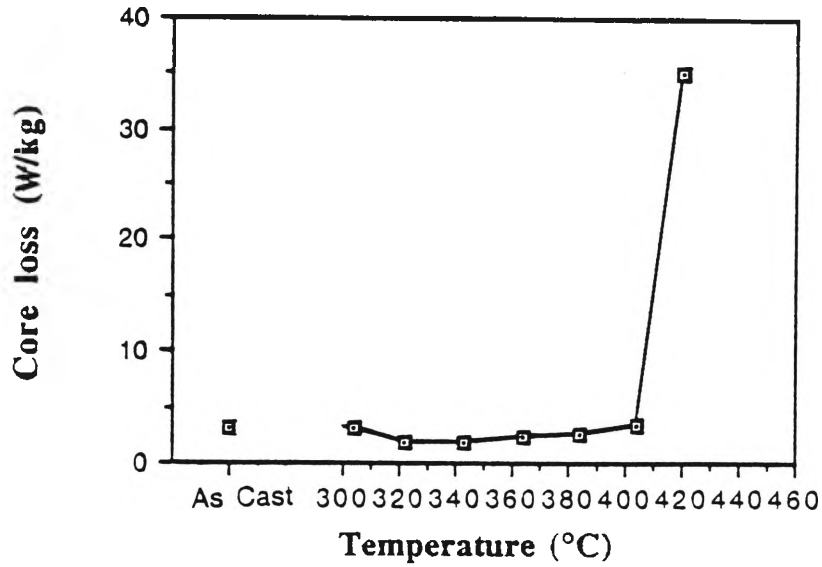

(c) at 1kHz

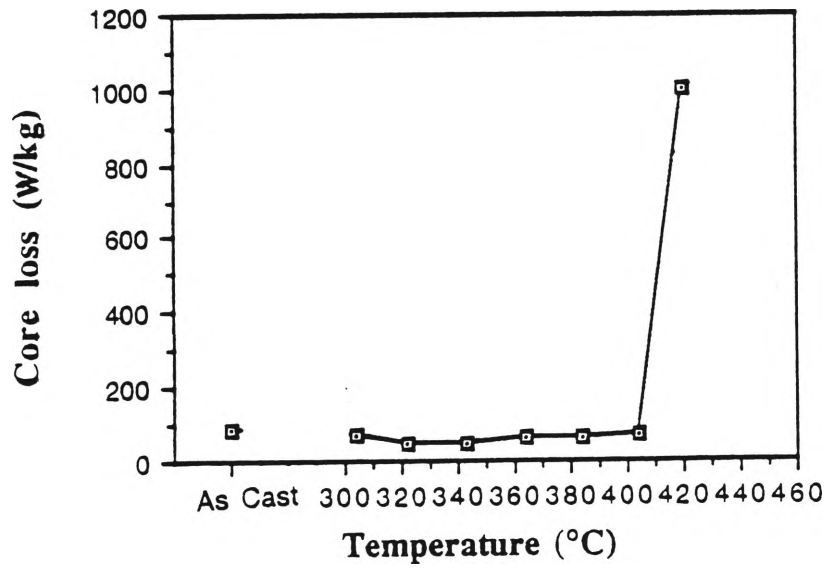

(d) at 5kHz

Fig.4.3.4 (continue)

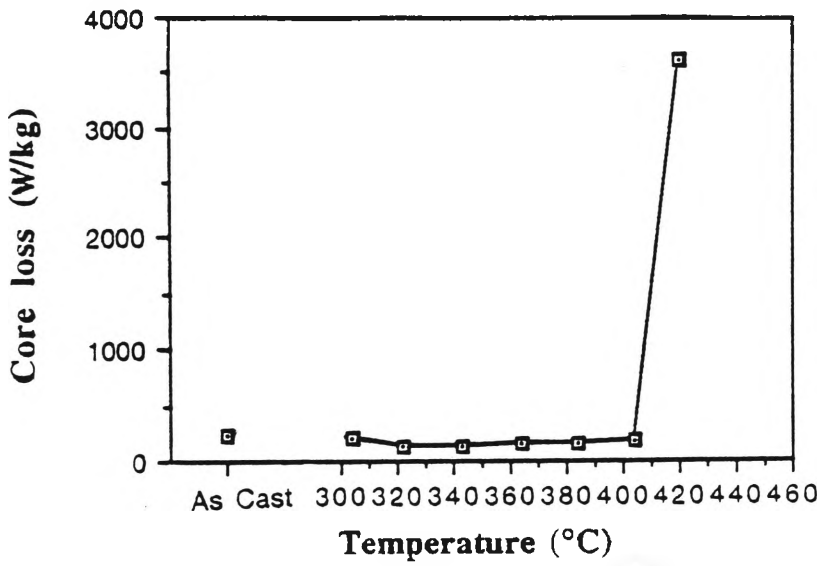

(e) at 10kHz

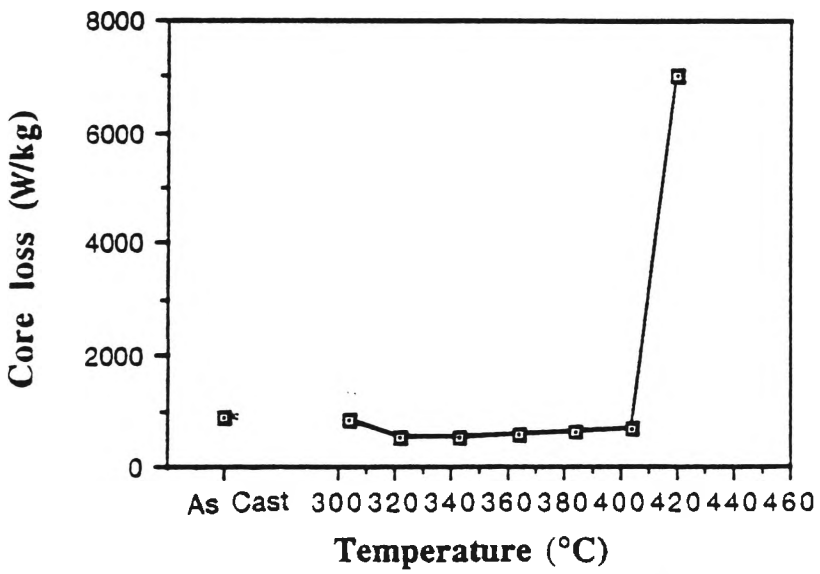

(f) at 25kHz

Fig.4.3.4 (continue)

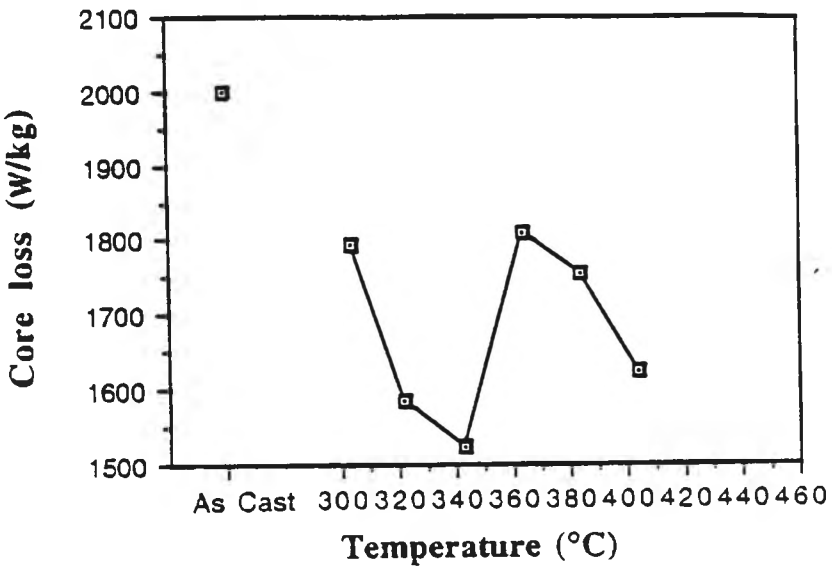

(g) at 50 kHz

Fig.4.3.4 Core loss (L_T) vs. temperature (T_a) at B = 0.9 Tesla for $Fe_{60}Ni_{20}Si_{10}B_{10}$.

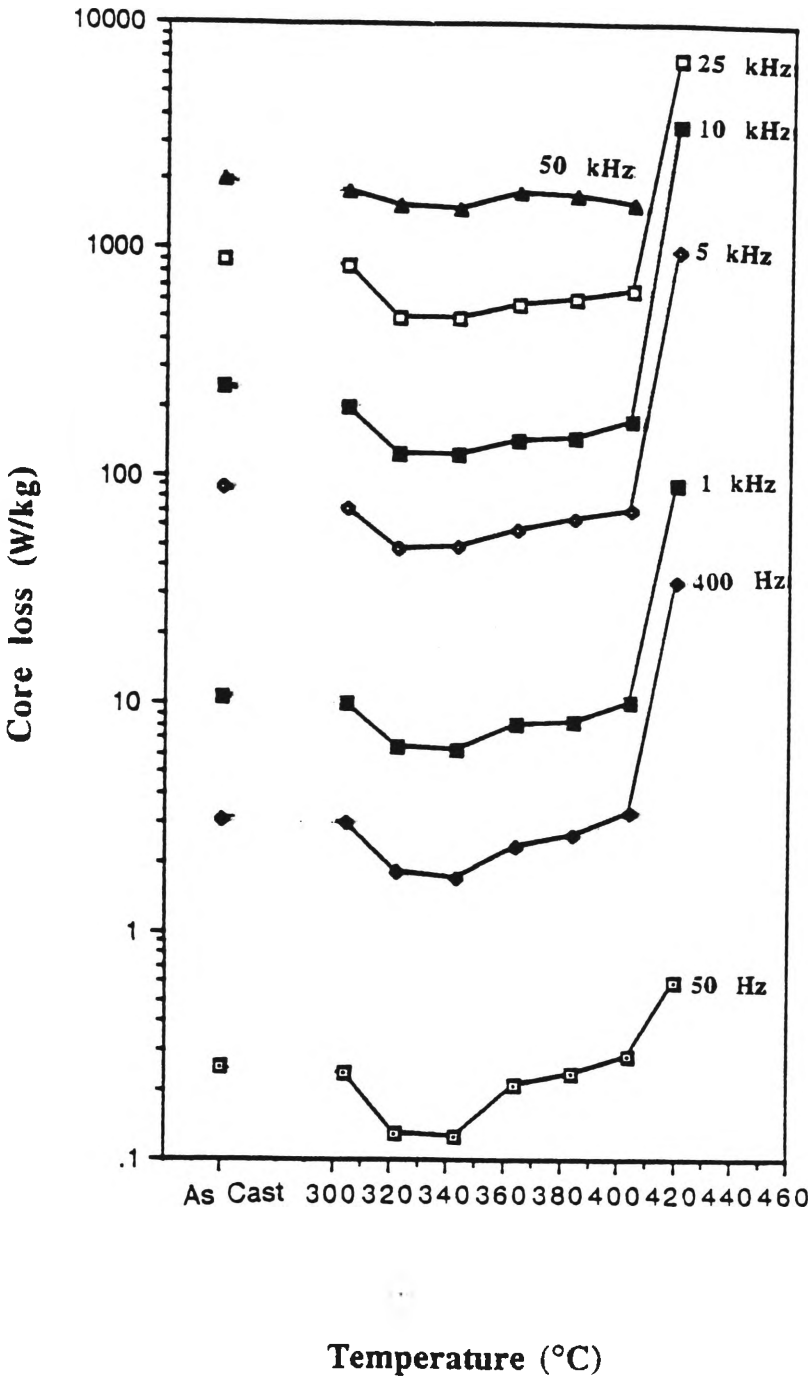

Fig.4.3.5 Core loss (L_T) vs. temperature (T_a) at B = 0.9 Tesla for $Fe_{60}Ni_{20}Si_{10}B_{10}$ at different frequencies.

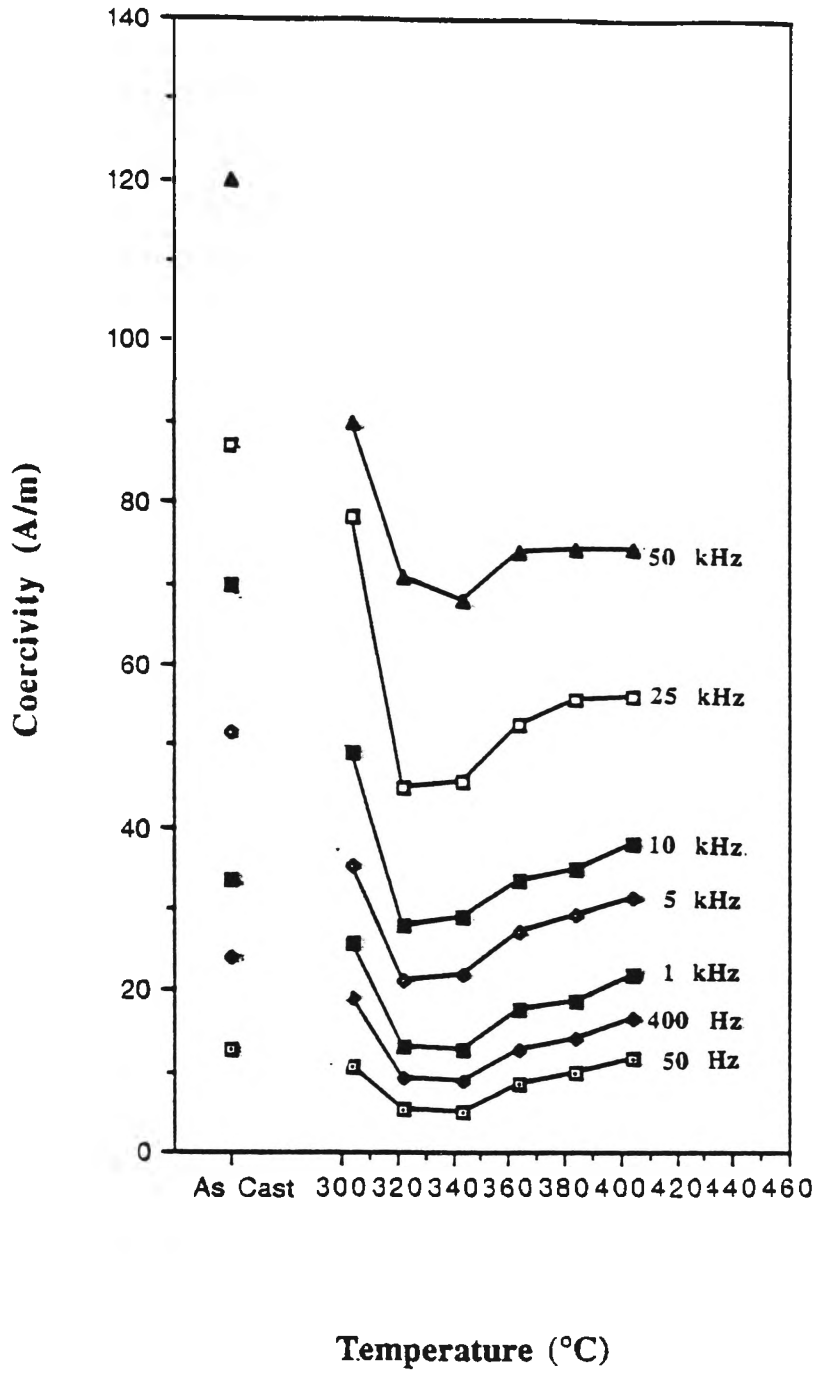

Fig.4.3.6 Coercivity (H_c) vs. temperature (T_a) at B = 0.9 Tesla for $Fe_{60}Ni_{20}Si_{10}B_{10}$ at different frequencies.

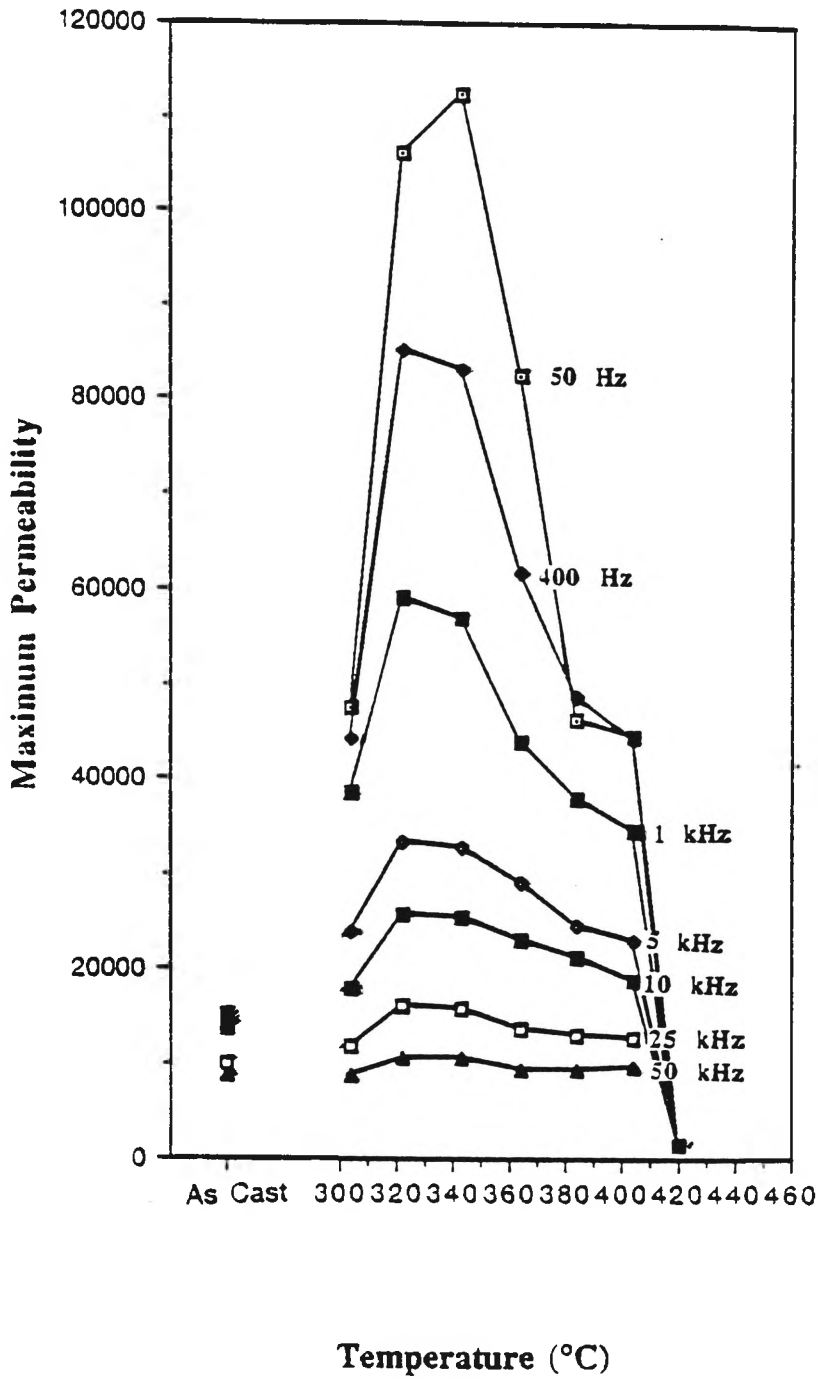

Fig.4.3.7 Maximum permeability (μ_{max}) vs. temperature (T_a) for $Fe_{60}Ni_{20}Si_{10}B_{10}$ at different frequencies.

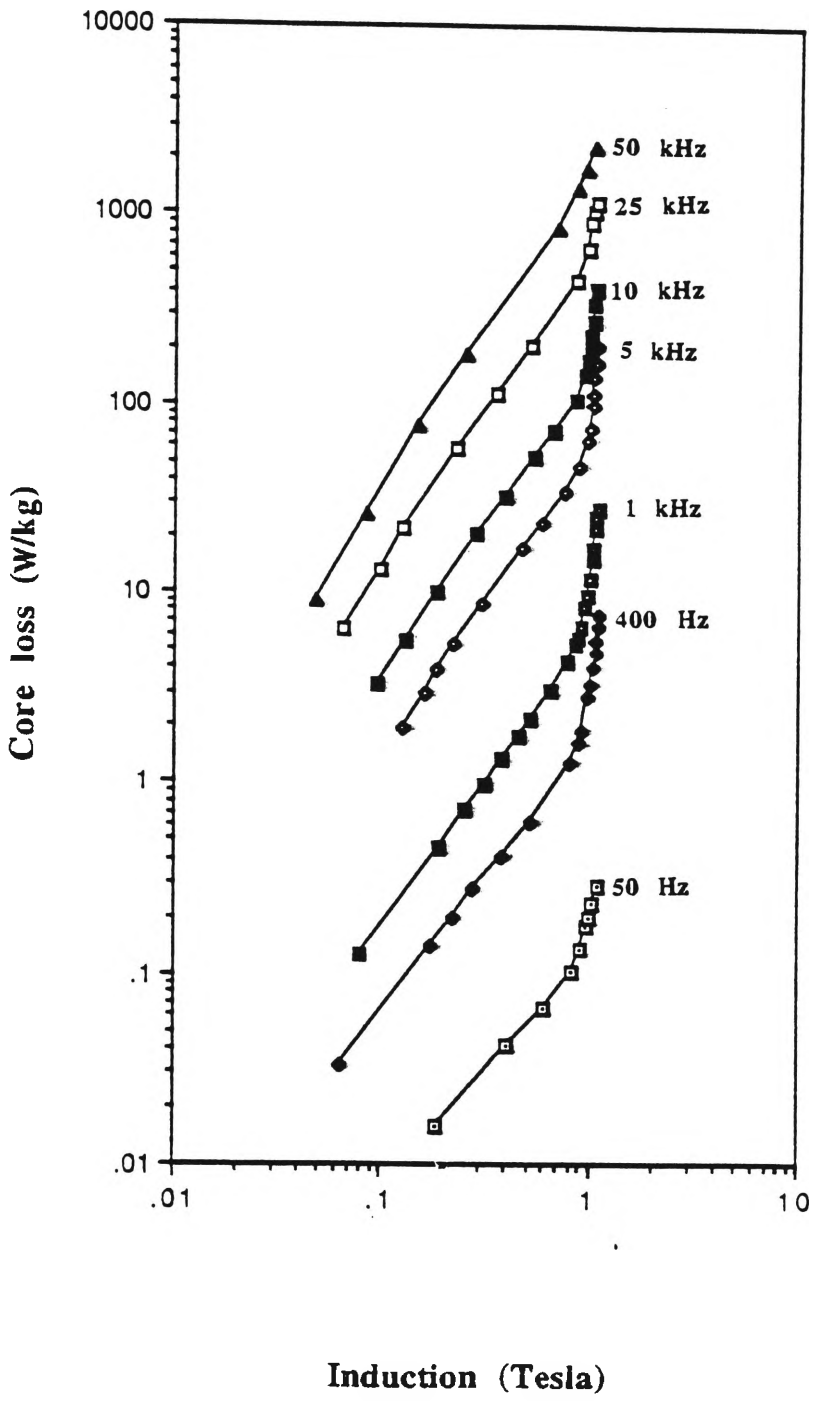

Fig.4.3.8 Core loss at different inductions for $Fe_{60}Ni_{20}Si_{10}B_{10}$ ribbon annealed for 60 mins. at 322°C.

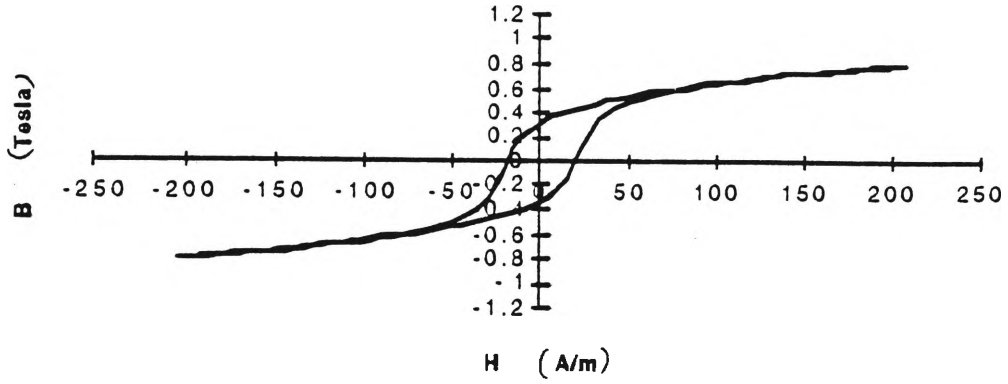

(a) For as-cast ribbon

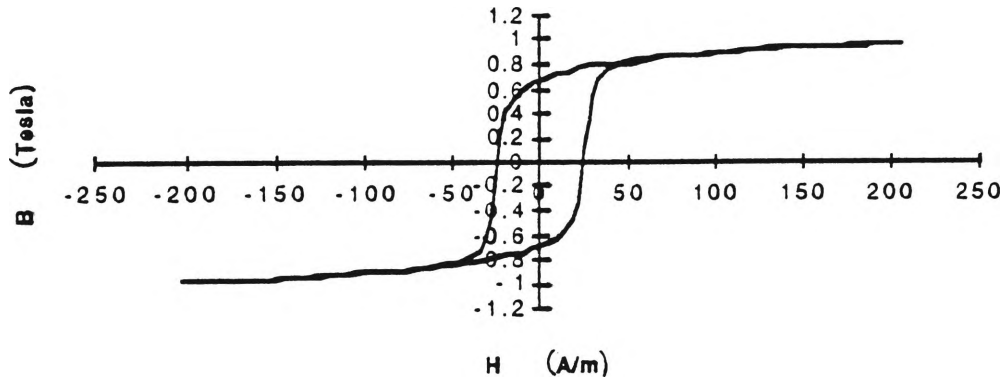

(b) For ribbon annealed as 304°C for 60 mins.

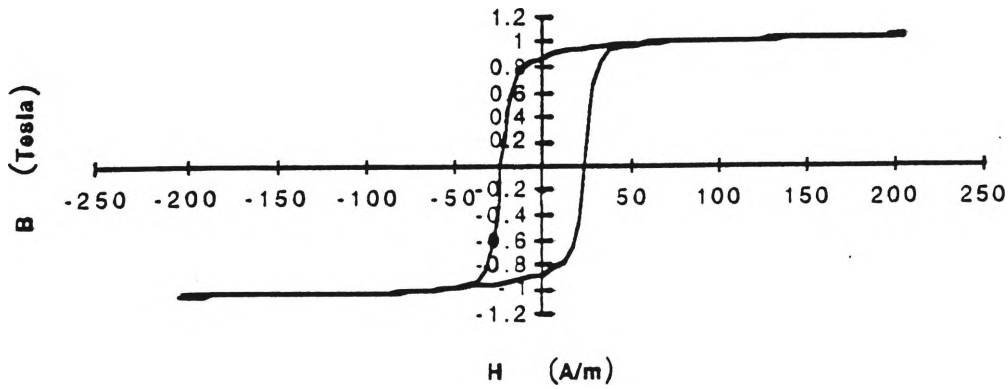

(c) For ribbon annealed as 322°C for 60 mins.

Fig.4.3.9 (continue)

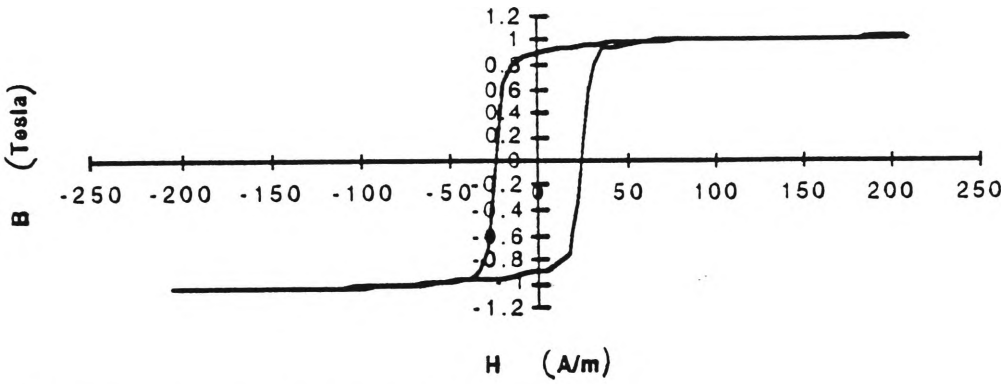

(d) For ribbon annealed as 343°C for 60 mins.

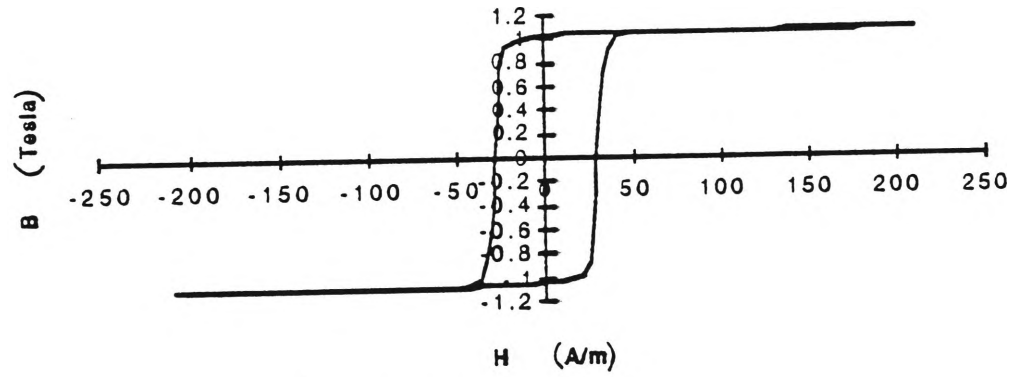

(e) For ribbon annealed as 364°C for 60 mins.

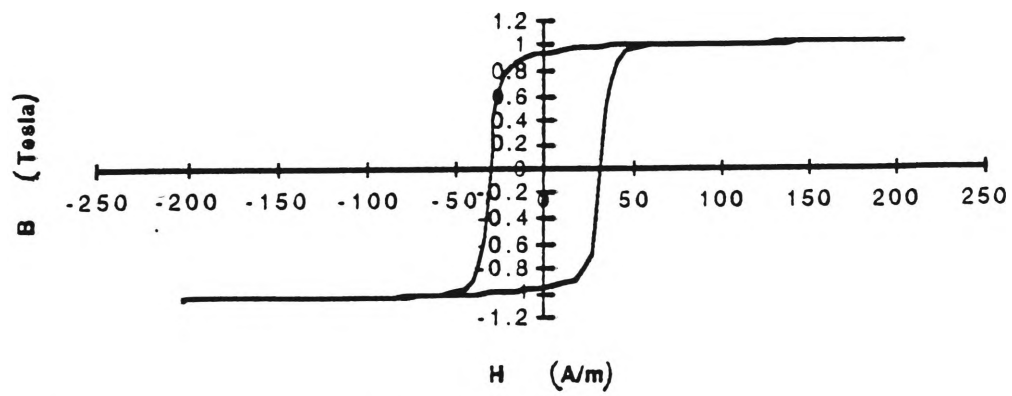

(f) For ribbon annealed as 384°C for 60 mins.

Fig.4.3.9 (continue)

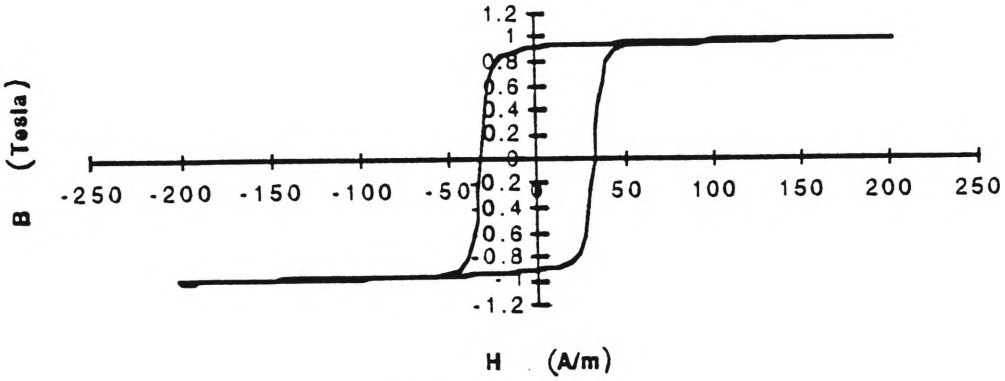

(g) For ribbon annealed as 404°C for 60 mins.

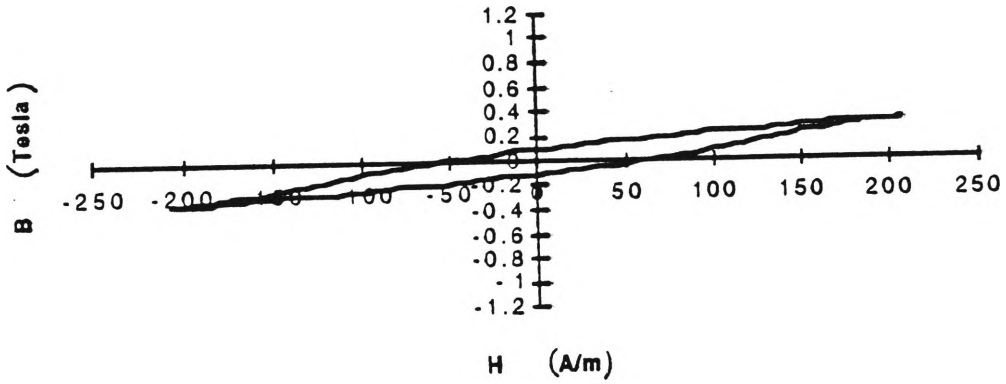

(h) For ribbon annealed as 420°C for 60 mins.

Fig.4.3.9 Hysteresis loops for $Fe_{60}Ni_{20}Si_{10}B_{10}$ ribbon annealed at different temperatures. The loops were measured at 400 Hz with an applied magnetic field of 200 A/m ± 10 A/m.

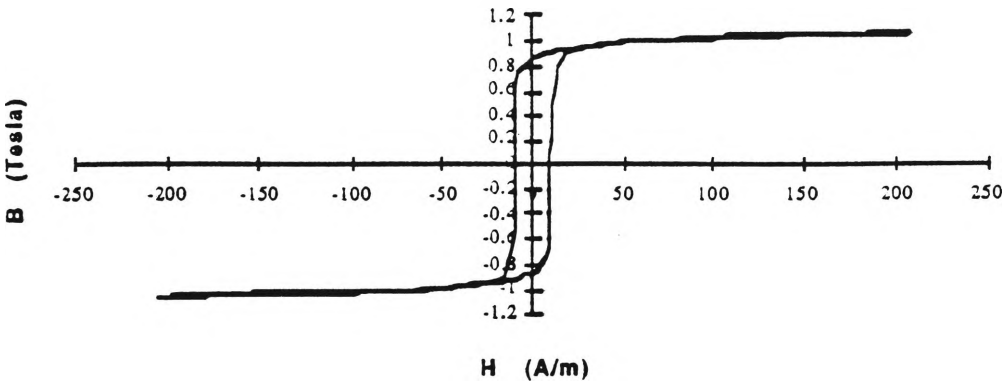

(a) at 50 Hz

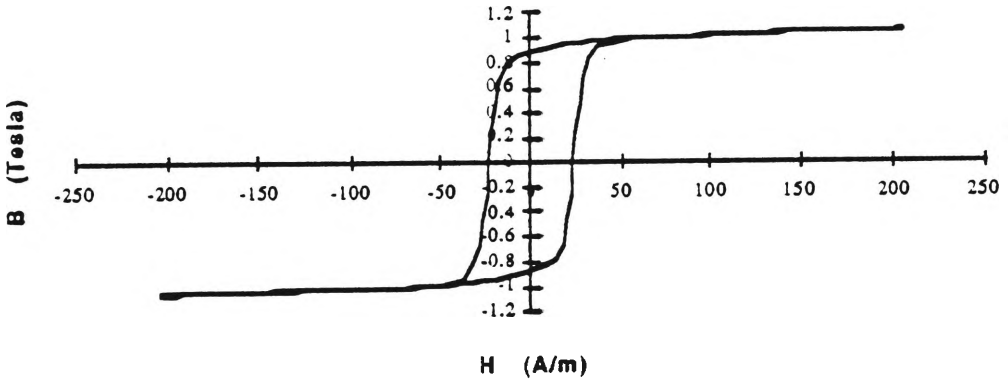

(b) at 400 Hz

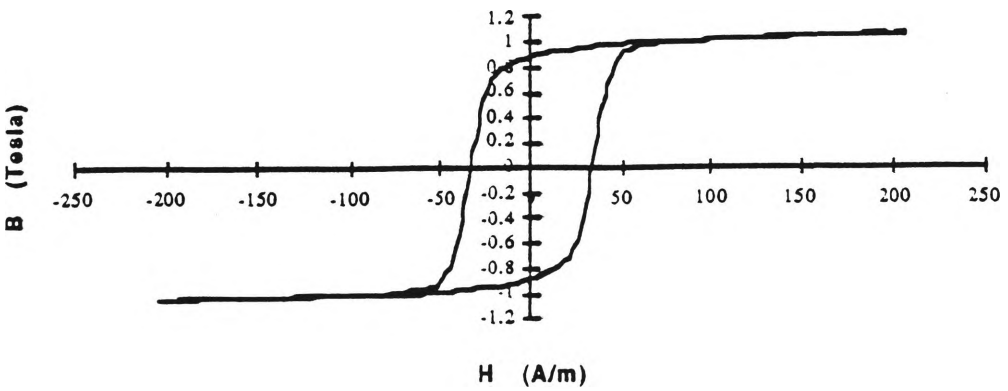

(c) at 1kHz

Fig.4.3.10 (continue)

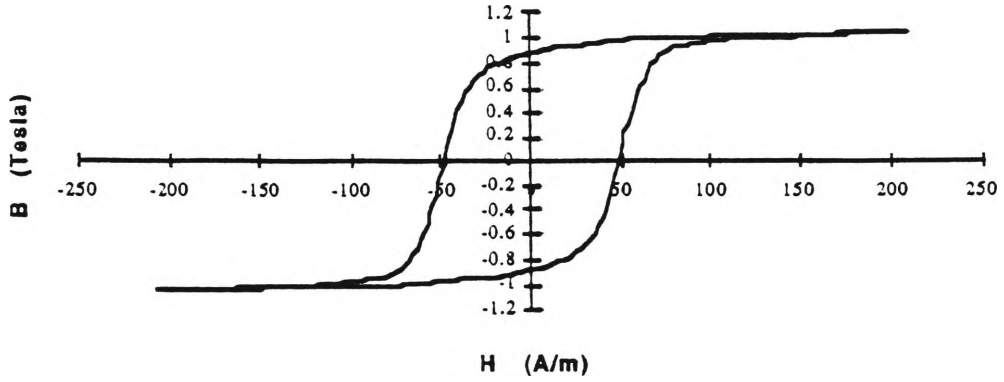

(d) at 5kHz

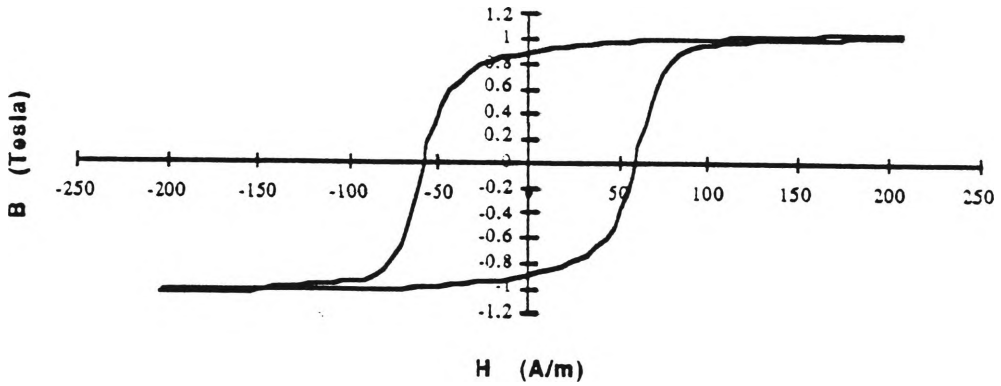

(e) at 10kHz

Fig.4.3.10 (continue)

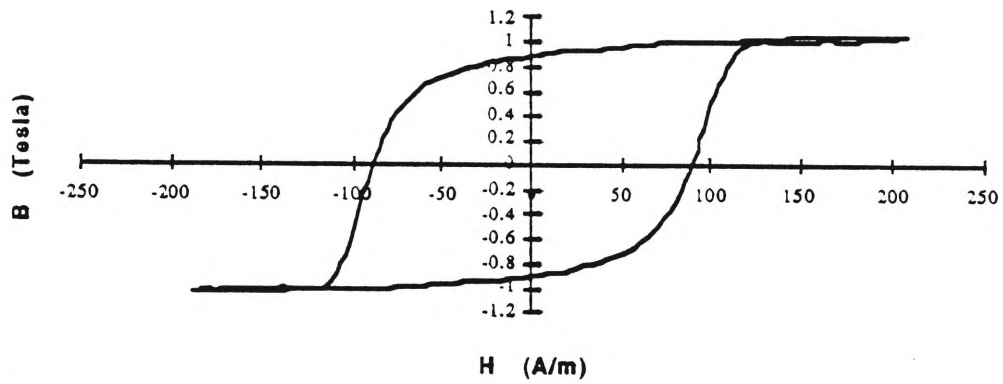

(f) at 25kHz

Fig.4.3.10 The change in the shape of the hysteresis loop for $Fe_{60}Ni_{20}Si_{10}B_{10}$ ribbon annealed for 60 mins. at 322°C with frequency. The hysteresis loops were measured with an applied field of 200 A/m ± 10 A/m.

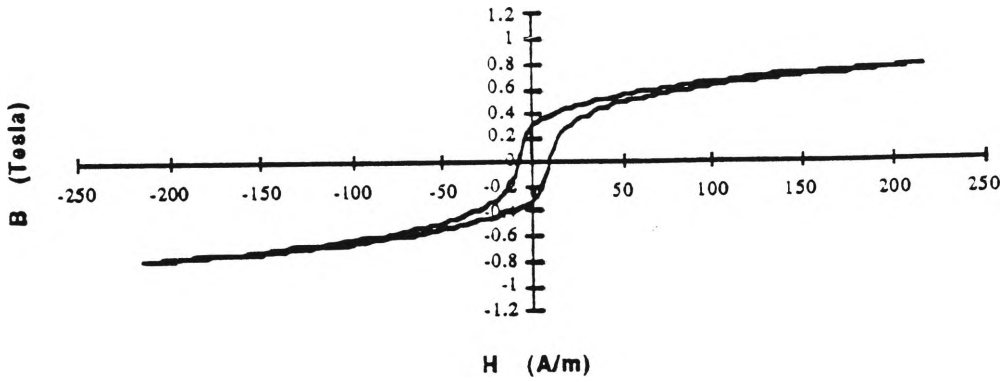

(a) For as-cast ribbon

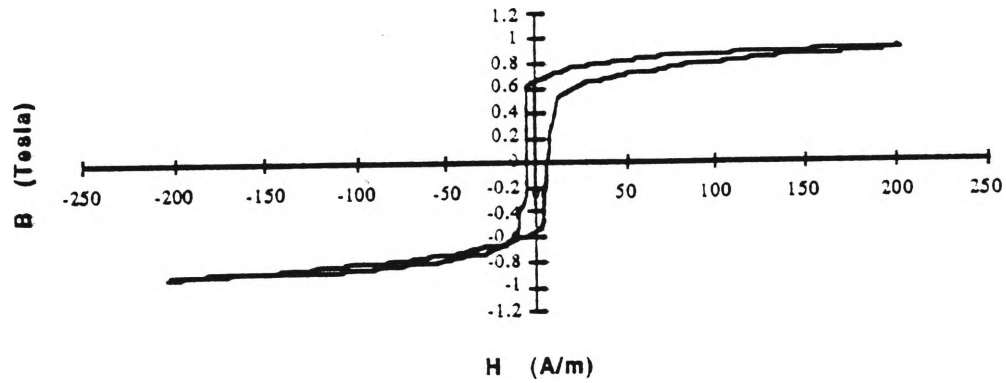

(b) For ribbon annealed at 304°C for 60 mins.

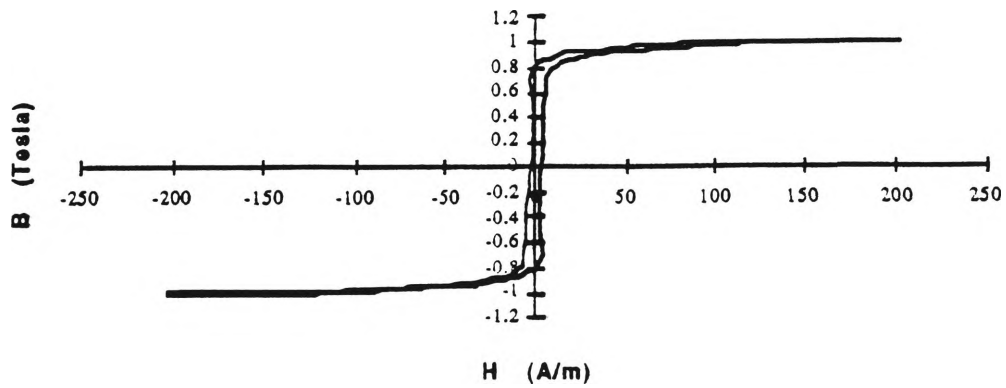

(c) For ribbon annealed at 322°C for 60 mins.

Fig.4.3.11 (continue)

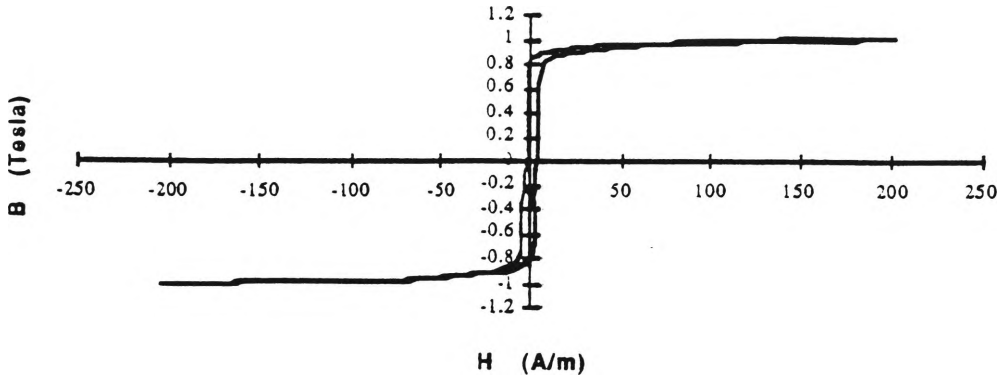

(d) For ribbon annealed at 343°C for 60 mins.

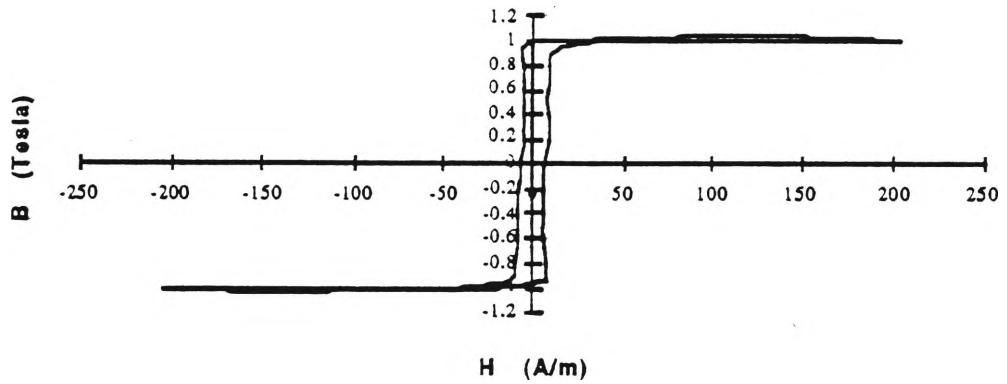

(e) For ribbon annealed at 364°C for 60 mins.

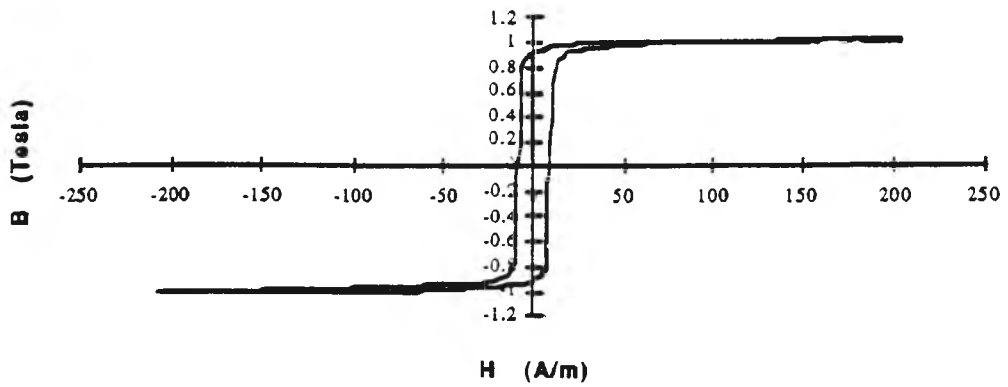

(f) For ribbon annealed at 382°C for 60 mins.

Fig.4.3.11 (continue)

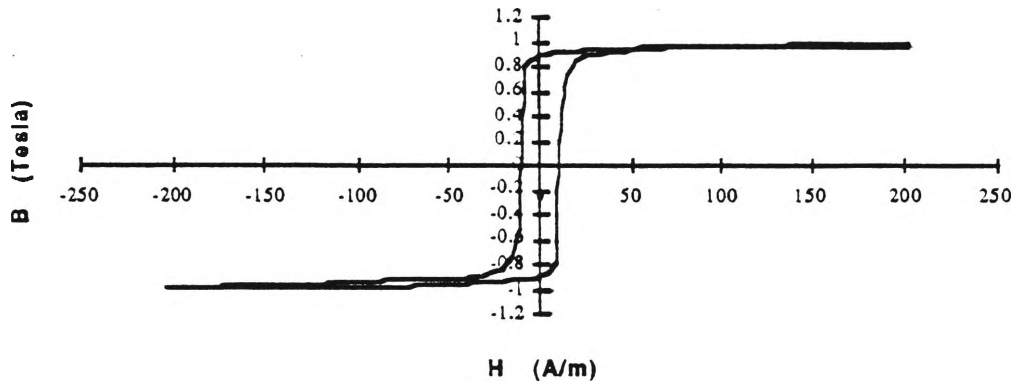

(g) For ribbon annealed at 404°C for 60 mins.

Fig.4.3.11 Change in the coercivity of the hysteresis loop for $Fe_{60}Ni_{20}Si_{10}B_{10}$ ribbon with increase in annealing temperature at 1 Hz frequency. The loops were measured at 400 Hz with an applied magnetic field of 200 A/m ± 10 A/m.

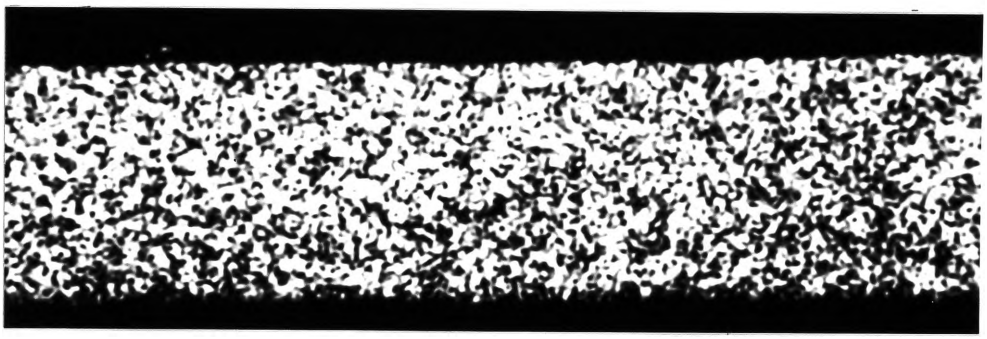

Fig.4.3.12 Optical micrograph of a cross-section for $Fe_{60}Ni_{20}Si_{10}B_{10}$ ribbon annealed for 60 mins. at 420°C (X 500).

4.4 Magnetic Properties of $Fe_{72}Si_{10}B_{18}$ ribbon

Fig.4.4.1 shows the dynamic DSC trace at a rate of 20°C/min. of an $Fe_{72}Si_{10}B_{18}$ sample. It shows only one exothermic peak at 584°C. The DSC thermogram also showed a small endothermic peak at 451°C as shown in Fig.4.4.2. To confirm that the endothermic peak corresponds to the Curie temperature, the susceptibility method was also used to measure the Curie temperature as shown in Fig.4.4.3. The Curie point temperature matches the endothermic peak in the DSC trace.

Fig.4.4.4 and Fig.4.4.5 show the core loss vs. temperature at 1.0 Tesla induction for different frequencies. $Fe_{72}Si_{10}B_{18}$ does not show any sign of an optimum annealing temperature in the results. At annealing temperatures above 500°C, the magnetic properties of the material cannot be measured by this instrument.

The change in the coercivity with temperature at 1.0 Tesla induction is shown in Fig.4.4.6. Like core loss, the coercivity changes with annealing temperature but there was no clear evidence of an optimum annealing temperature.

Fig.4.4.7 shows the maximum permeability for different annealing temperatures at different operating frequencies.

Figs.4.4.8a-c show the core loss at different inductions for $Fe_{72}Si_{10}B_{18}$ ribbon annealed for 60 mins. at different annealing temperatures. Fig.4.4.8a is for the as-cast ribbon. Fig.4.4.8b is for the ribbon annealed for 60 mins. at a temperature below the Curie point (i.e. at 405°C). Fig.4.4.8c is for the ribbon annealed for 60 mins. at a temperature above the Curie point (i.e. at 460°C). Note the variations in the log-log graphs. Ideally, the plots should be straight lines until the saturation magnetic induction is reached. These fluctuation are due to the instrumental limitations in

measuring the magnetic properties of high magnetostrictive samples. Due to this problem the estimated values of core loss are not shown for this sample in Fig.4.4.4 and Fig.4.4.5.

Fig.4 4.9a-i show the hysteresis loops at 400 Hz frequency and annealed at different temperatures for 60 mins. As the annealing temperature increases, the hysteresis loop changes very little until at 445°C the hysteresis loop starts to become skewed.

Figs.4.4.10a-f show hysteresis loops at different frequencies for the $Fe_{72}Si_{10}B_{18}$ as-cast sample. As the frequency increases the hysteresis loop becomes wider and as a result the core loss and coercivity increase. These hysteresis loops were plotted at 200 A/m ± 10 A/m applied magnetic field. Note the change in the loop shape at 25 kHz frequency. This is due to the problem of measuring magnetic properties of a magnetostrictive sample with this instrument.

In the $Fe_{72}Si_{10}B_{18}$ sample, the soft magnetic properties start to deteriorate well before optically-observable crystallisation. Hence the size of the exothermic peak was measured by DSC for samples pre-annealed at different temperatures for 60 mins. The graph of heat release vs. annealing temperature of the sample is shown in Fig.4.4.11.

Fig.4.4.12 shows the hysteresis loops measured at 1 Hz frequency for a ribbon annealed at 480°C for 60 mins. The hysteresis loops were measured before and after chemically removing 25% of the total mass of the ribbon by dil. HNO_3.

Fig.4.4.13 shows the hysteresis loops measured at 1 Hz frequency for an as-cast ribbon of $Fe_{72}Si_{10}B_{18}$ before and after chemically removing 25% of the ribbon mass. The hysteresis loop remains the same. Hence it is clear that the changes evident

in Fig.4.4.12 are due to effects produced on annealing. This change starts well before the beginning of optically-observable crystallisation.

Fig.4.4.14 shows the microstructure of an $Fe_{72}Si_{10}B_{18}$ sample annealed for 60 mins. at 515°C.

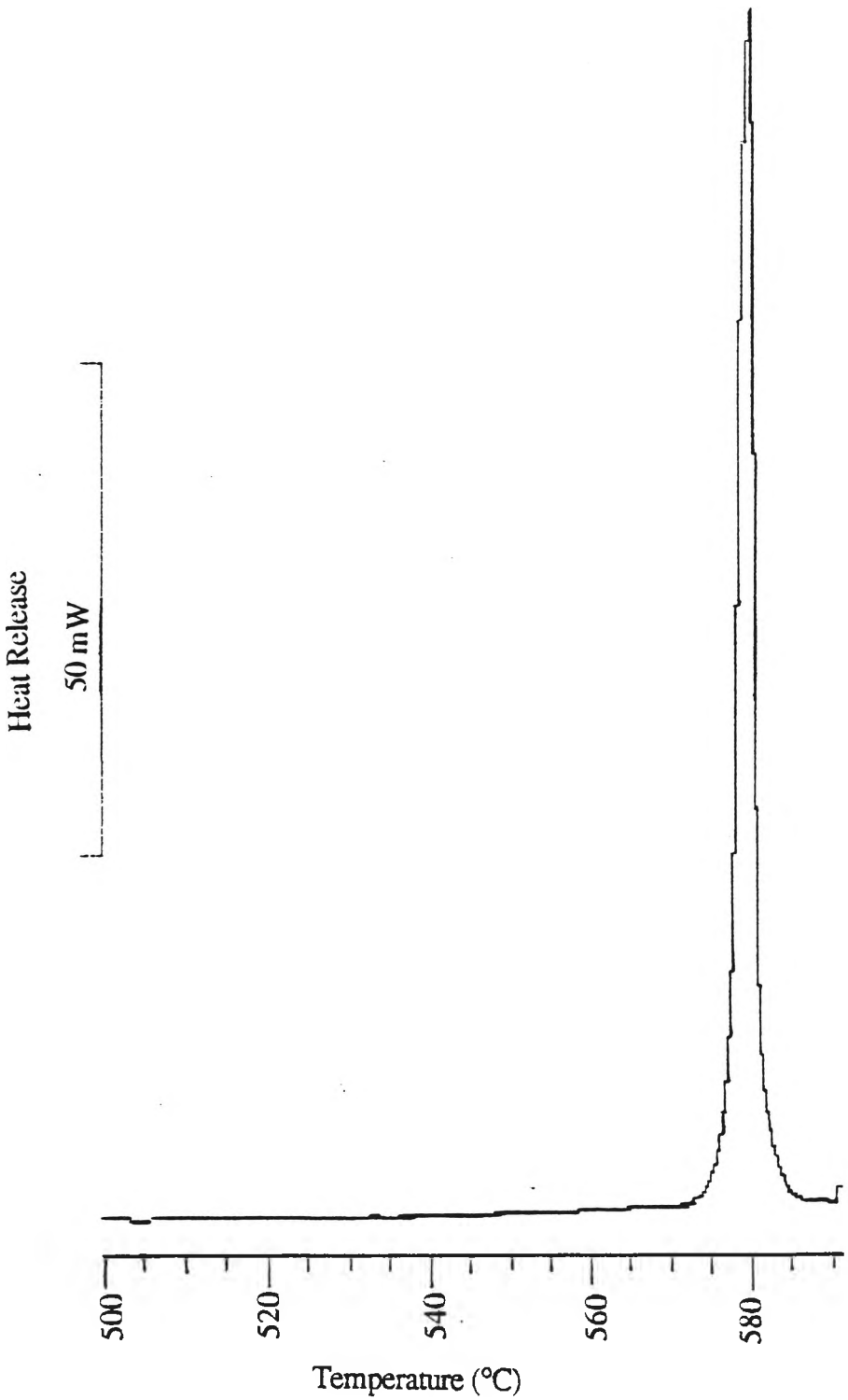

Fig.4.4.1 Dynamic DSC thermogram for $Fe_{72}Si_{10}B_{18}$ (20°C/min.).

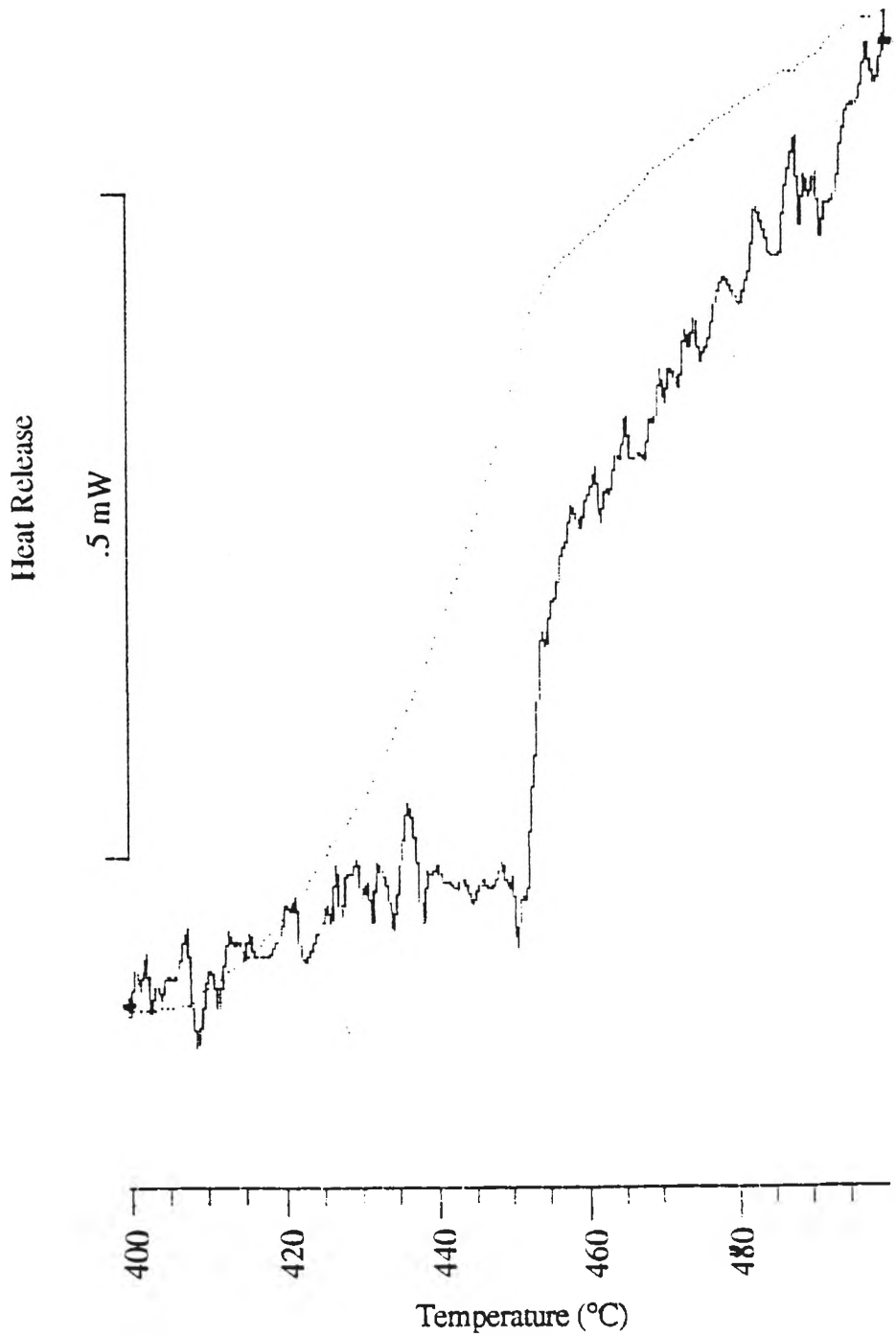

Fig.4.4.2 Curie temperature for $Fe_{72}Si_{10}B_{18}$ measured by DSC.

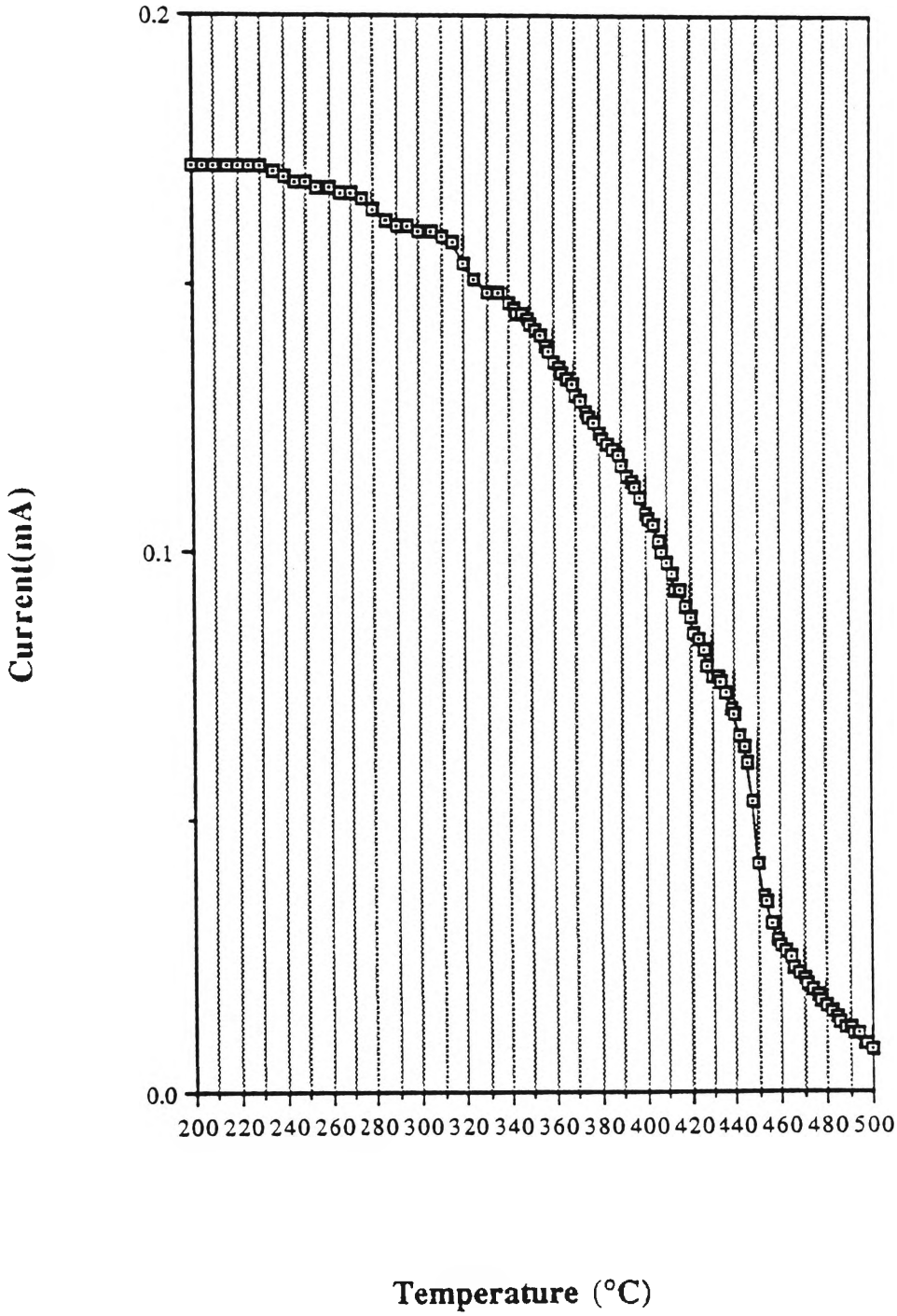

Fig.4.4.3 Measurement of Curie temperature for $Fe_{72}Si_{10}B_{18}$ ribbon by the susceptibility method.

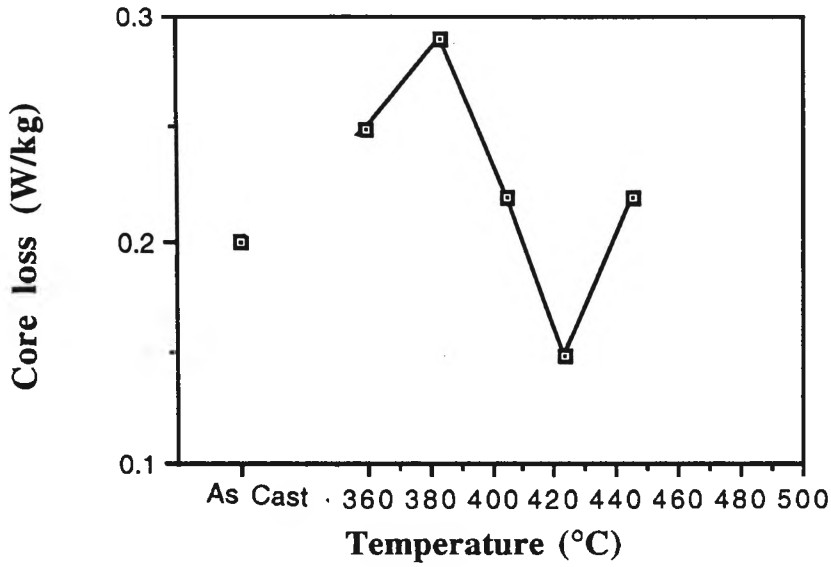

(a) at 50 Hz

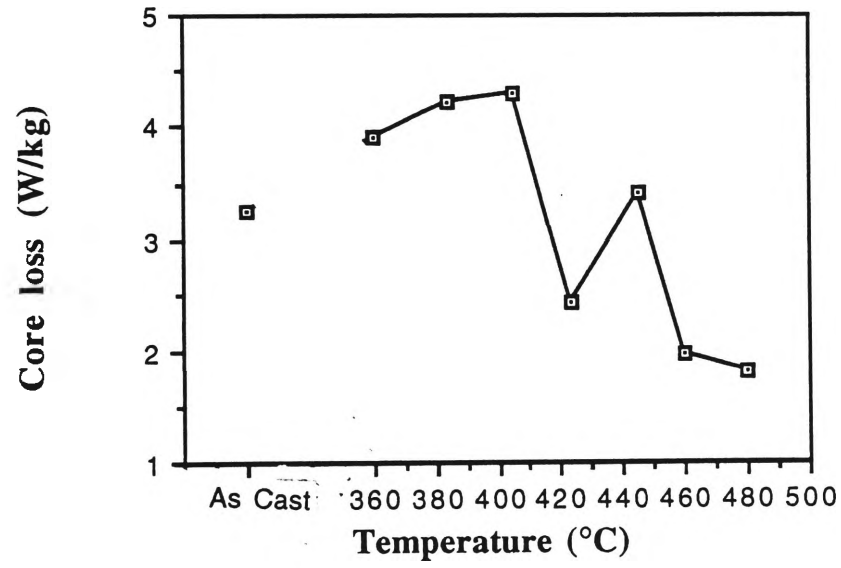

(b) at 400 Hz

Fig.4.4.4 (continue)

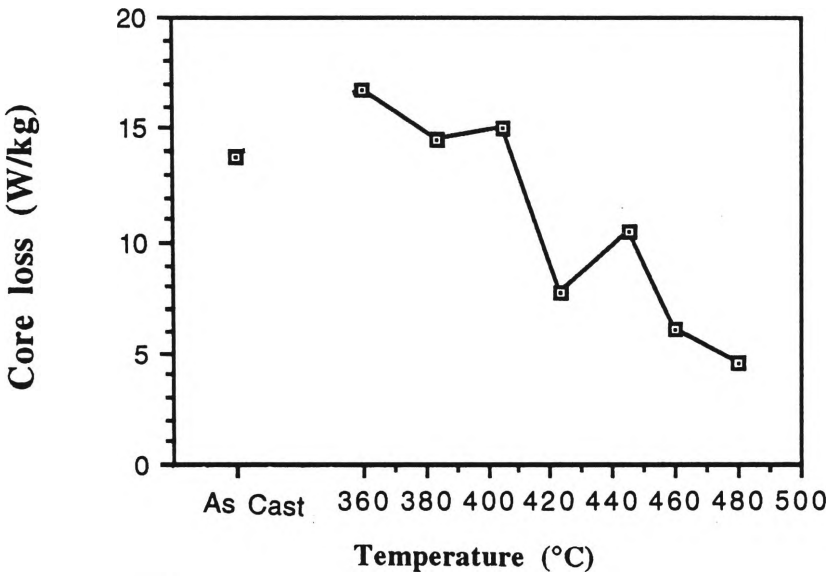

(c) at 1 kHz

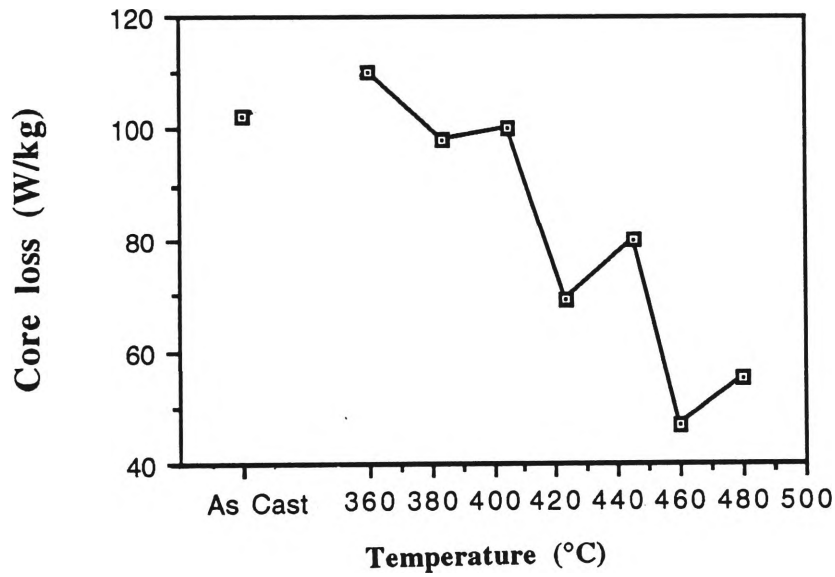

(d) at 5 kHz

Fig.4.4.4 (continue)

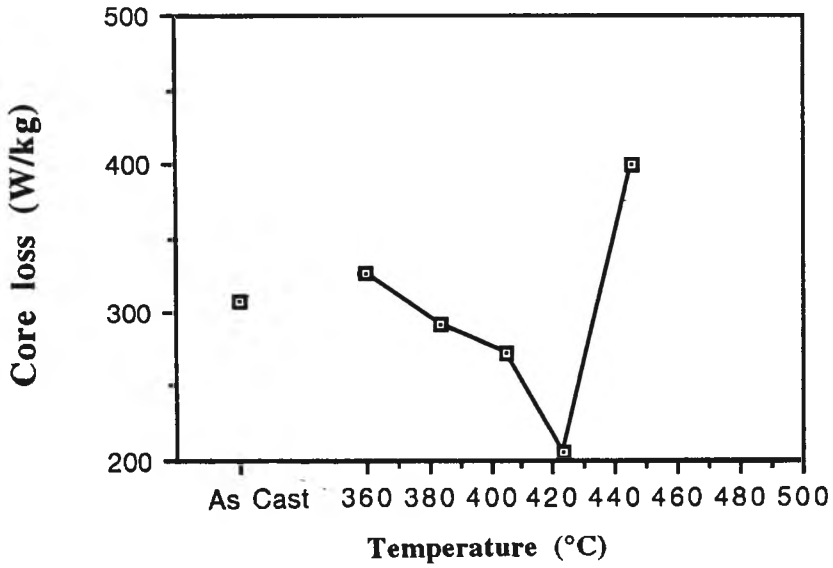

(e) at 10 kHz

Fig.4.4.4 Core loss (L_T) vs. annealing temperature (T_a) at B = 1.0 Tesla for $Fe_{72}Si_{10}B_{18}$ ribbon at different frequencies.

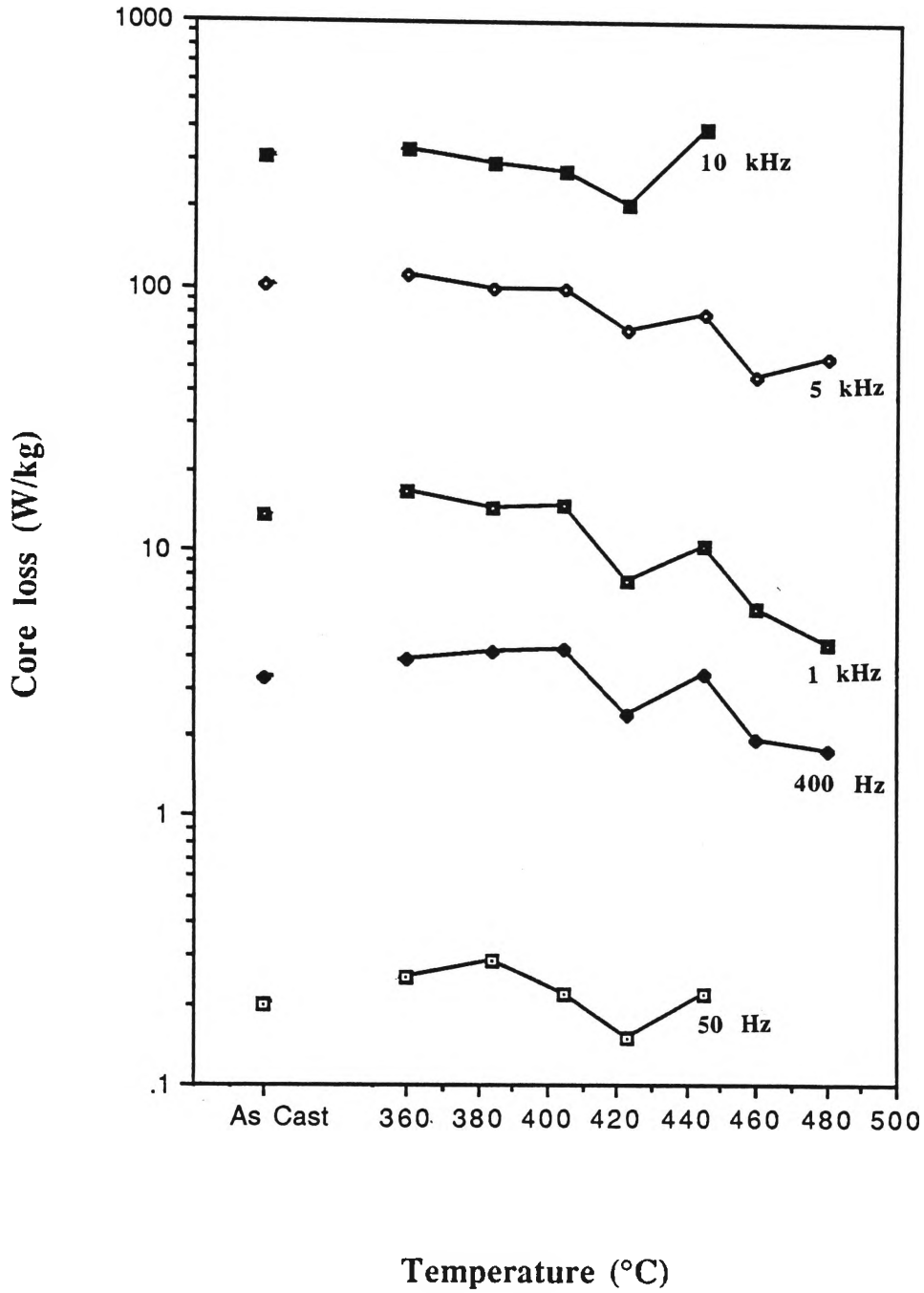

Fig.4.4.5 Core loss (L_T) vs. temperature (T_a) at B = 1.0 Tesla for $Fe_{72}Si_{10}B_{18}$ at different frequencies.

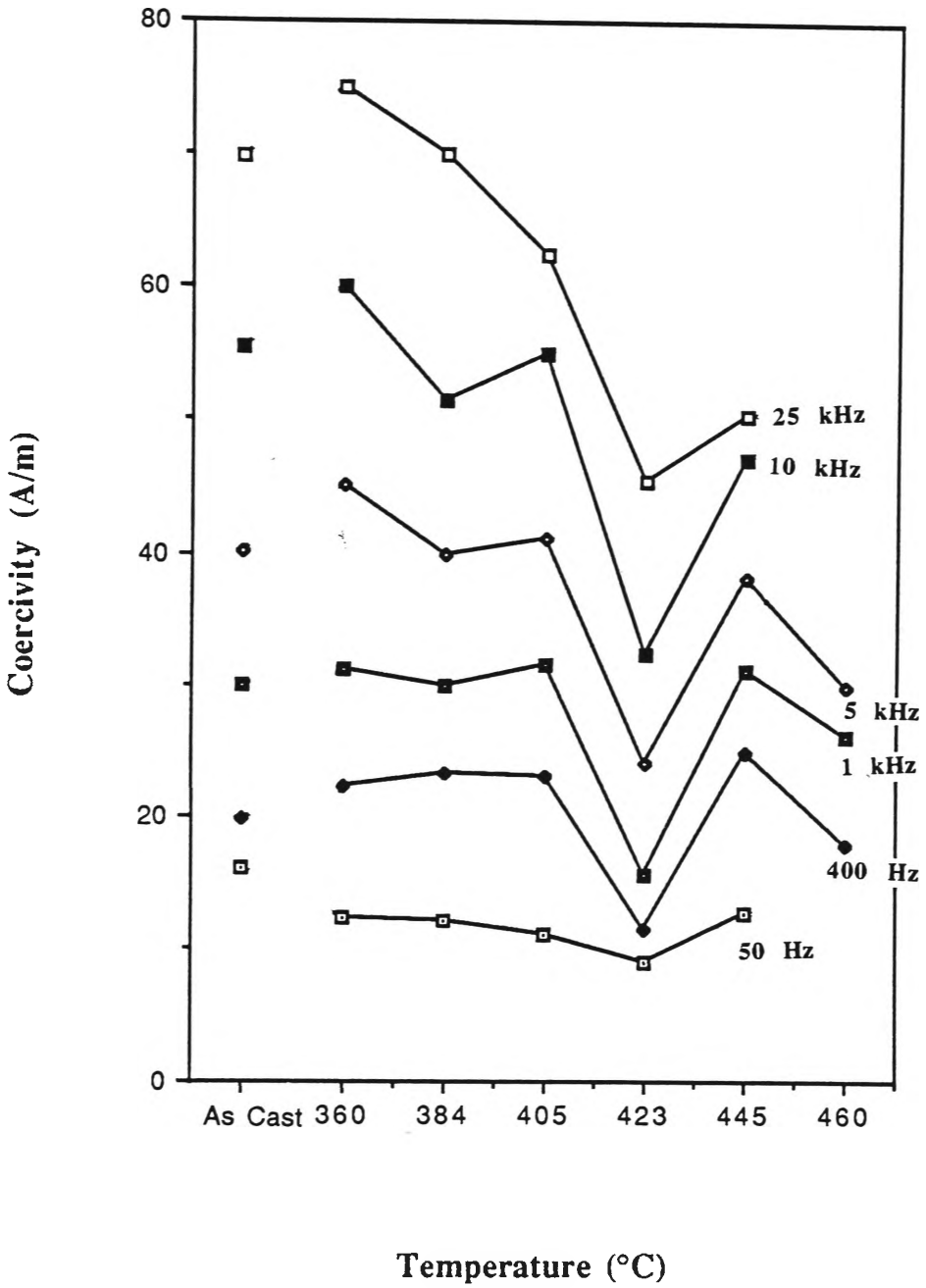

Fig.4.4.6 Coercivity (H_c) vs. annealing temperature (T_a) at B = 1.0 Tesla induction for $Fe_{72}Si_{10}B_{18}$ at different frequencies.

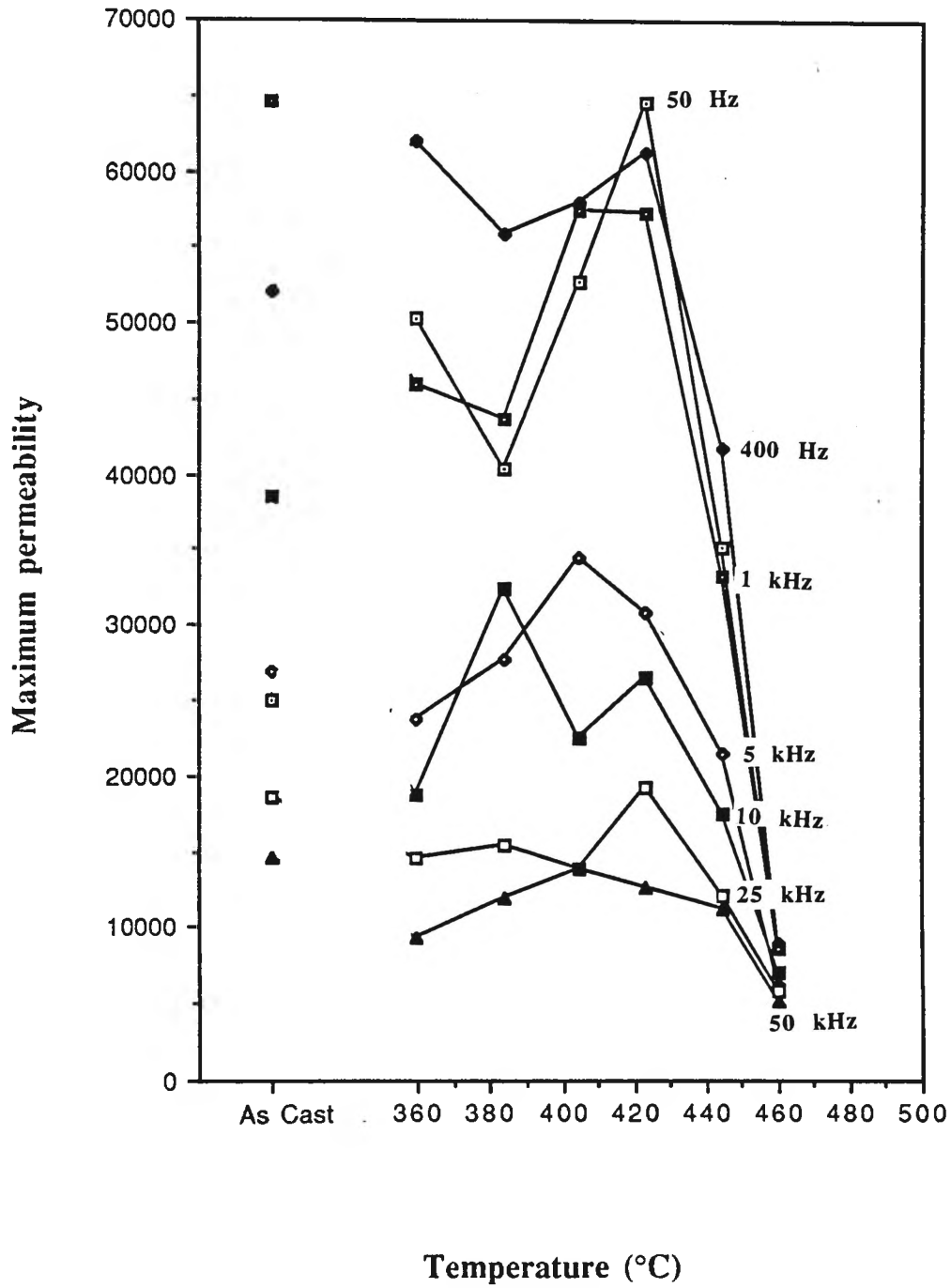

Fig.4.4.7 Maximum permeability (μ_{max}) vs. annealing temperature (T_a) for $Fe_{72}Si_{10}B_{18}$ ribbon at different frequencies.

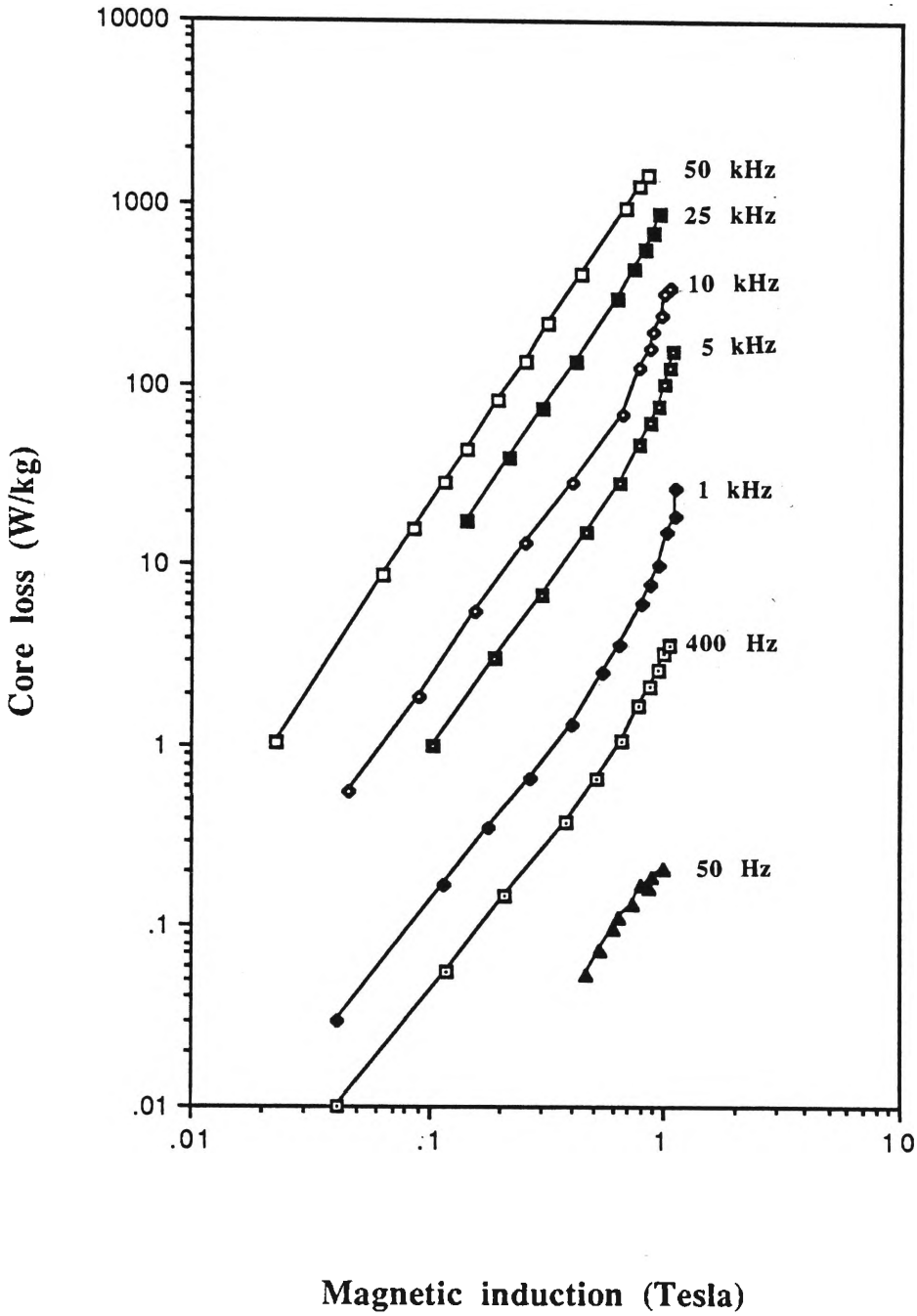

(a) For as-cast $Fe_{72}Si_{10}B_{18}$ ribbon.

Fig.4.4.8 (continue)

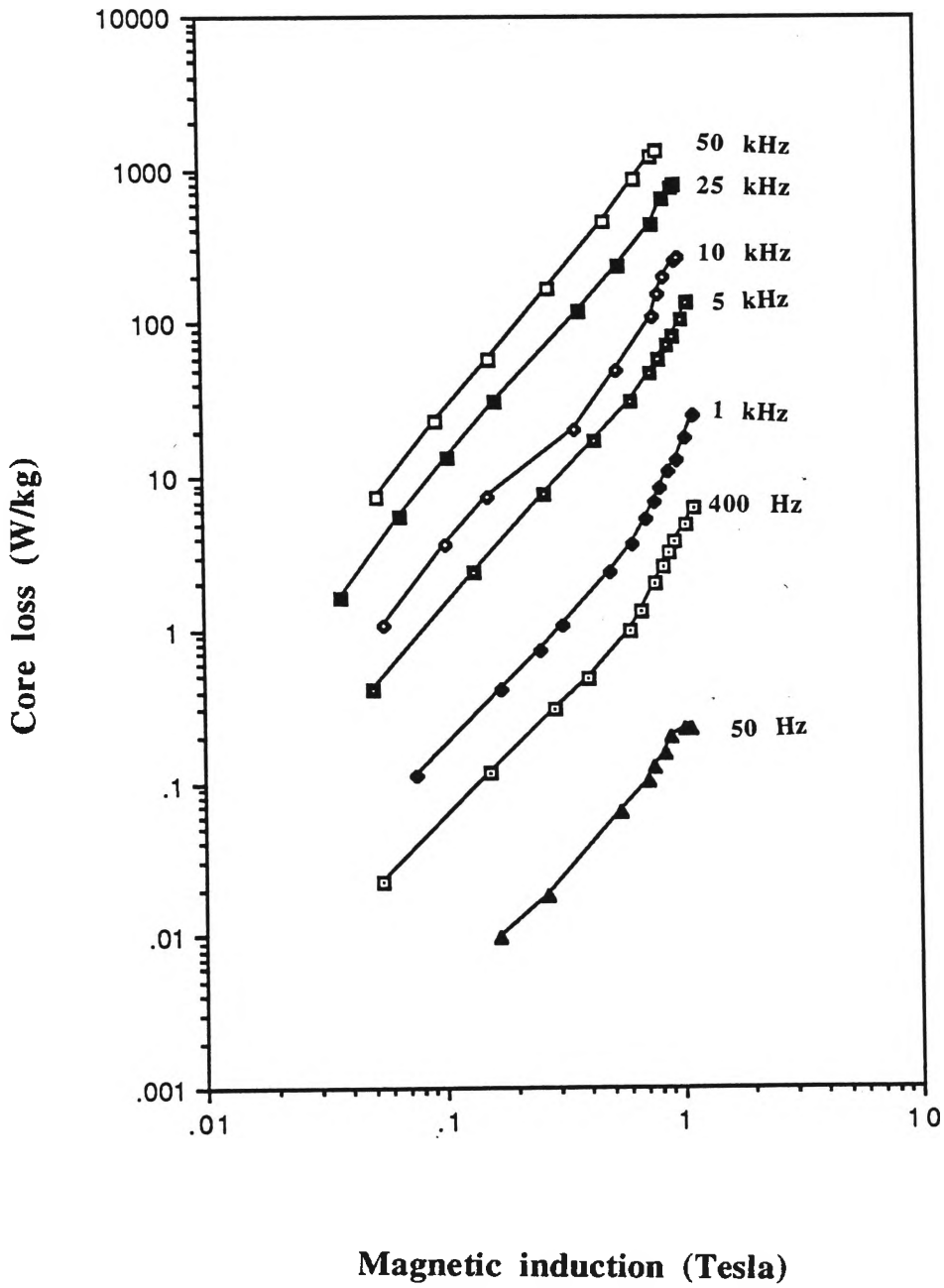

(b) For $Fe_{72}Si_{10}B_{18}$ ribbon annealed at 405°C for 60 mins.

Fig.4.4.8 (continue)

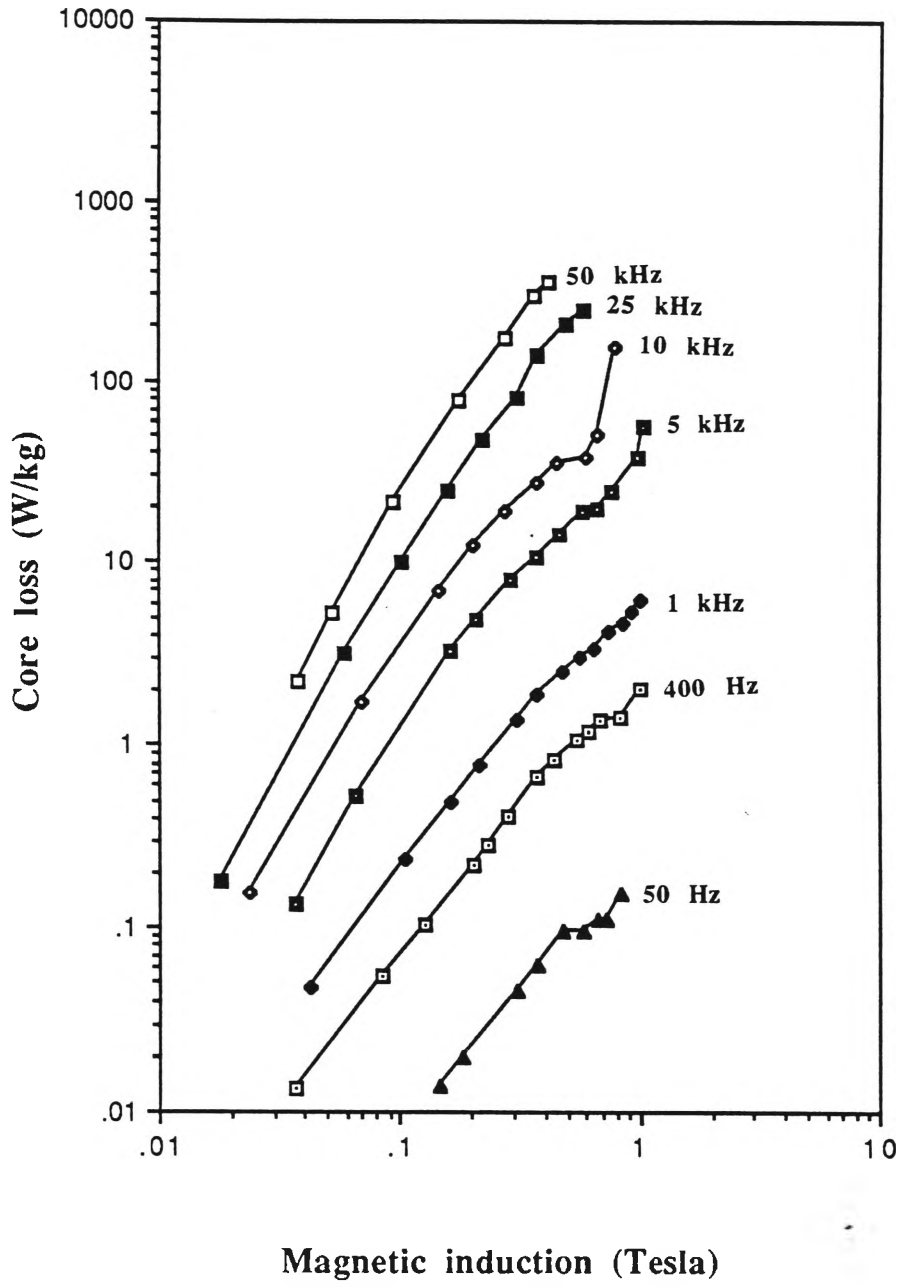

(c) For $Fe_{72}Si_{10}B_{18}$ ribbon annealed at 460°C for 60 mins.

Fig.4.4.8 Core loss at different inductions for $Fe_{72}Si_{10}B_{18}$ ribbon annealed for 60 mins. at different annealing temperatures.

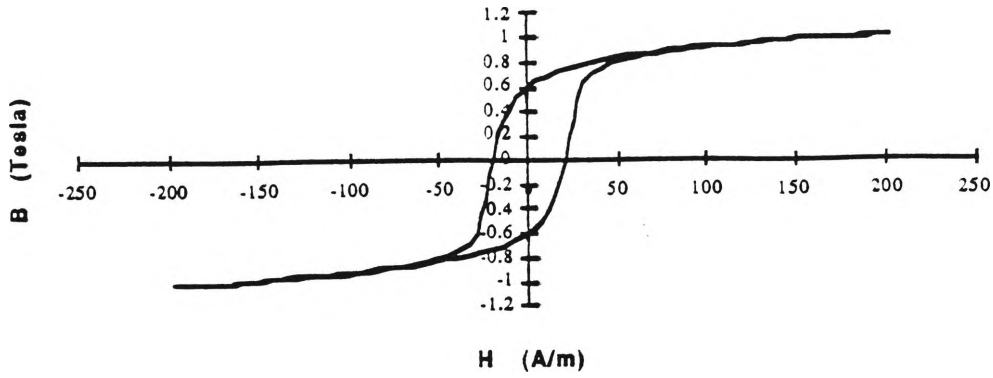

(a) For as-cast ribbon

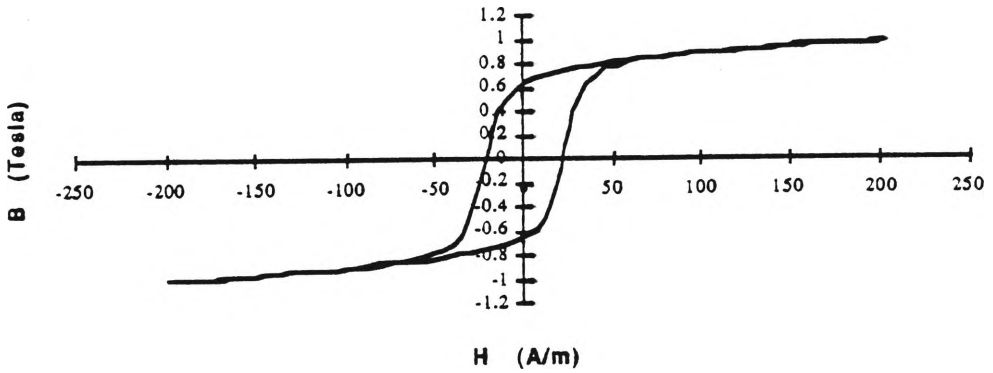

(b) For ribbon annealed for 60 at 363°C

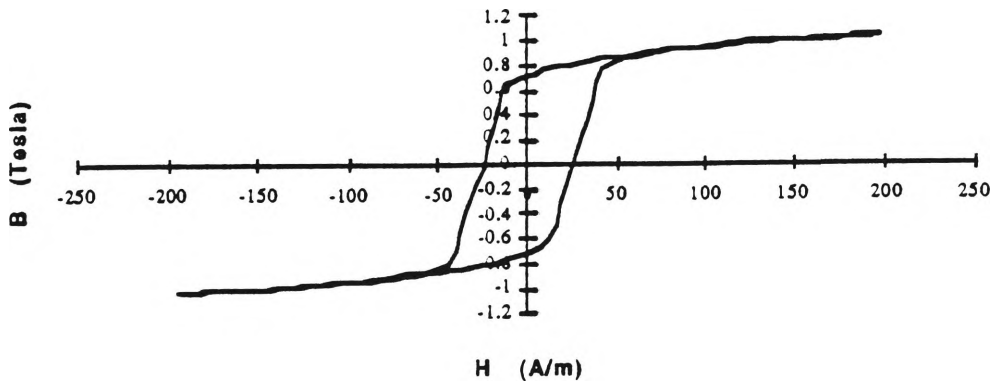

(c) For ribbon annealed for 60 at 384°C

Fig.4.4.9 (continue)

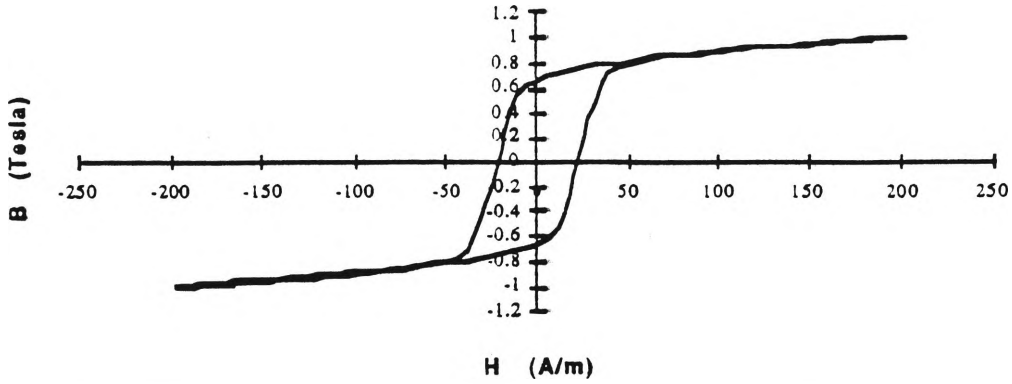

(d) For ribbon annealed for 60 at 405°C

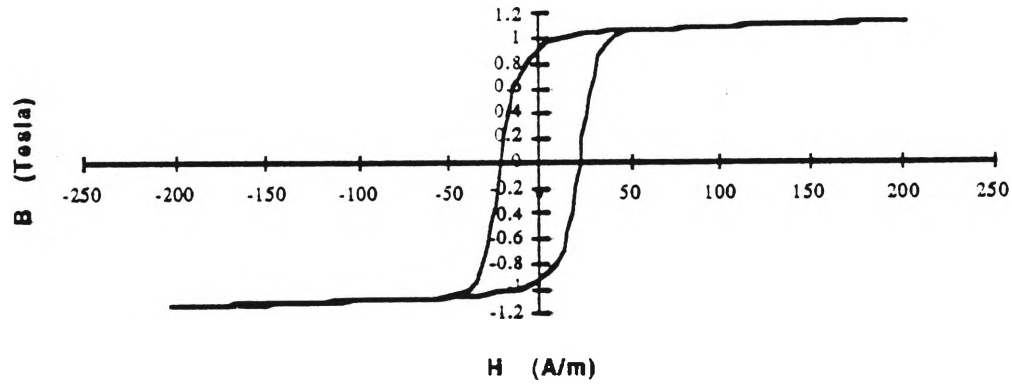

(e) For ribbon annealed for 60 at 423°C

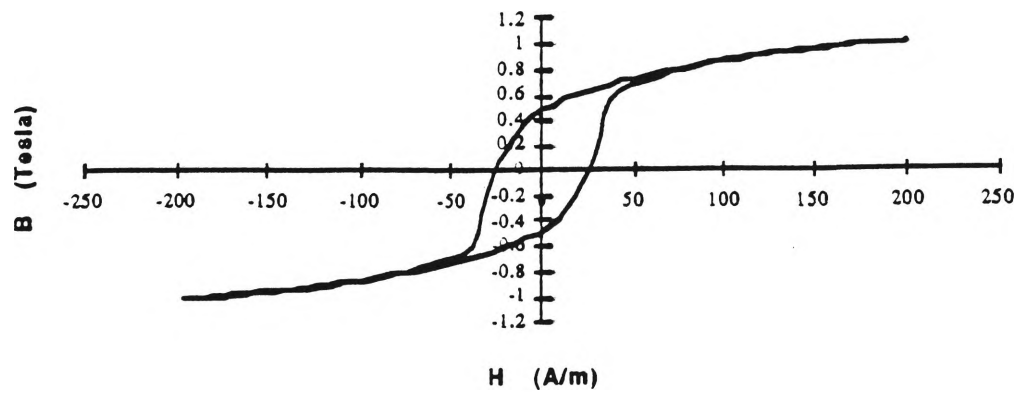

(f) For ribbon annealed for 60 at 445°C

Fig.4.4.9 (continue)

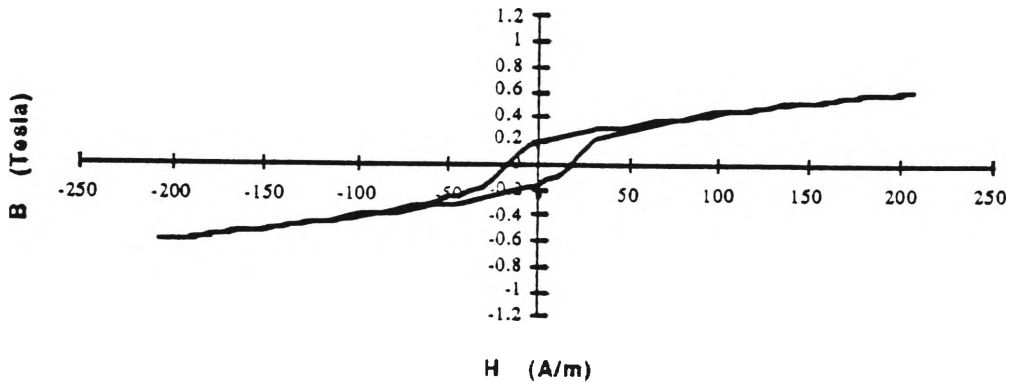

(g) For ribbon annealed for 60 at 460°C

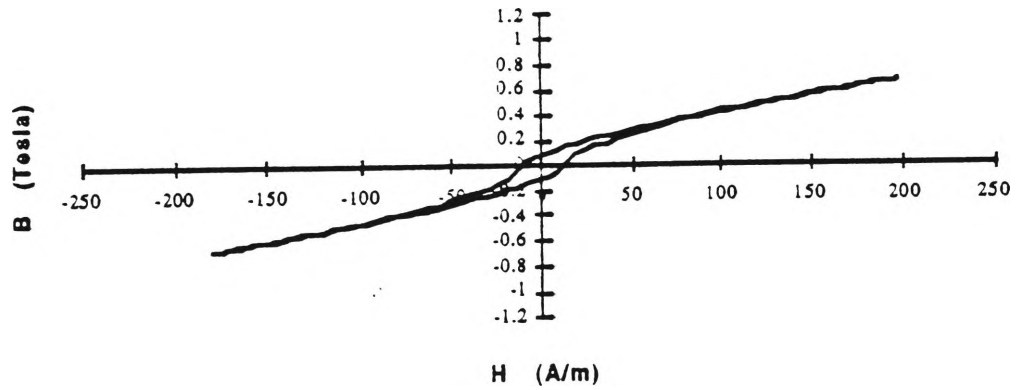

(h) For ribbon annealed for 60 at 480°C

Fig.4.4.9 (continue)

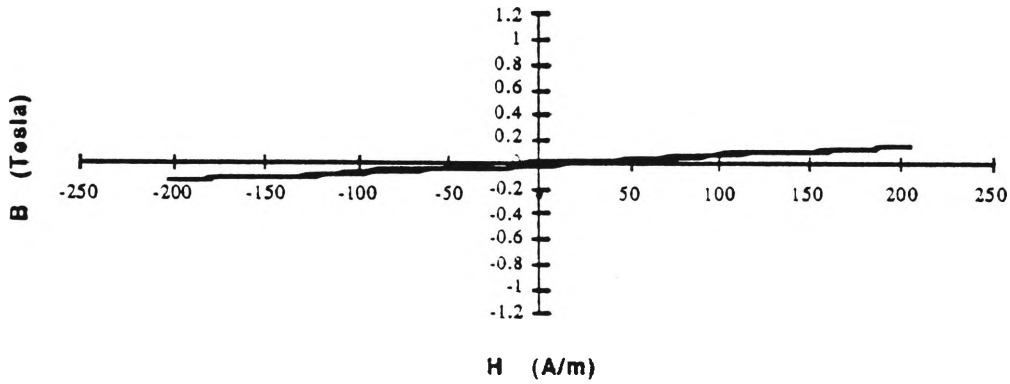

(i) For ribbon annealed for 60 at 500°C

Fig.4.4.9 Hysteresis loops for $Fe_{72}Si_{10}B_{18}$ ribbon annealed at different temperatures. The loops were measured at 400 Hz with an applied magnetic field of 200 A/m ± 10 A/m.

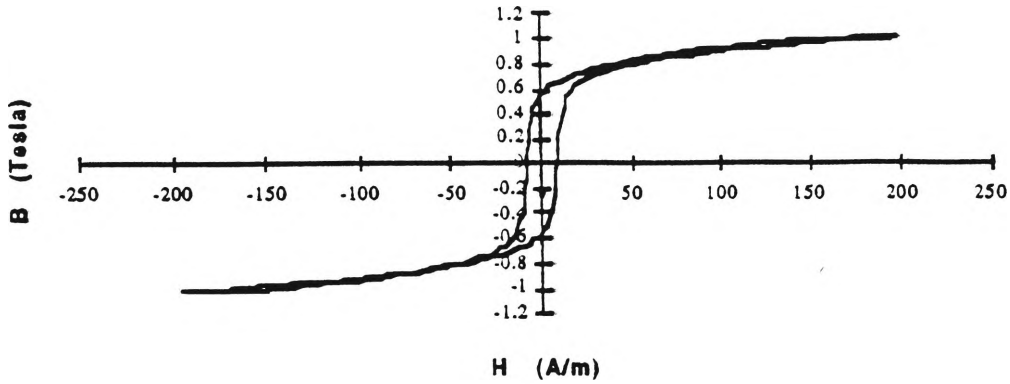

(a) at 50 Hz

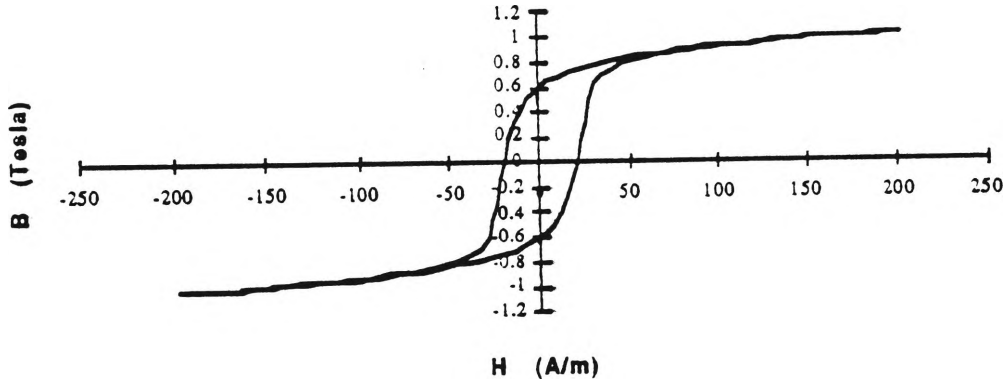

(b) at 400 Hz

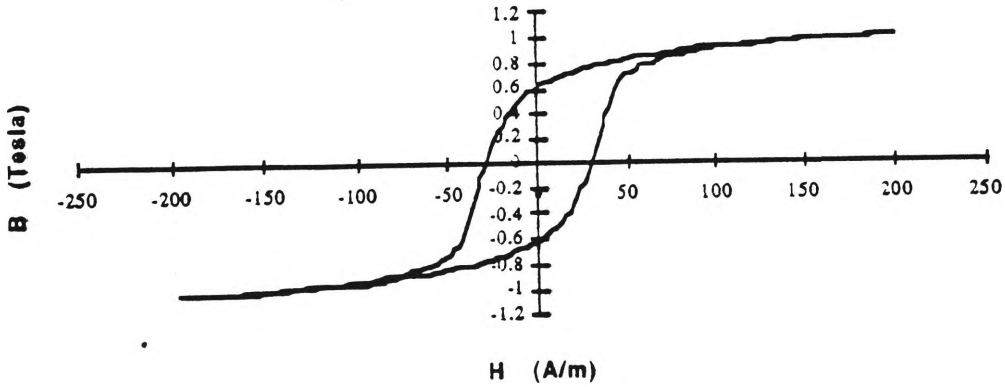

(c) at 1 kHz

Fig.4.4.10 (continue)

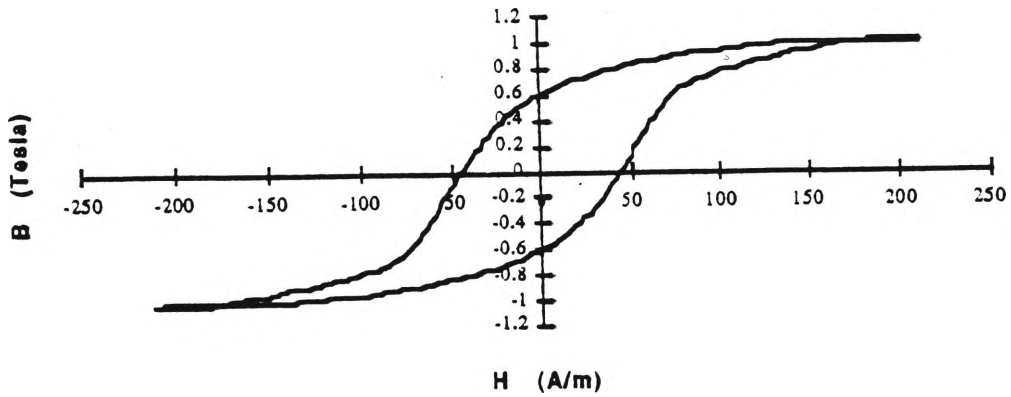

(d) at 5 kHz

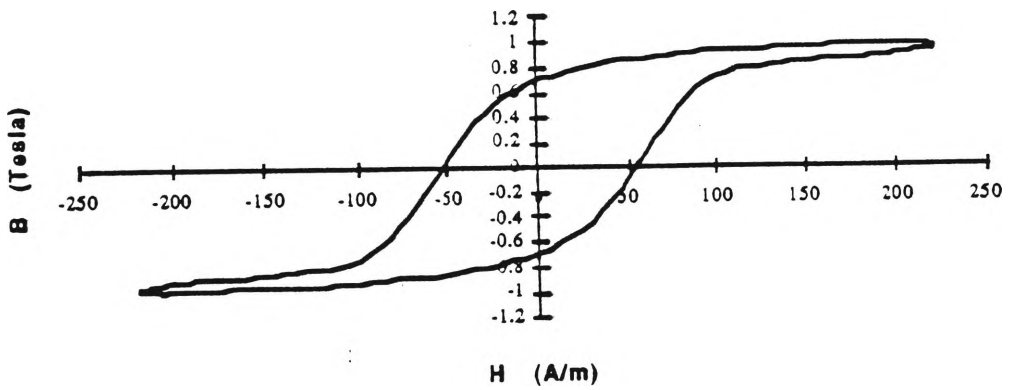

(e) at 10 kHz

Fig.4.4.10 (continue)

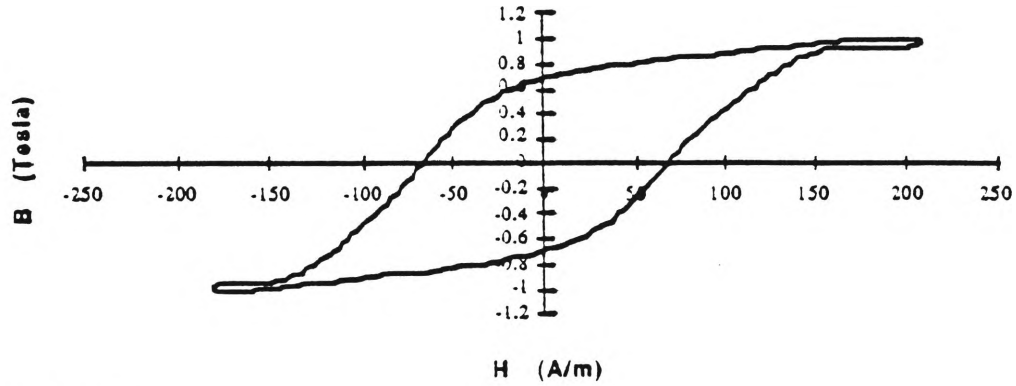

(f) at 25 kHz

Fig.4.4.10 The change in the shape of the hysteresis loop for as-cast $Fe_{72}Si_{10}B_{18}$ ribbon with frequency. The loops were measured with an applied field of 200 A/m ± 10 A/m.

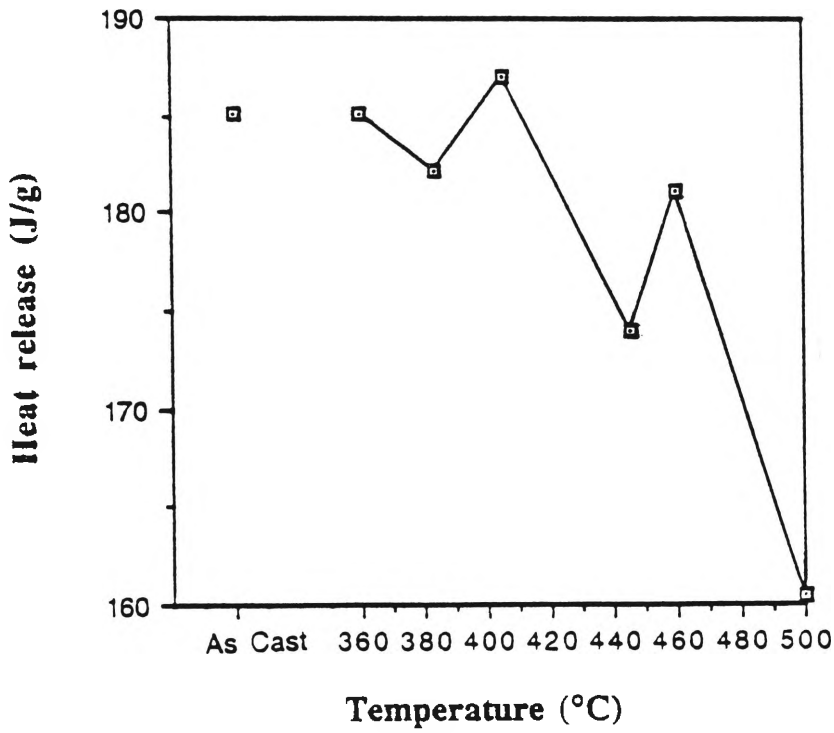

Fig.4.4.11 Size of exothermic peak for $Fe_{72}Si_{10}B_{18}$ ribbon after pre-annealing for 60 mins. at the indicated temperatures.

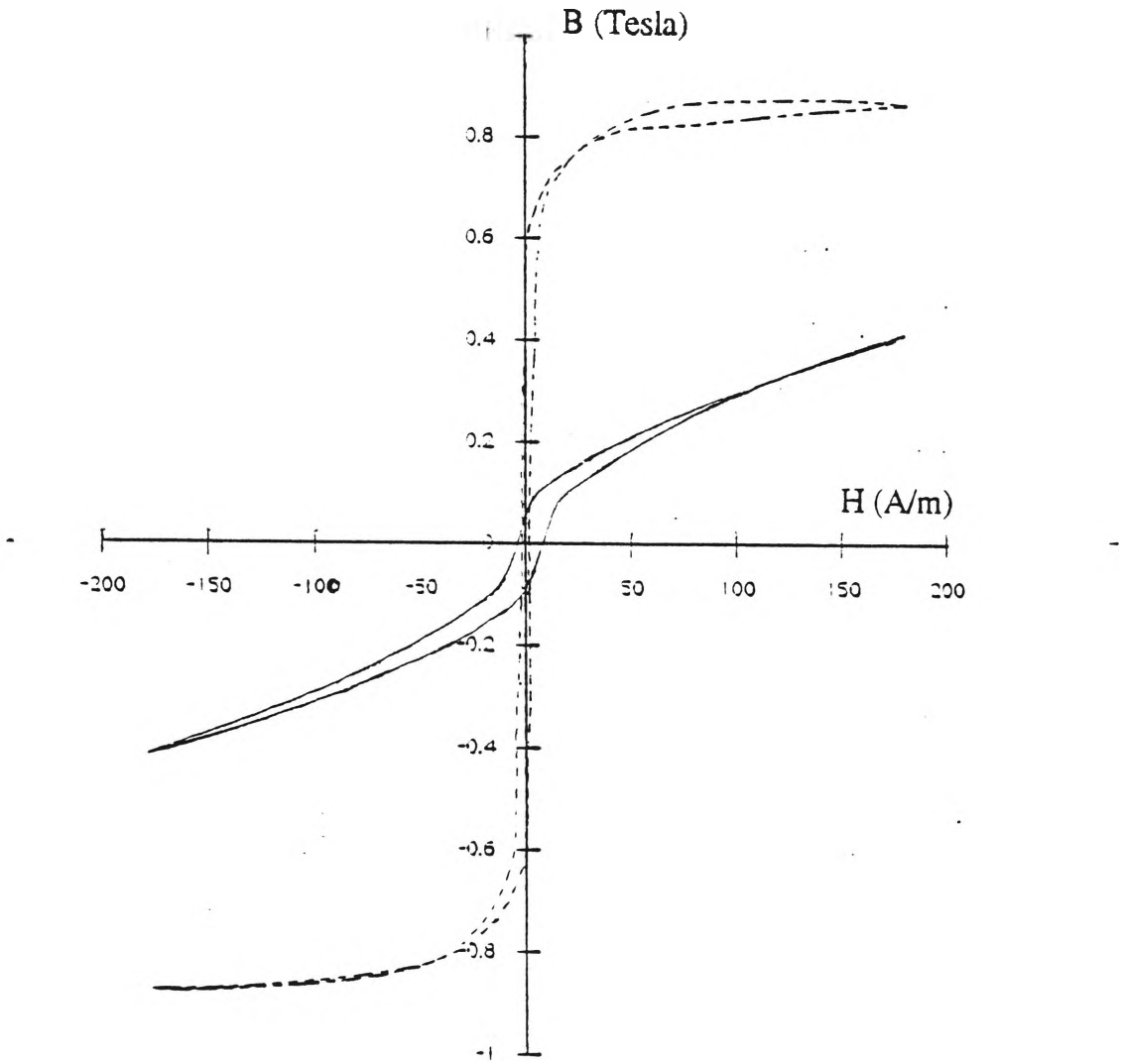

Fig.4.4.12 Hysteresis loop measured at 1 Hz frequency for $Fe_{72}Si_{10}B_{18}$ ribbon annealed for 60 mins. at 480°C (full line). The as-annealed ribbon had H_c = 6.8 A/m and B = 0.4 Tesla. The dotted hysteresis loop was measured after chemically removing 25 % of the total mass of the sample. This loop had Hc = 0.7 A/m and B = 0.87 Tesla. Both the loops were measured at 180 A/m ± 5 A/m.

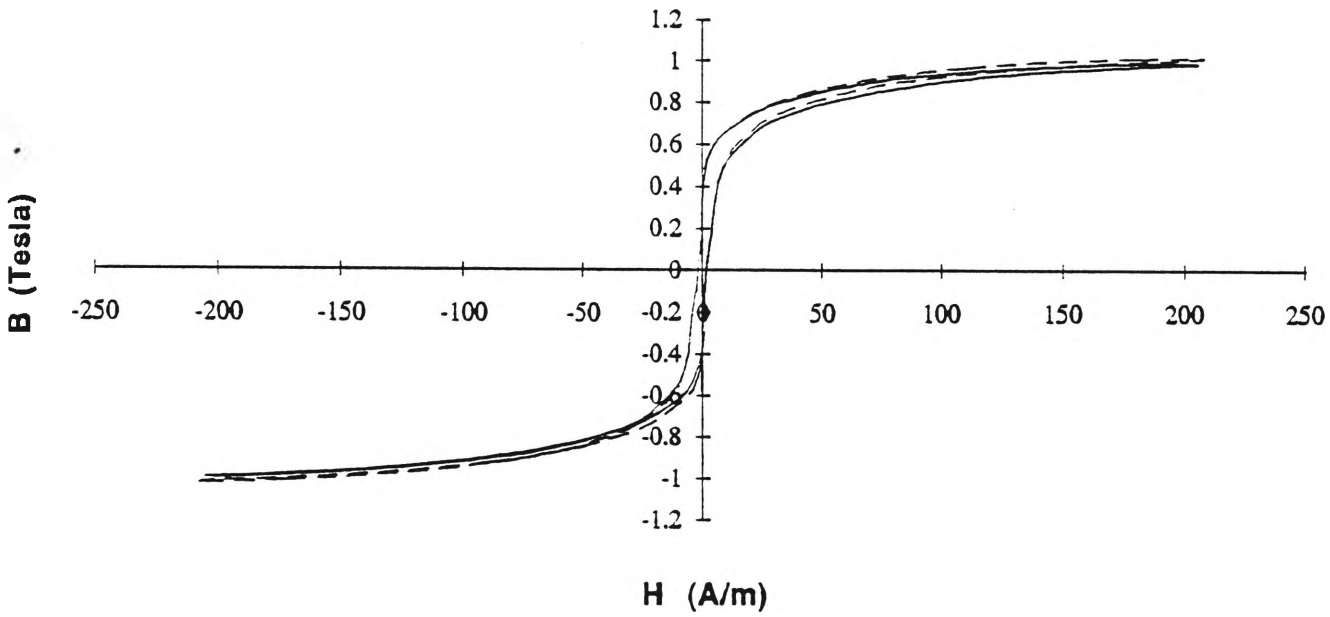

Fig.4.4.13 Hysteresis loop of the as-cast $Fe_{72}Si_{10}B_{18}$ alloy at 1 Hz. The full line loop is from the as-cast ribbon, while the dotted line curve is from the as-cast ribbon after chemically removing 25% mass of the ribbon.

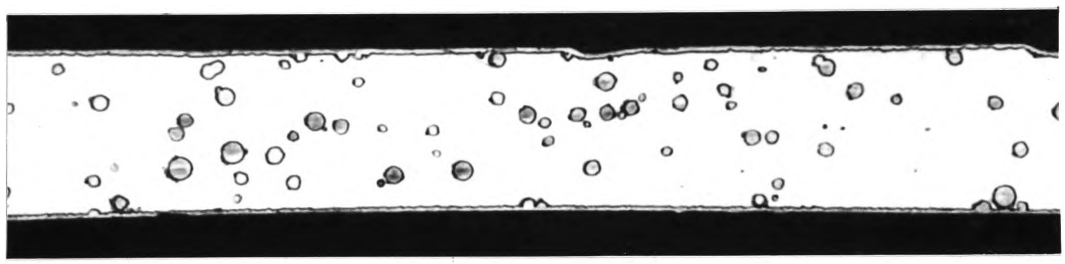

Fig.4.4.14 Optical micrograph of a cross-section for $Fe_{72}Si_{10}B_{18}$ ribbon annealed for 60 mins. at 515°C (X 200).

Chapter 5

5.0 DISCUSSION

The magnetic properties of the materials examined improve significantly upon annealing up to a certain temperature, and then begin to deteriorate when annealed at higher temperatures because of the increase in the percentage of crystals in the structure. The optimum annealing temperature is dependent on the required operating frequency and the composition of the material. The origins of these frequency dependent changes are discussed in sections 5.2, 5.3 and 5.4. Section 5.5 deals with the asymmetrical displacement of the hysteresis loops in the Co-based alloys.

5.1 Presence of temperature gradient in the annealed samples

When annealing of the metallic glasses is carried out, it is necessary to maintain a uniform temperature along the sample. As the percentage of crystallites and their size are major factors at higher operating frequencies in determining the soft magnetic properties of the material, it is necessary to have a uniform annealing temperature across the length of the sample. In these experiments, the annealing was carried out on 10 cm long ribbons, and it was believed that the ribbons had a uniform temperature. Subsequently, in a further study, Fairbank [45] showed the existence of a temperature gradient in the furnace. TEM micrographs showed a higher percentage of crystallites in the bottom part of the ribbon as compared to the top part of the ribbon. This was confirmed by measuring the temperature at different heights in the furnace. The temperature differential between the top and bottom of the sample was found to be 15°C.

The magnetic properties of a material are influenced by the domain wall motion. Due to the temperature gradient along the sample, it is clear that the effects of annealing would be non-uniform along the length of the ribbon. The results obtained in this

work therefore represent an average of the values of properties over a 15°C annealing temperature range, even though the search coil is located over a 1 cm central length of the ribbon. The value of the results is clearly diminished by this error in the experimental technique, but they nevertheless represent an internally consistent set of data. The changes in magnetic properties with annealing temperature will still follow the same trends.

5.2 Response of $Co_{75}Si_{10}B_{15}$ alloy to annealing in an applied magnetic field

Figs.4.2.8a-h show the typical hysteresis loop shapes produced at 400 Hz frequency at an applied field of 200 A/m ± 10 A/m as a function of annealing temperature. The shape of the hysteresis loop changes with the annealing temperature: at lower frequencies the coercivity of the hysteresis loop is a minimum at a certain annealing temperature. That is the optimum temperature for minimum core losses. At higher frequencies the core loss and the coercivity are minimised at different temperatures.

The change in the shape of the hysteresis loop is an indication of how readily the material can be magnetised along a specific direction. At a microscopic level, this is a measure of the ease with which the magnetic domain walls move in the material to accommodate the rate of change of the magnetic field.

At small applied magnetic fields, magnetisation occurs by reversible domain wall motion. At higher applied fields, magnetisation is dominated by large irreversible shifts of domain walls, known as Barkhausen jumps. At very high magnetic fields, the magnetisation of the material increases by a smooth rotation of individual domain magnetisation vectors in the direction of the applied magnetic field. When this process reaches its limit, the material is considered to be at the saturation level.

For material operating near the saturation level, the optimum annealing temperature is dependent on the operating frequency as shown in Fig.4.2.4. Material operating at lower frequencies showed optimum magnetic properties following a 384°C X 60 mins. annealing temperature. As the operating frequency increases, the minimum core loss is obtained at higher annealing temperature. At 50 kHz operating frequency the optimum magnetic properties are obtained following a 446°C X 60 mins. annealing cycle, which is 60°C above the optimum annealing temperature for the 50 Hz operating frequency. The increase in the optimum annealing temperature with operating frequency is in agreement with the literature as explained below.

At mains frequency (50 Hz), the magnetisation of the material occurs by smooth motion of domain walls. Any pinning of the domain walls increases the coercivity and as a result increases the core loss. The as-cast materials have relatively poor properties because they have stress anisotropy which introduces resistance to domain wall motion and increases the core loss. When the material is annealed at a temperature insufficient to introduce crystallisation, the stresses are relieved due to structural relaxation, reducing the stress anisotropy and hence the resistance to domain wall motion is minimised.

Although structural relaxation reduces the effect of domain wall pinning, there are other sources of domain wall resistance such as ragged edges, surface roughness and oxidation of surface layer of the material. It is claimed that if the surface of the material is polished [18], or if the ribbon is manufactured in vacuum [19], this will result in lower coercivity and an improvement in the magnetic properties of the material. If the alloy is annealed in a non-oxidising atmosphere it may also lower the core loss. An oxide layer is believed to generate nucleation sites for crystallisation which increase the number of crystals in the material. At lower frequencies, the

crystals will resist the motion of the domain walls and hence the coercivity is increased and in turn, this results in higher core losses.

The optimum annealing temperature for low frequency applications is not necessarily suitable for higher frequency applications. Since the number of pinning centres is reduced by stress relief, the resistance to domain wall motion is reduced. At higher frequencies the rate of domain wall motion is very high in order to accommodate the rate of change of magnetisation. This high rate domain wall movement will result in high excess eddy current losses. The introduction of crystals reduces the domain wall spacing as well as the domain wall motion by pinning the domain walls. As a result of the reduction of domain wall motion, the distance each domain moves during each half-cycle of excitation decreases. This results in lower excess eddy currents produced by domain wall motion. This excess eddy current is the major contribution to the core loss at higher frequency and therefore, such refinement of domain size minimises eddy current loss contributions to the total core loss. Fig.2.5.9 shows the decrease in core loss with the introduction of small amount of α-Co phase [27,47]. In this work, Fig.4.2.14b shows the diffraction pattern of an α-Co crystal: these crystals result in decreases in core loss at higher operating frequencies. Fig.4.2.3g shows that core loss for 50 kHz operating frequency is at a minimum for a 446°C X 60 mins. annealing cycle and Fig.4.2.13a shows the crystal particles in that sample. While for 458°C X 60 mins. annealing cycle the core loss is high even though Fig.4.2.13b shows crystals in that sample. This can be explained as: when the size of the crystals is of the same order as the wall width, they tend to act as wall nucleation centres, and additional walls are available for participation in the magnetisation process. When the number of these crystals becomes high, or their size is comparatively larger than the domain wall width, then their efficiency of wall pinning is increased. This results in higher coercivity and higher hysteresis losses. Comparing Fig.4.2.4 for core loss vs. temperature and Fig.4.2.5 for coercivity vs. temperature, it is found that the minimum core loss for 50 kHz operating frequency is for a 446°C X 60 mins. annealing cycle but

the minimum coercivity occurs at the 408°C X 60 mins. annealing cycle. This suggests that the minimum core loss obtained at high frequency has higher hysteresis loss components because of higher coercivity and the lower excess eddy current loss components because of wall pinning.

Annealing and cooling the sample in the presence of a magnetic field below the Curie temperature, aligns the magnetic domain magnetisation vectors in the direction of the applied magnetic field. This has the effect of removing domain walls which are not parallel to the applied magnetic field and therefore imparts an easy direction of magnetisation. This results in a squarer loop. In this alloy, all the samples were annealed in a magnetic field but above the Curie temperature (Tc ≈ 360°C) and cooled rapidly in its absence and therefore there is no contribution to the alignment from the magnetic field. This results in rounded loops, as shown in Fig.4.2.8 and Fig.4.2.9.

The maximum permeability of a material is a measure of the extent to which the material can be magnetised. The cobalt-based alloys have a high maximum permeability. The maximum permeability at 50 Hz operating frequency is ~90,000 for this material and is obtained by a 384°C X 60 mins. annealing cycle. At this temperature, the coercivity and the core loss are at a minimum for lower operating frequencies. As the annealing temperature increases the material's soft magnetic properties deteriorate. As a result the material's response to the applied magnetic field decreases and this in turn, reduces the permeability of the material at higher annealing temperature. At higher operating frequencies, in order to reach the saturation induction, higher applied fields are required. As a result, the permeability of the material at higher operating frequencies drops as shown in Fig.4.2.6.

A few anomalies were found in the results for this alloy. For a 423°C X 60 mins. annealing cycle the measured permeability is lower than that of samples annealed at slightly higher and lower temperatures. At the same temperature, an anomaly was

found in coercivity and core loss. This is not in agreement with the available literature and may be due to experimental error.

The crystals formed in cobalt-based alloys to improve the magnetic properties at high frequencies introduce a shift in the hysteresis loop. This is discussed further in section 5.5.

5.3 Response of $Fe_{60}Ni_{20}Si_{10}B_{10}$ alloy to annealing in an applied magnetic field

The $Fe_{60}Ni_{20}Si_{10}B_{10}$ alloy has a Curie temperature of approximately 410°C. These alloys were annealed in a 795 A/m magnetic field both below and above the Curie temperature for a 60 mins. annealing cycle. It was found from magnetic measurements that the onset of crystallisation for 60 mins. annealing occurs below 420°C. The optimum properties following magnetic annealing were found for 322°C X 60 mins. annealing cycle and 343°C X 60 mins. annealing cycle for most of the frequencies.

The effect of annealing in a magnetic field below the Curie temperature is obvious from the hysteresis loops of Fig.4.3.9a-h. These hysteresis loops are squarer (i.e., their squareness ratio (B_r/B_s) is more than the squareness ratio of $Co_{75}Si_{10}B_{15}$ ribbon) than those of Co-based amorphous alloys which were annealed above their Curie temperature.

Magnetic field annealing at a temperature below the Curie temperature induces magnetic anisotropy due to the directional ordering of the magnetic domain magnetisation vectors. Therefore, when a magnetically-annealed sample is subjected to an operating field, all the domains easily align parallel to the applied field, which results in squarer loop.

The change in dimensions of magnetostrictive materials is due to the rotation of 90° domains during magnetisation. If the magnetostrictive material is annealed in a longitudinal magnetic field then the magnetisation of material largely occurs by 180° domain wall motion. This will not introduce a change in the length of the sample. In this work all samples were rapidly cooled in the absence of a magnetic field. This might have caused some alignment of magnetic vectors in the direction different from the direction of applied field. So, when the material is magnetised there are rotations of magnetic vectors which introduces magnetostriction in the sample. This in turn, generates elastic stress which produces pinning centres and hinders domain wall motion, resulting in higher coercivity and higher core loss.

The change in shape of the hysteresis loops with annealing temperature at 400 Hz operating frequency is shown in Fig.4.3.9a-h. As the annealing temperature increases, the coercivity decreases due to stress relief and directional domain ordering caused by magnetic annealing. At the onset of crystallisation, the coercivity increases slowly. When the material contains a higher percentage of crystals, the coercivity increases significantly and the loop becomes skewed as shown in Fig.4.3.9h for the annealing cycle of 420°C X 60 mins.

The increase in core loss with increase in operating frequency is shown in Figs.4.3.4a-g. This phenomenon was explained in the previous section.

The minimum core loss was obtained at 50 Hz using a 343°C X 60 mins. annealing cycle. The coercivity for the same operating frequency is a minimum at the same temperature. The optimum core loss for 400 Hz and 1 kHz operating frequencies was also obtained for 343°C X 60 mins. annealing cycle while the minimum core loss for 5 kHz, 10 kHz, 25 kHz operating frequencies was obtained for a 322°C X 60 mins. annealing cycle. The minimum core loss for the 50 kHz operating frequencies is

obtained for 343 °C X 60 mins. annealing cycle. This irregularity in the observation may be due to experimental error as the measurements were taken only once. The optimum annealing temperature for both minimum core loss and minimum coercivity is approximately same except at 50 kHz. This is apparent from Fig.4.3.5 and Fig.4.3.6.

The maximum permeability in the as-cast material depends on the internal stress of the material produced by rapid quenching. On relieving the internal stresses by annealing, the maximum permeability of the material increases because of the easy motion of the domain walls. Permeability is an indication of the ease with which a magnetic material will magnetise. The ease of magnetisation of the material falls with the onset of crystallisation in the sample and so the maximum permeability drops for the materials annealed at higher temperatures.

5.4 Response of $Fe_{72}Si_{10}B_{18}$ alloy to annealing in an applied magnetic field

The Curie temperature of $Fe_{72}Si_{10}B_{18}$ is approximately 450°C. The amorphous ribbons of this alloy were annealed below and above the Curie temperature in a 795 A/m magnetic field. The effect of annealing as a function of temperature can be seen from the shape of the hysteresis loops shown in Fig.4.4.9a-i. Annealing below the Curie temperature in a magnetic field improves the shape of the hysteresis loop as explained above for the $Fe_{60}Ni_{20}Si_{10}B_{10}$ alloy.

In this alloy several anomalies were found. The hysteresis loops of this alloy start to become skewed after the 445°C X 60 mins. annealing cycle. This temperature is just below the Curie temperature and is believed to be due to the onset of crystallisation in the bulk or surface of the amorphous ribbon, although no optical metallographic evidence of crystallisation was found after annealing at this temperature. As the annealing temperature is increased further the hysteresis loop becomes more and

more skewed and for the 500°C X 60 mins. annealing cycle the hysteresis loop is flat. There was no metallographic evidence for crystallisation following a 500°C X 60 mins. annealing cycle, although the flat loop indicates that crystals are present in this alloy. The size of the exothermic peak in the DSC thermogram of each annealed sample was measured. The heat evolved in the DSC peak vs. annealing temperature plot is shown in Fig.4.4.11. This plot indicates that as annealing temperature increases, the size of the exothermic peak decreases, presumably because of the presence of crystals in the structure. As the number of crystals present in the annealed specimen increases, the size of the exothermic peak decreases. For the 500°C X 60 mins. annealing cycle the heat released was 20 J/g less than that of as-cast material. The first decrease in heat release was found for 445°C X 60 mins. annealing cycle. After that the heat released for 460°C X 60 mins. annealing cycle is increased which is anomalous because the hysteresis loop for 460°C X 60 mins. annealing cycle is more skewed than that of 445°C X 60 mins. annealing cycle, which suggests the presence of a larger number of crystals. This contradiction may be due to the difference in temperature along the length of the ribbon during annealing. The region from which the ribbon was selected for DSC measurements may have had a lesser number of crystals. For 500°C X 60 mins. annealing cycle the size of the exothermic heat decreases, again indicating the presence of crystals.

This Fe-based amorphous alloy has a high magnetostrictive constant ($\lambda_S = 30 \text{ X } 10^{-6}$). Material annealed above the Curie temperature is not affected by the magnetic field annealing, and so magnetic vectors are not aligned in the direction of the magnetic field. When these alloys are operated at higher frequencies, magnetisation takes place by the domain wall motion as well as by rotation of the magnetic vector. Since the rotation of magnetic vectors changes the length of the material, higher magnetostriction will occur in this material. This will lead to elastic stress in the sample and result in more pinning sites for the domain walls. In turn, this will increase the core loss and coercivity of the sample. In this alloy crystallisation appears to start around 445°C X

60 mins. annealing cycle. These crystals will also serve as pinning sites for the domain wall motion at lower operating frequency. These crystals refine the domains and restrict domain wall motion which reduces the excess eddy current at higher operating frequency. This kind of refinement will however contribute to the higher magnetostriction because in this case magnetisation at higher frequency will occur by rotation of magnetic vectors in the domains. The higher magnetostrictive samples are not suitable for magnetic measurements on our instrument because in this instrument the ribbon is slipped into a small slot around which the secondary coil is wound. Hence at high applied magnetic fields, if the operating frequency is high, significant magnetostriction will occur in the sample. As a result the ribbon will constantly vibrate and change its position, leading to fluctuations in the voltage induced in the secondary coil. These fluctuations will lead to errors in measurement of core loss, coercivity and permeability at higher operating frequency, as can be seen in Fig.4.4.4, Fig.4.4.5, Fig.4.4.6, Fig.4.4.7 and Fig.4.4.8.

5.5 Asymmetrically displaced hysteresis loop

In order to improve the soft magnetic properties of the Co-based amorphous alloys at higher operating frequency, a small percentage of crystals are introduced into the structure by annealing, and this annealing produces asymmetrically displaced hysteresis loops. This phenomenon has been observed in two forms, either as a shift in the hysteresis loop at lower applied fields or as a dip in the second quadrant of the hysteresis loop at higher applied fields as discussed below. Schematic diagrams of both the types of asymmetrically displaced hysteresis loop are shown in Fig.5.5.1.

Becker [40] has suggested that one possible cause of the asymmetrically displaced hysteresis loops is surface crystallisation of the ribbon. He carried out experiments on a $Co_{66}B_{30}Si_4$ amorphous alloy and showed metallographic evidence of surface crystallisation in this alloy. The magnetic measurements done on this alloy

(a)

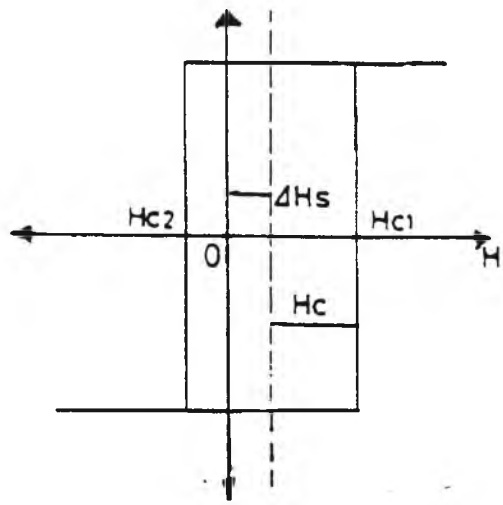

$H_c = (H_{c1} - H_{c2})/2$ $\Delta H_s = (H_{c1} + H_{c2})/2$

(b)

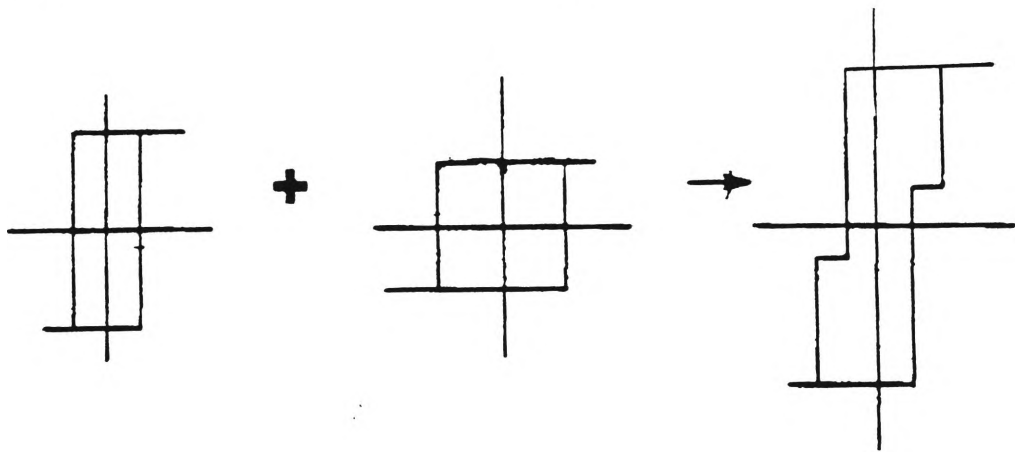

Fig.5.5.1 Schematic diagrams of asymmetrically displaced hysteresis loop

(a) shift in hysteresis loop at lower applied field [39]

(b) dip in second quadrant in hysteresis loop at higher applied field [40].

showed a dip in the second quadrant. To support his arguments for the dip in the second quadrant he carried out experiments on $Fe_{70.5}B_{15.5}Tb_7La_7$ ribbon which shows preferred surface crystallisation. This amorphous alloy when operated at a higher applied field also showed a dip in the second quadrant of the hysteresis loop, but this dip was removed from the hysteresis loop after chemically removing the surface.

Yamauchi and Yoshizawa [39] carried out experiments on $(Co,Fe,Mn,Nb)_{76}Si_{15}B_9$ amorphous ribbon and showed that the shift is prominent at higher annealing temperatures when there are more crystals in the sample. In magnetically-annealed samples the shift is more prominent than when annealed in the absence of magnetic field. In their experiments, chemical removal of the surface did not decrease the shift as shown in Fig.5.5.2

The experiments carried out in this work showed a hysteresis loop shift in $Co_{75}Si_{10}B_{15}$ ribbon when annealed at higher temperatures. A shift in hysteresis loops for $Fe_{72}Si_{10}B_{18}$ which was known to have surface crystallisation was not observed. The $Fe_{60}Ni_{20}Si_{10}B_{10}$ ribbon which shows bulk crystallisation also did not show a shift in the hysteresis loop.

Ideally, the asymmetrically displaced hysteresis loop measurements should be carried out in a static magnetic field in order to avoid all dynamic effects which may arise when measurements are taken in an AC magnetic field. In this work, all the measurements of asymmetrical displacements of the hysteresis loops were done at 1 Hz operating frequency.

$Co_{75}Si_{10}B_{15}$ amorphous ribbon in the as-cast state did not show a shift in the hysteresis loop. In our instrument, a shift of $\pm$ 1 A/m is within experimental error. When this ribbon was annealed at higher temperatures, crystals were produced, and these crystals resulted in a shift in the hysteresis loop as shown in Fig.4.2.10. On

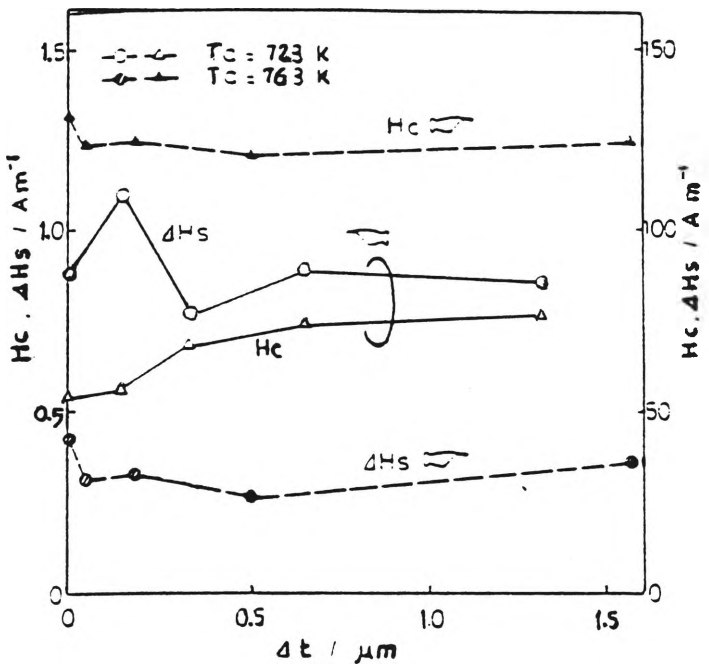

Fig.5.5.2 Change in H_c and ΔH_s for $(Co,Fe,Mn,Nb)_{76}Si_{15}B_9$ alloy as a function of amount of material removed Δt [39].

increasing the annealing temperature, the number of crystals increased and the size of the shift in the hysteresis loop increased as shown in Fig.4.2.12.

The cause of the asymmetrical displacement in the hysteresis loop was suggested by Becker to be due to surface crystallisation as shown in Fig.5.5.3 [40]. In the present work, there was no optical metallographic evidence for a surface crystalline layer in this alloy annealed at 472°C (see Fig.4.2.11). In order to check whether the shift was due to the surface effects or due to the crystals in the bulk, the surface layer of the $Co_{75}Si_{10}B_{15}$ sample was removed chemically by dil. HNO_3. The hysteresis loop measured after chemically removing the surface still showed a displacement in the hysteresis loop, although the extent of the shift was decreased. Yamauchi and Yoshizawa [39] also found that the extent of the shift did not vary significantly with the removal of the surface as shown in Fig.5.5.2. From this figure it is clear that the extent of the shift is not affected by increasing the percentage of removed material. This supports the idea that bulk rather than surface crystallisation may be primarily causing the shift. Yamauchi and Yoshizawa suggested that an oxide layer may cause the displacement. This may contribute to the total extent of the shift in these experiments since the shift decreased in size after chemically removing the surface.

To verify Becker's claim that surface crystallisation can produce a shift in the hysteresis loop, an $Fe_{72}Si_{10}B_{18}$ amorphous alloy was selected for magnetic measurements. This amorphous ribbon is known to show surface crystallisation [47,48].

The change in shape of the hysteresis loops of the $Fe_{72}Si_{10}B_{18}$ alloy on annealing are shown in Fig.4.4.12. These hysteresis loops did not show a shift as would be expected if surface crystallisation always produces a shift. Another major change in the hysteresis loops was the beginning of skewed hysteresis loop after 445°C X 60 mins. annealing cycle. As the annealing temperature increased, the loop became

(a)

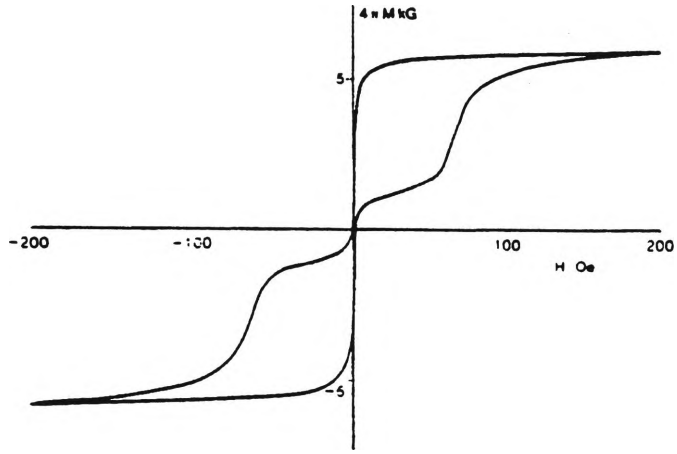

(b)

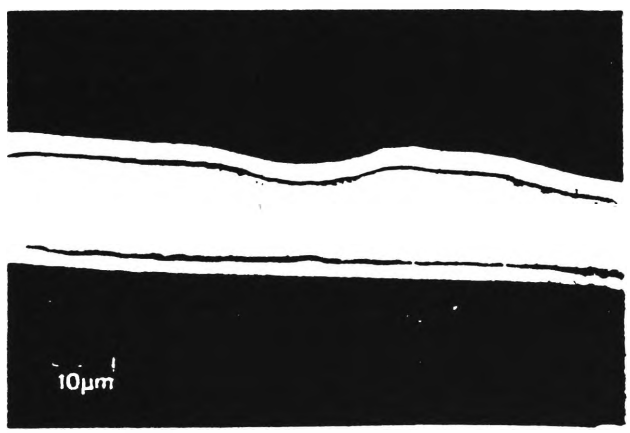

Fig.5.5.3 (a) Hysteresis loop of $Co_{66}B_{30}Si_4$ alloy annealed for 15 mins. at 550°C

(b) Cross-section of $Co_{66}B_{30}Si_4$ alloy annealed for 15 mins. at 550°C [40].

more skewed, an indication of crystallisation in the sample, either in the bulk or on the surface, because when the soft magnetic properties of the material deteriorate by introduction of the crystals, their magnetic flux drops. However, metallographic evidence of crystallisation was not found for any of the samples for which magnetic measurement were done. Previous work by Wunderlich [48] also showed that there was no optical metallographic evidence of surface crystallisation for 1 hr annealing at 500°C, as confirmed by this work. In order to check whether other surface effects were important, the surface of a 480°C annealed $Fe_{72}Si_{10}B_{18}$ sample was removed by chemical polishing in dil. HNO_3. Fig.4.4.12 shows the shape of the hysteresis loop for the as-annealed sample and after chemically removing the surface of the same ribbon. The hysteresis loop shows a significant change in shape after chemically removing the surface of the sample. The hysteresis loop shows that higher induction can be reached by applying a lower magnetic field and the hysteresis loop also shows a significant change in the coercivity. This change suggests that some surface effect produced by annealing is very significant. In order to check whether this effect resulted from annealing, an as-cast sample was also chemically polished and measurements were taken at 1 Hz operating frequency. Both the as-cast and the chemically polished sample, showed the same hysteresis loop as shown in Fig.4.4.13. Therefore it is the annealing treatment that generates the surface effects, even though this annealing produces no observable microstructural changes at the optical metallographic level.

To check whether the bulk crystallisation could be a reason for the shift in the hysteresis loop in Fe-based alloys, a $Fe_{60}Ni_{20}Si_{10}B_{10}$ amorphous alloy was selected. Ribbon samples were heat treated in presence of magnetic field below their Curie temperature. The hysteresis loops measured at 1 Hz for this alloy are shown in Fig.4.3.11. There was no shift in the hysteresis loops.

The shift phenomenon was observed only in the cobalt-based amorphous alloys. The optical metallographic and TEM evidences suggest that the shift in the hysteresis loop occurs mainly because of the formation of the crystals in the bulk of the ribbon. The shift phenomenon can be explained qualitatively as follows [41]. When the cobalt-based amorphous alloy is annealed, two magnetic phases appear in the sample. One phase is the amorphous matrix, which has soft magnetic properties such as low core loss, low coercivity and no particular easy magnetisation direction unless it has stress or field-induced magnetic anisotropy in a particular direction. The second phase is the crystalline phase which is introduced by annealing. It has hard magnetic properties such as higher coercivity and higher core loss as well as easy magnetic directions along particular directions in the crystal. When the magnetic field is applied to this two phase sample, all the magnetic vectors from the amorphous region and from the α-Co regions are aligned in the direction of the applied field. When the applied magnetic field is reversed, the magnetic vectors in the crystals will not change direction and will hinder the rotation of the magnetic vectors in the amorphous matrix in the sample. The cobalt has crystalline anisotropy which is 10 times greater than that of iron and 100 times more than nickel. Therefore, in order to alter the direction of magnetic vector of the crystalline region, very high magnetic fields are necessary. The magnetic vectors of the crystalline region would couple with nearby magnetic vectors of the matrix region. As a result, when the direction of the applied magnetic field is reversed, the coupled magnetic vectors of matrix region oppose the change of direction of magnetisation. Instead they are rotated at an angle as shown in Fig.5.5.4. This requires a larger field than $(H_{c1} + H_{c2})/2$, in order to establish a demagnetised state of the whole sample. Now, when the magnetic field is reversed again, the magnetic vectors of amorphous matrix coupled with the magnetic vectors of the crystals would begin to rotate along the field direction while the uncoupled magnetic vectors of the matrix region would change their direction as usual. This will lead to a shift in the hysteresis loop in the cobalt-based amorphous alloys. At higher annealing

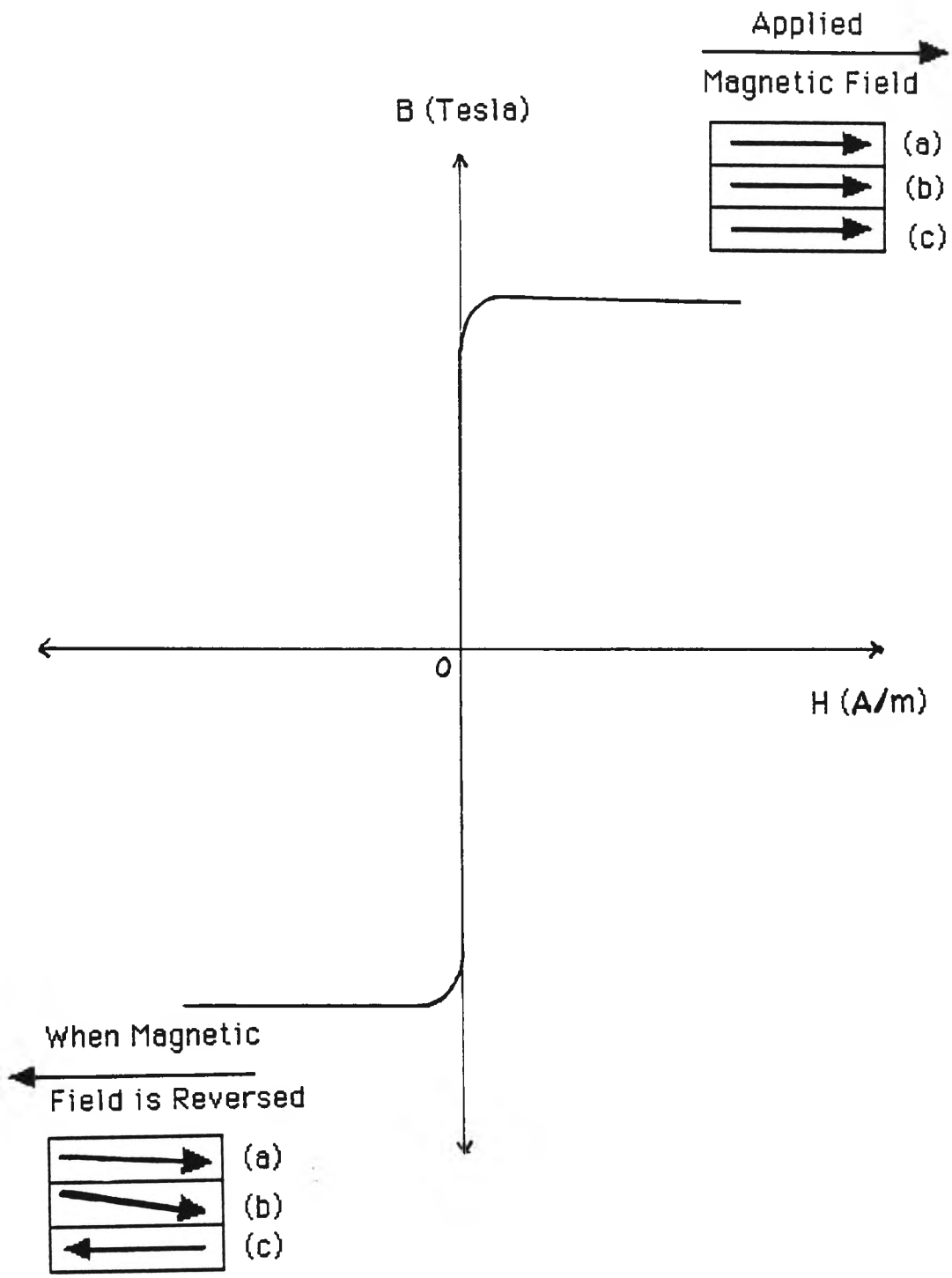

Fig.5.5.4 The magnetisation behaviour in Co-based alloy having two magnetic phases.

(a) alignment of magnetic vector in crystals

(b) magnetic vector of amorphous matrix coupled to crystalline region

(c) alignment of magnetic vector in amorphous region.

temperatures, the number and size of crystals is greater and therefore the shift of the hysteresis loop will be greater.

At higher applied magnetic fields the same phenomenon operates but in a slightly different way. All the coupled magnetic vectors alter their direction at the higher applied field. This will cause the dip in the second quadrant.

5.6 Effect of rough ribbon surface on magnetic property

Ribbons prepared in air have different magnetic properties from the ribbons prepared in vacuum [19]. The ribbon prepared in air has rough surface on the wheel side due to the air entrapment between the ribbon and the wheel surface. Overshott [21] suggested that the rough ribbon surface is one of the reason for non-repetitive non-uniform domain wall motion which leads to the increase of excess eddy current loss. Since it is difficult to observe and quantitatively measure the non-repetitive dynamic domain wall motion, Aboalkaz et al. [18] measured the harmonic content of the flux density under sine H magnetisation condition. They found that if the wheel side surface of the ribbon is made smooth the percentage of harmonic content decreases. This decrease in the percentage of harmonic content is due to the decrease of non-repetitive non-uniform domain wall motion. As a result coreloss may decrease. Since the rough surface pins the domain wall motion, the percentage of the harmonic content increases which leads to the higher excess eddy current loss at the mains frequencies and hence the higher coreloss.

Chapter 6

6.0 CONCLUSIONS

The results of the present work suggest the following conclusions:

1) The soft magnetic properties, such as core loss, coercivity, saturation induction and maximum permeability, of $Co_{75}Si_{10}B_{15}$ metallic glass alloy improve for lower frequency applications on annealing below the crystallisation temperature. For this alloy, there is a 60°C temperature difference between the optimum annealing temperature for minimum core loss temperature at 50 Hz frequency (384°C) and at 50 kHz frequency (464°C). Crystallisation of α-Co after annealing for 60 mins. at 446°C is responsible for the decrease in core loss at 50 kHz frequency. These crystals restrict the domain wall motion and refine the domain size, resulting in decreases in the excess eddy current loss. The introduction of crystals into the structure also produces a displacement in the hysteresis loop. In this alloy at least, the displacement is due principally to uniform crystallisation within the bulk of the ribbon rather than at the surface, as has been suggested for other metallic glasses. Surface oxidation may also contribute to the hysteresis loop shift.

2) The $Fe_{60}Ni_{20}Si_{10}B_{10}$ alloy has 20°C difference in optimum annealing temperatures for different frequencies. On annealing at temperatures below the crystallisation temperature, the magnetic properties improve significantly. This alloy does not show a displacement in the hysteresis loop.

3) The $Fe_{72}Si_{10}B_{18}$ alloy has very high magnetostriction hence its magnetic properties were very difficult to measure with our instrument. This alloy produces a skewed hysteresis loop after relatively low temperature annealing,

(60 mins. at 445°C), but did not show any hysteresis loop displacement as was expected from the literature since this alloy shows preferred surface crystallisation. Surface crystallisation could not be observed optically in any of the annealed samples on which magnetic properties could be measured, although DSC work suggested that annealing above 445°C for 60 mins. introduces crystals into the structure. When the surfaces of the annealed ribbons were removed, a sharp increase in induction and decrease in core loss was observed, indicating that some unidentified surface effect is responsible for the sharp deterioration of magnetic properties and skewed hysteresis loops on annealing.

7.0 REFERENCES

1. P. DUWEZ, R.H. WILLENS and W. KLEMENT, J. Appl. Phys., **31** (1960), 1136.
2. C.M. ADAM and G.E. FISH, Metals Forum, **7**, No.4 (1984), 218.
3. "Key Engineering Materials", Edited by G.S. Ansell, D.J. Fisher, P. Haasen, J. Weertman, F.H. Wohlbier, **17** (Trans Tech Publications, Switzerland, 1987), 225.
4. J.J. GILMAN, Science, **208** (1980), 856.
5. D. NARASIMHAN, U.S.Patent 4 142 571 (1979).
6. H.W. NG, R. HASEGAWA, A.C. LEE and L.A. LOWDERMILK, in "Proceedings of the IEEE", **79**, No.11 (1991), 1608.
7. P. DUWEZ, R. WILLENS and R. CREWDSON, J. Appl. Phys., **36** (1965), 2267.
8. H. WARLIMONT and R. BOLL, J Mag. Mag. Mater., **26** (1982), 97.
9. H.S. CHEN and D.E. POLK, U.S.Patent 3 856 513 (1974).
10. R.BOLL, in "The Vacuumschmelze Handbook, Soft Magnetic Materials", Vacuumschmelze GmbH, Hanau, 1979.
11. R. JOSEPH and E. SCHLOMANN, J. Appl. Phys., **36**, No.5 (1965), 1579.
12. M. MA and C. GRAHAM, IEEE Trans. Mag., **MAG-16** (1980), 1144
13. M. BLUNDELL, K.J. OVERSHOTT, and C.D.GRAHAM Jr., J. Appl. Phys. **50** (1979), 1598.
14. J. KHACHAN and G.W. DELAMORE, Rev. Sci. Instrum., **63,** No.5 (1992), 3222
15. Y. GUOBIN, X. CHUANSAN, W. SHUANGQUAN and W. RUN, in "Proc. of the 4th. Int. Conf. on Rapidly Quenched Metals", Sendai, 1981, Edited by T. Masumoto and K. Suzuki (Japan Inst. Metals,1982), 985.

16 H. KRONMULLER, in "Proc. of the 4th. Int. Conf. on Rapidly Quenched Metals", Sendai, 1981, Edited by T. Masumoto and K. Suzuki (Japan Inst. Metals,1982), 971.

17 J. FINK-FINOWICKI, B. LISOWSKI, in "Summer School on Amorphous metals,Wilga, Poland, 1985", Edited by H. Matyja and P.G. Zelinski, (World Scientific Publishing, Singapore, 1986), 263.

18 I.A.M.A. ABOALKAZ, J. RABIAS and K.J. OVERSHOTT, IEEE Trans. Mag., **MAG-19**, No.5 (1983), 1928.

19 F.E. LUBORSKY, H.H. LIEBERMANN, J.J. BECKER and J.L. WALTER, in "Rapidly Quenched Metals III", Edited by Cantor, **2**, (TMS, London, 1978), 188.

20 H.R.HILZINGER, J. Mag. Mag. Mater. , **83** (1990), 370.

21 K.J.OVERSHOTT, in "Proc. of the 4th. Int. Conf. on Rapidly Quenched Metals", Sendai, 1981, Edited by T. Masumoto and K. Suzuki (Japan Inst. Metals,1982), 835.

22 K.J. OVERSHOTT and M.H. PRICE, IEEE Trans. Mag.,**MAG-18**, No.6 (1982), 1395

23 W. T. McLYMAN, "Transformer and inductor design handbook", Marcel Dekker, New York, 1988.

24. F.E. LUBORSKY, in "Amorphous Metallic Alloys" , Edited by F.E. Luborsky, (Butterworths Monographs in Materials, Butterworth & Co Ltd., London, 1983),.360.

25 G.E. FISH and C.H. SMITH, in "Soft and hard magnetic materials with applications", Proc. symposium held 4–9 October, 1986, Edited by J.A. Salsgiver, K.S.V.L. Narasimhan, P.K. Rastogi, H.R. Shepard and C.M. Maucione, (ASM, Metal Park, Ohio), 7.

26 V.R.V. RAMANAN, in "Rapidly Solidified Materials: Properties and Processing", Proc. 2nd Int. Conf. on Rapidly Solidified Metals, San Diego, (ASM, 1988), 145.

27 C.S. TSAI, W.J. YANG, M.S. LEU and C.S. LIN, J. Appl. Phys., **70**, No.10 (1991), 5846.

28 Literature supplied by the Allied Chemical Co, Parsippany, NY.

29 T.EGAMI, Mater. Res. Bull., **13** (1978), 557.

30 T. MASUMOTO and T. EGAMI, Mater. Sci. Eng., **48** (1981), 147.

31 C.D. GRAHAM Jr. and T. EGAMI, in "Rapidly Quenched Metals III", **2** (TMS, London, 1978), 96.

32 A. SLAWSKAWANIEWSKA, A. WITEK and A. REICH, Mater. Sci. Eng., **A133** (1991), 363.

33 G. KONCZOS and B.SAS, in "Proc Summer School on Amorphous metals, Wilga , Poland, 1985", Edited by Matyja & Zelinski, (World Scientific Publishing,1986), 105.

34 F.E. LUBORSKY,P.G. FRISCHMANN and L.A. JOHNSON, J. Mag. Mag. Mater., **8** (1978), 318.

35 J. GONZALEZ, J.M. BLANCO, I. TELLERIA, J.M. BARANDIARAN, M. VAZQUEZ, A. HERNANDO and A.R. PIERNA, J. Mag. Mag. Mater., **83** (1990) 168.

36 T. SAWA, S. HASHIMOTO and K. INOMATA, IEEE Trans. Mag., **MAG-23**, No.5 (1987), 3509.

37 G.E. FISH and R.HASEGAWA, J. Appl. Phys., **63**, No.8 (15th April, 1988) 2986.

38 T.W. WU and F. SPAEPEN, Phil. Mag. B, **61**, No.4, (1990), 739.

39 K. YAMAUCHI and Y. YOSHIZAWA, Materi. Sci. and Eng., **A133** (1991) 180

40 J.J. BECKER, IEEE Trans. Mag., **MAG-18**, No.6 (1982), 1451.

41 O. KOHMOTO, N. YAMAGUCHI, K. OHYA and H. FUJISHIMA, Japan J. Appl. Phys., **17**, No.1 (1978), 257.

42 W.P. BRENNAN, in "Analytical Calorimetry", **3**,Edited by S. Porter and J.F. Johnson, (Plenum press, NY, 1974), 110.

43 A. DATTA, N.J. DeCRISTOFARO, and L.A. DAVIS, in "Proc. of the 4th. Int. Conf. on Rapidly Quenched Metals", Sendai, 1981, Edited by T. Masumoto and K. Suzuki (Japan Inst. Metals,1982),.1007

44 R. HASEGAWA, G.E. FISH and V.R.V. RAMANAN, in "Proc. of the 4th. Int. Conf. on Rapidly Quenched Metals", Sendai, 1981, Edited by T. Masumoto and K. Suzuki (Japan Inst. Metals,1982), 929

45 A.FAIRBANK, private communication

46 M.S. LEU, C.S. TSAI, C.H. CHANG, and C.S. LIN, in "Proc. of 1989 Conference of the Chinese Society for Materials Science" (1989), 253.

47 M.A. GIBSON, Ph.D. thesis, University of Wollongong,1988.

48 S.J. WUNDERLICH, B.Met. thesis, University of Wollongong, 1986

49 C.W. CHEN, "Magnetism and metallurgy of soft magnetic materials", North Holland, 1977.

50 M.G. BLUNDELL, C.D. GRAHAM Jr. and K.J. OVERSHOTT, J. Mag. Mag. Mater., **19**, (1980), 174.